Dissertation

submitted to the

Combined Faculties of the Natural Sciences and Mathematics

of the Ruperto-Carola-University of Heidelberg, Germany

for the degree of

Doctor of Natural Sciences

Put forward by

Osvaldo Aquines Gutiérrez

born in: Monterrey N.L. Mexico

Oral examination: 20.12.2017

"Inclusive V^0 Production at the LHC"

Referees: **Prof. Dr. Werner Hofmann**
Prof. Dr. Stephanie Hansmann-Menzemer

Abstract

The inclusive production of V^0-particles, i.e. K_s^0 mesons, Λ and $\overline{\Lambda}$ baryons in pp-collisions at a centre-of-mass energy of 7 TeV is analyzed with the LHCb detector. The study is done separately for both polarities of the LHCb spectrometer magnet. The results are combined for the final cross-section measurements. The total luminosity used for the analysis is 1.8 nb^{-1}. The production cross-section is measured in bins of the V^0 phase space. The kinematic variables used are the V^0 transverse momentum p_T and rapidity y. The selected range for the kinematic variables is $0 \leq p_T \leq 2.4\,\mathrm{GeV}/c$ and $2.5 \leq y \leq 4.5$ for the K_s^0 and $0.2 \leq p_T \leq 2.4\,\mathrm{GeV}/c$ and $2.5 \leq y \leq 4.0$ for Λ and $\overline{\Lambda}$. The measurements are compared with predictions from QCD based models of multi-hadron production at high energies.

Zusammenfassung

Die Produktion von V^0-Teilchen, d.h. K_s^0 Mesonen sowie Λ und $\overline{\Lambda}$ Baryonen, in pp-Kollisionen bei einer Schwerpunktsenergie von 7 TeV wurde mit Hilfe des LHCb-Detektors untersucht. Die Studie wurde für beide Polaritäten des LHCb-Spektrometermagnets durchgeführt. Für die endgültigen Wirkungsquerschnitte wurden die Einzelmessungen kombiniert. Insgesamt basiert die Analsye auf einer itegrierten Luminosität von 1.8 nb^{-1}. Die Produktionsquerschnitte wurden in Bins des Phasenraumes bestimmt, und zwar als Funktion des Transversalimpulses p_T und der Rapidität y der V^0s. Der untersuchte kinematische Bereich ist $0 \leq p_T \leq 2.4\,\mathrm{GeV}/c$ und $2.5 \leq y \leq 4.5$ für K_s^0 Mesonen, und $0.2 \leq p_T \leq 2.4\,\mathrm{GeV}/c$ und $2.5 \leq y \leq 4.0$ für Λ and $\overline{\Lambda}$. Die Messungen werden mit Vorhersagen QCD-basierter Modelle zur Beschreibung der Multi-Hadron-Produktion bei hohen Energien verglichen.

Acknowledgements

I would like to thank my colleagues from the MPIK Heidelberg LHCb group for their extensive assistance, especially concerning implementation of DaVinci and setting up the framework for GRID jobs, Raluca Muresan for collaboration and feedback for V^0 and minimum bias related issues, and Cesar Castromonte for helping with LaTeX, root and C++ issues.

Also, to my family and friends who gave me their support during my PhD: it would be a long list and I don't want to leave anyone out, but they know who they are and how thankful I am to them.

Contents

Acknowledgements iv

1 Introduction 1

2 Theoretical Background 3

2.1 The Standard Model . . . 3

2.1.1 Leptons . . . 4

2.1.2 Quarks . . . 5

2.1.3 Mediators . . . 5

2.1.4 Strong Force . . . 6

2.1.5 Weak Force and the CKM Matrix . . . 6

2.1.6 Weakly decaying V^0's . . . 9

2.2 QCD . . . 11

2.2.1 Lagrangian . . . 11

2.2.2 Classical Density . . . 11

2.2.3 Gauge Fixing . . . 12

2.2.4 Asymptotic Freedom . . . 13

2.2.5 Confinement . . . 14

2.2.6 Color Wave-Functions . . . 14

2.2.7 Multi-Hadron Production . . . 15

2.2.8 Parton Shower . . . 16

2.2.9 Hadronization . . . 16

2.2.10 Strange Quark Production . . . 17

3 The LHCb Experiment **19**
3.1 The Large Hadron Collider (LHC) . . . 19
3.1.1 LHC Performance . . . 23
3.2 The LHCb Experiment . . . 24
3.3 Tracking . . . 25
3.3.1 Vertex locator . . . 27
3.3.2 Tracker Turicensis . . . 30
3.3.3 Inner Tracker . . . 32
3.3.4 Outer Tracker . . . 36
3.4 RICH . . . 38
3.4.1 RICH1 . . . 39
3.4.2 RICH2 . . . 40
3.5 Magnet . . . 41
3.6 Calorimeter system . . . 42
3.6.1 SPD/PS . . . 44
3.6.2 ECAL . . . 44
3.6.3 HCAL . . . 46
3.7 Muon system . . . 48
3.8 Trigger . . . 48
3.8.1 L0 trigger . . . 50
3.8.2 HLT trigger . . . 50
3.8.3 VELO Microbias Trigger . . . 52

4 Analysis Preface **53**
4.1 DATA and MC Sample . . . 53
4.2 Detector Performance . . . 54
4.2.1 Primary Vertex and IP Resolutions . . . 54
4.2.2 Tracking Efficiency . . . 54
4.2.3 RICH Particle Identification . . . 58
4.3 General Strategy . . . 60
4.3.1 Yields . . . 61

4.3.2 Efficiencies 64

5 Event Selection **66**

5.1 General requirements 66

5.2 Geometrical candidate selection (ω) 67

5.3 Separation of $V^0$from background using ω 69

5.4 Selection efficiency 71

5.5 Kinematic Analysis with Armenteros Variables 78

5.6 Systematic analysis of the discriminant variable ω 80

5.6.1 V^0impact parameter d 80

5.6.2 v_1 and v_2 83

5.6.3 Track impact parameters d_1 and d_2 88

5.6.4 Resolution effect on ω 90

6 Cross-checks **95**

6.1 Invariant mass 95

6.2 Rapidity 99

6.3 Flight length and $c\tau$ 101

7 Systematics **108**

7.1 Yield extraction 109

7.2 Non-prompt and diffractive contributions 114

7.3 Binning and generator dependence 117

7.4 Magnet Down/Up asymmetries 117

8 Results **124**

8.1 Measured yields 124

8.2 Observed efficiencies 128

8.3 Cross-sections 132

8.4 Conclusion 138

A Tables **140**

A.1 Yields 140

A.2 Efficiencies 144
A.3 Cross-sections for both B-field polarities 147
A.4 Systematics 150
A.5 Cross-sections 155

B RICH selection **157**

C V^0production ratios **163**

References **166**

List of Tables

2.1 Leptons (spin 1/2) 5
2.2 Quarks (spin 1/2). Masses are in the $\overline{MS}$ scheme [1] 5
2.3 Mediators (Bosons) 6
2.4 V^0 decay channels and other relevant quantities 11

3.1 Measured main parameters of the LHCb dipole magnet 42
3.2 Main parameters of the LHCb electromagnetic calorimeter 45

4.1 Summary of data samples used for the analysis (DATA2010) 53
4.2 Signal and sideband regions 64

5.1 Observed $\hat{k}$ values for K^0_s-decays 75
5.2 Observed $\hat{k}$ values for Λ, $\overline{\Lambda}$,-decays 75
5.3 Weighted chi-square test values for comparison of d from MC2010 vs DATA2010, before and after smearing. 83
5.4 Weighted chi-square test value for comparison of v_1, v_2 for MC2010 vs DATA2010, before and after smearing. 85

7.1 V^0 systematic uncertainties 108
7.2 Long-Lived Progenitors of Λ's 115

A.1 Number of observed K^0_s-decays on DATA 2010, Magnet Down, in bins of transverse momentum p_T and rapidity y. 140
A.2 Number of observed K^0_s-decays on DATA 2010, Magnet Down, in bins of transverse momentum p_T and rapidity y. 141

A.3 Number of observed Λ-decays on DATA2010, Magnet Down, in bins of transverse momentum p_T and rapidity y. 141

A.4 Number of observed Λ-decays on DATA2010, Magnet Up, in bins of transverse momentum p_T and rapidity y. 142

A.5 Number of observed $\overline{\Lambda}$-decays on DATA2010, Magnet Down, in bins of transverse momentum p_T and rapidity y. 142

A.6 Number of observed $\overline{\Lambda}$-decays on DATA2010, Magnet Up, in bins of transverse momentum p_T and rapidity y. 143

A.7 Estimated reconstruction and selection efficiencies (in %) for K^0_s-decays on MC 2010, Magnet Down, in bins of transverse momentum p_T and rapidity y. 144

A.8 Estimated reconstruction and selection efficiencies (in %) for K^0_s-decays on MC 2010, Magnet Up, in bins of transverse momentum p_T and rapidity y. 144

A.9 Estimated reconstruction and selection efficiencies (in %) for Λ-decays on MC 2010, Magnet Down, in bins of transverse momentum p_T and rapidity y. 145

A.10 Estimated reconstruction and selection efficiencies (in %) for Λ-decays on MC 2010, Magnet Up, in bins of transverse momentum p_T and rapidity y. 145

A.11 Estimated reconstruction and selection efficiencies (in %) for $\overline{\Lambda}$-decays on MC 2010, Magnet Down, in bins of transverse momentum p_T and rapidity y. 146

A.12 Estimated reconstruction and selection efficiencies (in %) for $\overline{\Lambda}$-decays on MC 2010, Magnet Up, in bins of transverse momentum p_T and rapidity y. 146

A.13 Observed K^0_s production cross-section (in μb) in bins of transverse momentum p_T and rapidity y on DATA2010, Magnet Down. The quoted error is statistical. 147

A.14 Observed K_s^0 production cross-section (in μb) in bins of transverse momentum p_T and rapidity y on DATA2010, Magnet Up. The quoted error is statistical. 147
A.15 Observed Λ production cross-section (in μb) in bins of transverse momentum p_T and rapidity y on DATA2010, Magnet Down. The quoted error is statistical. 148
A.16 Observed Λ production cross-section (in μb) in bins of transverse momentum p_T and rapidity y on DATA2010, Magnet Up. The quoted error is statistical. 148
A.17 Observed $\overline{\Lambda}$production cross-section (in μb) in bins of transverse momentum p_T and rapidity y on DATA2010, Magnet Down. The quoted error is statistical. 149
A.18 Observed $\overline{\Lambda}$production cross-section (in μb) in bins of transverse momentum p_T and rapidity y on DATA2010, Magnet Up. The quoted error is statistical. 149
A.19 Estimated uncertainties (in %) due to background estimation for K_s^0-decays. 150
A.20 Estimated uncertainties (in %) due to background estimation for Λ-decays. 150
A.21 Estimated uncertainties (in %) due to background estimation for $\overline{\Lambda}$-decays. 151
A.22 Estimated uncertainties (in %) due to binning (generator dependence) for K_s^0-decays. 151
A.23 Estimated uncertainties (in %) due to binning (generator dependence) for Λ-decays. 152
A.24 Estimated uncertainties (in %) due to binning (generator dependence) for $\overline{\Lambda}$-decays. 152
A.25 Estimated uncertainties (in %) due to difference in reconstruction efficiencies for opposite magnet polarities for K_s^0-decays. 153
A.26 Estimated uncertainties (in %) due to difference in reconstruction efficiencies for opposite magnet polarities for Λ-decays. 153

A.27 Estimated uncertainties (in %) due to difference in reconstruction efficiencies for opposite magnet polarities for $\overline{\Lambda}$-decays. 154
A.28 Measured K^0_s production cross-section (in μb) in bins of transverse momentum p_T and rapidity y as defined on Eq. 4.3. The first quoted error is statistical and the second is the local systematic error. The total global systematic uncertainty is 12%. 155
A.29 Measured Λ production cross-section (in μb) in bins of transverse momentum p_T and rapidity y as defined on Eq. 4.3. The first quoted error is statistical and the second is the local systematic error. The total global systematic uncertainty is 12%. 155
A.30 Estimated $\overline{\Lambda}$ production cross-section (in μb) in bins of transverse momentum p_T and rapidity y as defined on Eq. 4.3. The first quoted error is statistical and the second is the local systematic error. The total global systematic uncertainty is 12%. 156

B.1 Estimated uncertainties (in %) due to RICH particle identification for Λ-decays. 161
B.2 Estimated uncertainties (in %) due to RICH particle identification for $\overline{\Lambda}$-decays. 161

List of Figures

1.1 Predicted $\overline{\Lambda}/\Lambda$ ratio at 7 TeV center-of-mass energy by various generators. Peter Skands, Les Houches Plots [2]. 2

2.1 Elementary particles in the Standard Model [3]. Left: fundamental spin 1/2 particles (quarks and leptons). Right and Center: spin 1 mediators of interactions. 4

2.2 Of the three forces included in the Standard Model, only the weak force allows for quarks or leptons to change flavor and generation. . . 7

2.3 $K_s^0 \to \pi^+ \pi^-$ decay: we can observe the flavor change from an $\overline{s}$ to an $\overline{u}$ quark. 10

2.4 $\Lambda \to$ p π^- decay 10

2.5 β as a function of α_s using 3 active light flavors [4]. 13

2.6 Perturbative QCD branching process following g $\to q\bar{q}$ [5]. 17

2.7 Schematic picture of the formation of hadrons by the string breaking process [6]. 18

3.1 Aerial view of the LHC with SPS [7]. 20

3.2 The CERN Accelerator Complex [8]. 21

3.3 Cross-section schematic view of an LHC dipole magnet [9]. 22

3.4 Map of the LHC showing the stations for its four major experiments [7]. 23

3.5 Angular distribution of $b\bar{b}$ pairs produced in high energy pp collisions [10]. 24

3.6 z view of the LHCb Detector [11]. 26

3.7 VELO's silicon detector modules [11]. 27

3.8 Top: Cross-section of the VELO sensors in the xz-plane, indicating the angular acceptance of the detector and the relative arrangement of the stations. The distance from the first to the last station is 106.5 cm. Bottom: Sketch of a VELO station in the closed and fully open positions [11]. 28
3.9 Sketch illustrating the Rϕ geometry of the VELO sensors [11]. 30
3.10 Schematic showing the xuvx layout of the TT [12]. 31
3.11 TT detector modules [11]. 33
3.12 Front view of a T station [11]. 34
3.13 IT detector modules layouts. Dimensions are given in cm and refer to the sensitive surface covered by the Inner Tracker [11]. 35
3.14 Schematic view of a two-sensor IT module [11]. 36
3.15 Arrangement of OT straw-tube modules in layers and stations [11]. . 37
3.16 Cross section of an OT module [11]. 38
3.17 Cherenkov angle versus particle momentum for the RICH radiators [11]. 39
3.18 Side view schematic layout of the RICH1 detector [11]. 40
3.19 a) Top view schematic layout of the RICH2 detector, b) Schematic layout of the RICH2 detector [11]. 42
3.20 Schematic layout of the LHCb dipole magnet [11]. 43
3.21 Loops of wavelength-shifting (WLS) fibers [13]. 45
3.22 Outer, middle, and inner type ECAL modules [11]. 46
3.23 Schematic view of an HCAL Module [11]. 47
3.24 Schematic side view of the muon system [11]. 49
3.25 Schematic representation of the trigger system 51
3.26 Flow diagram of the trigger sequence [11]. 52

4.1 Primary Vertex (PV) X and Y resolution plotted as a function of the number of tracks used for its calculation, for (a) early 2010 data and (b) MC [14]. 55
4.2 IP resolution for X and Y coordinates plotted as a function of $1/p_T$ for (a) early 2010 data [15] and (b) MC. 56

4.3 K_s^0 signal for two types of candidates: two long tracks (solid black histogram), and one long track and one VELO track with an associated calorimeter cluster (solid blue histogram). Dashed lines represent the yields after background subtraction for each selection [14]. 57

4.4 Tracking efficiency as a function of transverse momentum p_T for K_s^0 reconstruction [14]. 58

4.5 Cherenkov photon profiles measured in RICH1 and RICH2. Blue circles indicate the kaon and pion hypotheses [16]. 59

4.6 Kaon PID efficiency for kaons (black squares) and pions (red squares) [16]. 59

4.7 Proton PID efficiency for protons (black squares) and pions (red squares) [16]. 60

4.8 Invariant mass distribution for K_s^0 candidates on DATA2010. 62

4.9 Invariant mass distribution for K_s^0 candidates from MC2010. 63

4.10 Invariant mass distribution for Λ and $\overline{\Lambda}$ candidates from DATA2010. 63

4.11 Invariant mass distribution for Λ and $\overline{\Lambda}$ candidates from MC2010. . . 64

5.1 Schematic illustration of the various track types, classified by the tracking subdetectors traversed. 67

5.2 Schematic view of the planes formed by the V^0 daughter particles' tracks. The vector $\hat{n}$ is shown at the beginning of the positive and negative daughters as a green arrow, and its projection into the primary vertex as a yellow arrow, where v_1 and v_2 are measured. 67

5.3 3-D schematic view of a simulated V^0 decay showing d, d_1, and d_2. The red and blue lines are the initial momentum directions of the positive and negative daughters, respectively. In between the green knobs is the candidate's decay vertex. Gray lines illustrate the projection of the candidate and daughters' momentum towards the primary vertex (in between the yellow knobs), from which d, d_1, and d_2 are calculated. 68

5.4 ω distribution for true MC candidates (solid red histogram) and combinatorial background (solid blue histogram) for MC2010. 70

5.5 K_s^0's ω distribution from the background subtracted yields in DATA2010(black filled triangles), MC2010 (red filled circles), and true MC particles (solid blue histogram). The ratio plot shows how the simulated data underestimates data for candidates of $\omega \leq 5.5$ and starts overestimating for $\omega \geq 5.5$, hence the need for the correction factor $\hat{k}$ (Eq 5.6). . 73
5.6 ω vs $\pi\pi$ invariant mass on DATA2010. 74
5.7 ω vs $\pi\pi$ invariant mass for MC2010. 74
5.8 Λ, $\overline{\Lambda}$'s ω distributions from background subtracted yields in DATA2010 (black filled triangles), MC2010 (red filled circles), and true MC particles (solid blue histogram). 76
5.9 ω vs $\pi\pi$ invariant mass on DATA2010 77
5.10 ω vs $\pi\pi$ invariant mass on DATA2010 77
5.11 Visualization of the V^0 decay and its momentum components. 78
5.12 Armenteros-Podolansky plot showing the defined structure for K_s^0's and Λ 's. 79
5.13 Λ-invariant mass distribution after $\omega \geq 5.5$ selection (black histogram) for MC2010, showing K_s^0 contamination from true identified K_s^0-decays(cyan filled histogram), and estimated by $|m_{\pi\pi} - 498\text{MeV/c}^2| \leq 30\text{MeV/c}^2$ (solid red histogram). 80
5.14 ω vs d distribution for true MC V^0's for MC2010. 81
5.15 d distribution for selected candidates from DATA2010 (black filled circles), and MC2010 before and after smearing (solid blue and red histograms). 82
5.16 ω vs v_1 distribution of true MC V^0's for MC2010. 83
5.17 ω vs v_2 distribution of true MC V^0's for MC2010. 84
5.18 v_1 vs flight length distribution of true MC V^0's for MC2010. 84
5.19 v_2 vs flight length distribution of true MC V^0's for MC2010. 85
5.20 v_1 distribution for selected candidates from DATA2010 (black filled circles),and MC2010 before and after smearing (solid blue and red histograms). 86

5.21 v_2 distribution for selected candidates from DATA2010 (black filled circles),and MC2010 before and after smearing (solid blue and red histograms). 87
5.22 d_1 vs flight length distribution of true MC V^0's for MC2010. 88
5.23 d_2 vs flight length distribution of true MC V^0's for MC2010. 89
5.24 ω vs d_1 distribution of true MC V^0's for MC2010. 89
5.25 ω vs d_2 distribution of true MC V^0's for MC2010. 90
5.26 d_1 distribution for selected candidates from DATA2010 (black filled circles), and MC2010 before and after smearing (solid blue and red histograms). 91
5.27 d_2 distribution for selected candidates from DATA2010 (black filled circles), and MC2010 before and after smearing (solid blue and red histograms). 92
5.28 d vs v_1 distribution of true MC V^0's for MC2010. 93
5.29 d vs v_2 distribution of true MC V^0's for MC2010. 93
5.30 ω distribution estimated via background subtracted yields for DATA2010 (black filled circles),and MC2010 before (blue histogram) and after smearing (red histogram). 94

6.1 Invariant mass distribution of K^0_s-decays after selection from DATA2010 (black filled circles) and MC2010 (solid blue histogram), normalized to match signal yields. This normalization was chosen because the background contribution in K^0_s-decays is insignificant compared to Λ and $\overline{\Lambda}$-decays. 96
6.2 Invariant mass distribution of Λ-decays after selection from DATA2010 (black filled circles) and MC2010 (solid blue histogram), normalized to match the background area in both distributions. 97
6.3 Invariant mass distribution of $\overline{\Lambda}$-decays after selection from DATA2010 (black filled circles) and MC2010 (solid blue histogram), normalized to match the background area in both distributions. 98

6.4 Observed y distribution of reconstructed and selected K_s^0-decays for DATA2010 (black filled circles) and MC2010 (red filled circles). MC2010 is normalized to match DATA2010 statistics. 99

6.5 Observed y distribution of reconstructed and selected Λ and $\overline{\Lambda}$-decays for DATA2010 (black filled circles) and MC2010 (red filled circles). MC2010 is normalized to match DATA2010 statistics. 100

6.6 Observed flight length distribution of reconstructed and selected K_s^0-decays on DATA2010 (black filled circles) and MC2010 (red filled circles). MC2010 is normalized to match DATA2010 statistics. 103

6.7 Observed flight length distribution of reconstructed and selected Λ and $\overline{\Lambda}$-decays on DATA2010 (black filled circles) and MC2010 (red filled circles). MC2010 is normalized to match DATA2010 statistics. 104

6.8 Observed efficiency in flight length bin distribution. The double structure due to the detector module setup is present. 105

6.9 Observed $c\tau$ distribution of reconstructed and selected K_s^0-decays on DATA2010 (black filled circles) and MC2010 (red filled circles). MC2010 is normalized to match DATA2010 statistics. 106

6.10 Observed $c\tau$ distribution of reconstructed and selected Λ and $\overline{\Lambda}$-decays on DATA2010 (black filled circles) and MC2010 (red filled circles). MC2010 is normalized to match DATA2010 statistics. 107

7.1 Reconstructed and selected K_s^0-decays in bins of p_T for MC2010, measured via background subtracted yields (red filled circles), and true MC (solid blue histogram). 110

7.2 Reconstructed and selected K_s^0-decays in bins of y for MC2010, measured via background subtracted yields (red filled circles), and true MC (solid blue histogram). 111

7.3 Reconstructed and selected K_s^0-decays in bins of p_T for MC2010, measured via background subtracted yields (red filled circles), and true MC (solid blue histogram). 112

7.4 Reconstructed and selected K_s^0-decays in bins of y for MC2010, measured via background subtracted yields (red filled circles), and true MC (solid blue histogram). 113

7.5 Diffractive interaction diagrams. 114

7.6 Transverse momentum p_T distribution of V^0's after selection (black filled circles) showing single diffractive (red filled circles), double diffractive (blue filled circles), and non-prompt contamination (green filled circles) for MC2010. 116

7.7 p_Y vs p_X distributions for reconstructed K_s^0 candidates after selection from DATA2010. 119

7.8 p_Y vs p_X distributions for reconstructed Λ, $\overline{\Lambda}$-decays after selection from DATA2010, for the Magnet Down case. 120

7.9 p_Y vs p_X distributions for reconstructed Λ, $\overline{\Lambda}$-decays after selection from DATA2010, for the Magnet Up case. 121

7.10 p_Y vs p_X distributions for reconstructed K_s^0-decays after selection from DATA2010, combining Magnet Down and Up results. 122

7.11 p_Y vs p_X distributions for reconstructed Λ, $\overline{\Lambda}$-decays after selection from DATA2010, combining Magnet Down and Up results. 123

8.1 Measured K_s^0 yields in bins of p_T (y integrated). Triangles are measurements done on DATA2010 for Magnet Down and Up polarities (black filled and black hollow triangles). In blue and red the same measurements for MC2010 are shown. The distributions are normalized to the same area as the data. Error bars are statistical uncertainties. 125

8.2 Measured Λ yields in bins of p_T (y integrated). Triangles are measurements done on DATA2010 for Magnet Down and Up polarities (black filled and black hollow triangles). In blue and red the same measurements for MC2010 are shown. The distributions are normalized to the same area as the data. Error bars are statistical uncertainties. 126

8.3 Measured $\overline{\Lambda}$yields in bins of p_T (y integrated). Triangles are measurements done on DATA2010 for Magnet Down and Up polarities (black filled and black hollow triangles). In blue and red the same measurements for MC2010 are shown. The distributions are normalized to the same area as the data. Error bars are statistical uncertainties. 127

8.4 Reconstruction and selection efficiencies ϵ^{sel} for K^0_s-decays measured for MC2010, p_T vs y profile. 129

8.5 Reconstruction and selection efficiencies ϵ^{sel} for Λ-decays measured for MC2010, p_T vs y profile. 130

8.6 Reconstruction and selection efficiencies ϵ^{sel} for $\overline{\Lambda}$-decays measured for MC2010, p_T vs y profile. 131

8.7 Observed K^0_s production cross-section (y integrated) in bins of p_T. Triangles are measurements done on DATA2010 for Magnet Down and Up polarities (black filled and black hollow triangles). The blue and red histograms represent the particles generated from MC2010, scaled to match the DATA2010 area. The green histograms represent the prediction by PYTHIA 8. Error bars are statistical uncertainties. . . 133

8.8 Observed Λ production cross-section (y integrated) in bins of p_T. Triangles are measurements done on DATA2010 for Magnet Down and Up polarities (black filled and black hollow triangles). The blue and red histograms represent the particles generated from MC2010, scaled to match the DATA2010 area. The green histograms represent the prediction by PYTHIA 8. Error bars are statistical uncertainties. . . 134

8.9 Observed $\overline{\Lambda}$ production cross-section (y integrated) bins of p_T. Triangles are measurements done on DATA2010 for Magnet Down and Up polarities (black filled and black hollow triangles). The blue and red histograms represent the particles generated from MC2010, scaled to match the DATA2010 area. The green histograms represent the prediction by PYTHIA 8. Error bars are statistical uncertainties. . . 135

8.10 Measured prompt K_s^0 production cross-section as a function of p_T, measured on the LHCb DATA2010 (black filled circles), LHCb @0.9 TeV [17] (black hollow squares), UA1 [18] (blue filled circles), and UA5 [19] (red filled squares). Measurements were done at different cms energies on different hadron collision types and different pseudo-rapidity or rapidity ranges. 136

8.11 Prompt K_s^0 production prediction for the rapidity range $2.5 \leq \mathrm{y} \leq 4.5$, for 7 TeV and 0.9 TeV pp collisions generated using PYTHIA 8 [20]. 137

8.12 Measured prompt Λ and $\overline{\Lambda}$ production cross-section as a function of p_T, measured on the LHCb DATA2010 (black filled circles) and UA1 [18] (blue filled circles). Measurements were done at different center-of-mass energies on different hadron collision types and different pseudo-rapidity or rapidity ranges. 137

B.1 p candidate (black filled circles) and π candidate (red filled circles) momentum p for Λ-decays, after selection, in the signal region. 158

B.2 DLL(p-π) distribution for p candidate momentum for Λ-decays in the signal region (solid black histogram) and sidebands (solid violet histogram). 159

B.3 DLL(p-π) distribution for p candidates from Λ-decays in the signal region for DATA2010 (black filled circles), sideband subtracted DATA2010 (red filled circles), MC2010 (solid blue histogram), and MC truth associated (cyan filled histogram). 160

B.4 Invariant mass distribution for Λ-decays after selection without RICH cuts (solid black histogram) and after DLL(p-π) > 0 (solid violet histogram). 162

C.1 Measured $\overline{\Lambda}/\Lambda$ production ratios in bins of y for DATA2010 (black filled circles), LHCb 2011 measurement [17] (black hollow circles), and generator predictions by MC2010 (solid red histogram) and PYTHIA 8 (solid green histogram). Error bars represent systematic uncertainties. 164

C.2 Measured $\overline{\Lambda}/K_s^0$ production ratios in bins of y for DATA2010 (black filled circles), LHCb 2011 measurement [17](black hollow circles), and generator predictions by MC2010 (solid red histogram) and PYTHIA 8 (solid green histogram). Error bars represent systematic uncertainties. 165

Chapter 1

Introduction

The results obtained so far in heavy flavor physics have been fully consistent with the SM. On the other hand, hadron production in high energy collisions is not fully understood. Strangeness production in hadron-hadron collisions is a good probe for QCD-based hadron production models, since there are no initial strange quarks; therefore, strange particles must come from strong interactions. In this way, strangeness production allows us to verify or refine QCD-based phenomenological predictions from lower energies.

There are three long-lived neutral particles: K_s^0 mesons, Λ, and $\overline{\Lambda}$ baryons. They each contain one strange quark and are commonly referred as V^0's (Section 2.1.6). Measuring the cross section for V^0 production will not just allow for the verification or refinement of QCD-based phenomenological predictions, but will also act as a stepping stone for CP violation measurements using B meson decays, which is the primary objective of the LHCb experiment. It is also important for quark-gluon plasma studies in high energy heavy ion collisions. Here an enhancement in the strange quark production is expected, and it is relevant to know how much of that strangeness is produced by proton-proton interactions, where no quark-gluon plasma is formed. V^0 ratios such as $\overline{\Lambda}/\Lambda$ provide good tests for baryon number transport. Figure 1.1 shows the expected $\overline{\Lambda}/\Lambda$ ratio from theoretical predictions [2] at 7 TeV center-of-mass energy, as a function of the pseudorapidity η. It is clear from this figure that in the central region the ratio is unity, but in the forward region the ratio

starts falling, indicating that the forward region is more sensitive to baryon number transport. This is an area of opportunity for the LHCb experiment, which is fully instrumented in the pseudorapidity range $2.5 \leq \eta \leq 5$.

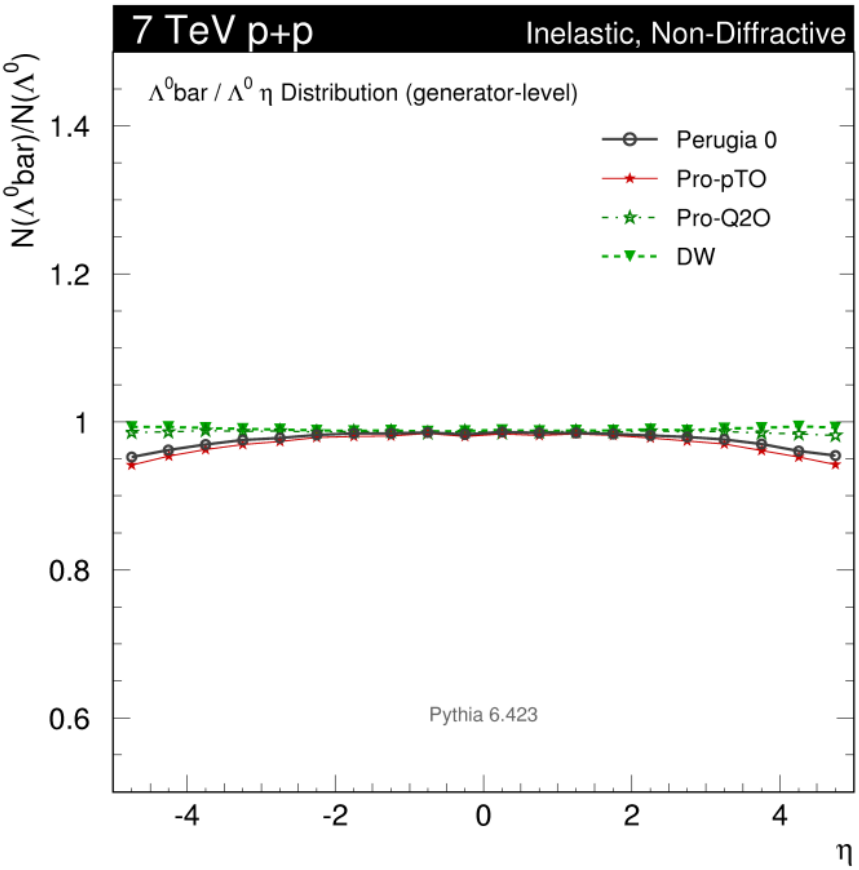

Figure 1.1: Predicted $\overline{\Lambda}/\Lambda$ ratio at 7 TeV center-of-mass energy by various generators. Peter Skands, Les Houches Plots [2].

Chapter 2

Theoretical Background

Since the beginning of mankind, numerous efforts have been made to classify the fundamental constituents of matter. From the early days of Fire, Earth, Air, and Water, through the alchemists of the middle ages to the chemists of the Modern Era, this classification became more complex, and each time, as more was learnt about the intrinsic nature of things, scientists had to deal with smaller and smaller components. For a moment, when electrons and nucleons were discovered, it seemed that a final understanding had been reached. Afterward, however, it was discovered that many other tiny particles of comparable size existed, and furthermore, that nucleons were made up of other smaller particles called quarks. Nowadays, there are many theories that try to explain all of these elements. The Standard Model is one of the most accepted and commonly used.

2.1 The Standard Model

The Standard Model was developed in the 1970s as the basic theory of matter. It is based on sets of fundamental spin 1/2 particles called "quarks" and "leptons", which interact by exchanging intermediate vector bosons, i.e., particles of spin 1 [21]. Nowadays there are seventeen named particles in the Standard Model (Figure 2.1). The last particles discovered were the tau neutrino in 2000, and the Higgs boson in 2012 [22], [23].

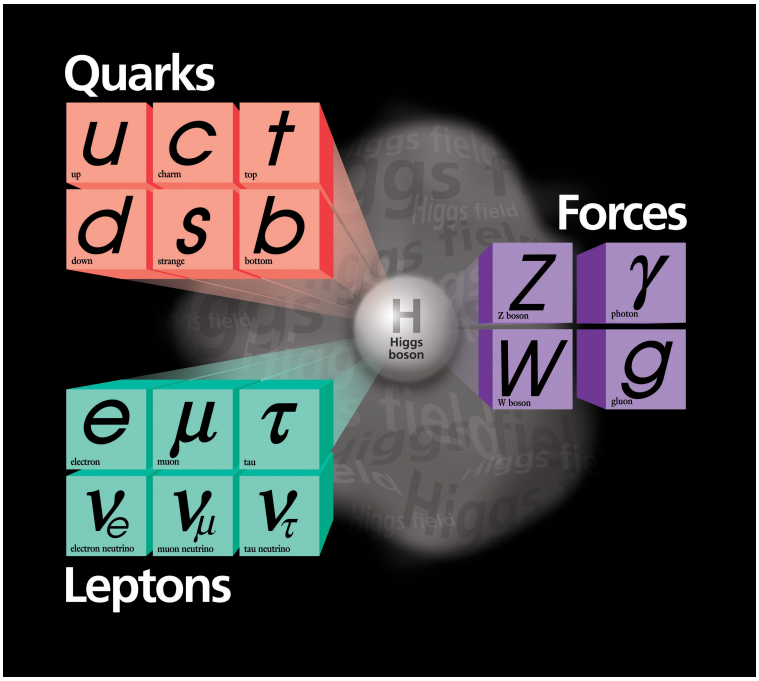

Figure 2.1: Elementary particles in the Standard Model [3]. Left: fundamental spin 1/2 particles (quarks and leptons). Right and Center: spin 1 mediators of interactions.

2.1.1 Leptons

There are six leptons carrying an integral electric charge (in units of the magnitude of the electron charge). They are divided into three generations, each one containing two members: a charged particle and its associated neutral particle, called a neutrino. Each of these six leptons has its own antilepton. For example, the positron has the same mass as an electron but the exact opposite charge. If we count the antiparticles, we have a total of 12 leptons. Table 2.1 shows some of the physical properties of the leptons [24].

Table 2.1: Leptons (spin 1/2)

Lepton	Symbol	Charge($\|e\|$)	Mass(MeV/c^2)
electron	e	-1	0.511 ± 0
electron neutrino	ν_e	0	< 0.002
muon	μ	-1	105.7 ± 0
muon neutrino	ν_μ	0	< 0.19
tau	τ	-1	1776.82 ± 0.16
tau neutrino	ν_τ	0	< 18.2

2.1.2 Quarks

As with leptons, quarks come in 3 generations, each one containing one positive and one negative quark. Negative quarks have a charge of Q=-$\frac{1}{3}$, and positive quarks have a charge of Q=+$\frac{2}{3}$ of the magnitude of the electron charge. Each quark has a different flavor; not counting the anti-particles, we end up with six different flavors (see Table 2.2).

Table 2.2: Quarks (spin 1/2). Masses are in the $\overline{MS}$ scheme [1]

Flavor	Symbol	Charge($\|e\|$)	Mass
up	u	$+\frac{2}{3}$	$2.3^{+0.7}_{-0.5}$ MeV/c^2
down	d	$-\frac{1}{3}$	$4.8^{+0.5}_{-0.3}$ MeV/c^2
strange	s	$-\frac{1}{3}$	95^{+5}_{-5} MeV/c^2
charm	c	$+\frac{2}{3}$	$1.275^{+0.025}_{-0.025}$ GeV/c^2
bottom	b	$-\frac{1}{3}$	$4.18^{+0.03}_{-0.03}$ GeV/c^2
top	t	$+\frac{2}{3}$	160^{+5}_{-4} GeV/c^2

2.1.3 Mediators

Four types of fundamental interactions are known. Because the different interactions are described in terms of the exchange of particles in quantum language, we call these particles mediators. Mediators are particles of spin 1 (i.e., bosons). The strong interaction is responsible for binding quarks together in hadrons. It is mediated by the gluon. The electromagnetic interaction is responsible for the bound states of electrons in nuclei and the intermolecular forces in solids and liquids. It is mediated by the

photon. The weak interaction is responsible for flavor changes. It is mediated by the $W^{\pm}$ and Z^0 bosons. The gravitational interaction is responsible for the attraction between particles with non-zero mass. It is theoretically associated with a spin 2 boson called the graviton, which has not yet been found. Table 2.3 lists these mediators and some of their properties.

Table 2.3: Mediators (Bosons)

Mediator	Force	Charge($\|e\|$)	Mass(GeV/c^2)	(Spin/parity)
photon(γ)	electromagnetic	0	0	1^-
gluon(G)	strong	0	0	1^-
$W^{\pm}$	weak (charged)	±1	81.8	1^-
Z^0	weak (neutral)	0	92.6	1^+
graviton(g)	gravitational	0	0	2^+

2.1.4 Strong Force

Quarks have many other properties besides those shown in Table 2.2. One of these is a property called *color charge*. Each quark will carry one of three colors: *red, green* or *blue*. Similar to the way that electromagnetism describes the interaction between electric charges, *chromodynamics*, or the laws governing the strong force, details the interactions of quarks through their color charge. This color nomenclature is an analogy taken from the field of optics, with the intention of illustrating the fact that quarks are observable only in colorless combinations. The known possibilities are combinations of two or three quarks, known as *hadrons*. *Baryons* refer to the three quark combinations, and must contain one of each color: red + green + blue is equal to white or colorless. *Mesons* are made up of two quarks in a quark-antiquark combination, for instance: blue + $\overline{blue}$ = colorless.

2.1.5 Weak Force and the CKM Matrix

Normally, all free hadrons (except the proton (uud)) will eventually decay into combinations of lighter hadrons, leptons, and/or photons. The possible daughters in a

decay depend on the force that acts as the mediator. Figure 2.2 shows a graphical interpretation of the interactions between the forces and particles of the Standard Model.

The weak force is the only one that allows for the transition of quarks into lighter quarks and leptons into lighter leptons. In addition, the weak force explains decays that require changes in flavor, for example: a neutron (n) decaying to a proton (p) + electron (e) + neutrino (ν_e).

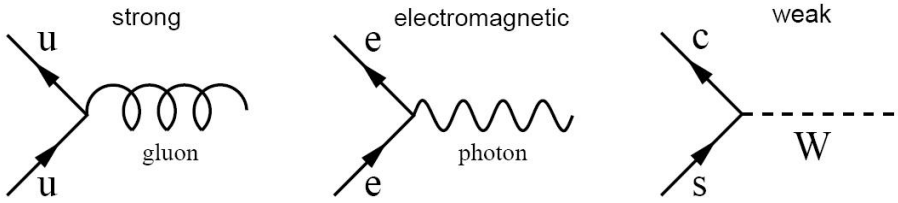

Figure 2.2: Of the three forces included in the Standard Model, only the weak force allows for quarks or leptons to change flavor and generation.

This property of the weak force implies that all stable matter in the universe is made up of only first generation quarks and leptons, which is a consequence of the fact that the weak force not only couples within a generation, but also allows for cross-generational transitions. For quarks, these couplings are summarized in the Cabbibo-Kobayashi-Maskawa (CKM) Matrix,

$$\begin{pmatrix} d' \\ s' \\ b' \end{pmatrix} = \underbrace{\begin{pmatrix} V_{ud} & V_{us} & V_{ub} \\ V_{cd} & V_{cs} & V_{cb} \\ V_{td} & V_{ts} & V_{tb} \end{pmatrix}}_{CKM matrix} \begin{pmatrix} d \\ s \\ b \end{pmatrix}$$

In other words, the weak force does not, see for instance a simple s quark, but rather an s', which is a linear combination of d, s, and b quarks,

$$s' = V_{cd}d + V_{cs}s + V_{cb}b. \tag{2.2}$$

The magnitude of these matrix elements $|Vij|$ is related to the quantum mechanical probability amplitude of a quark changing flavor, for example, an *up-type* quark i transitioning into a *down-type* quark j, within or even between generations. Within the Standard Model, these magnitudes are not calculable from fundamental principles and must be determined experimentally. Curiously, these experimental measurements have revealed a pattern in the CKM matrix. The elements on the matrix diagonal are approximately equal to one, which means that a quark is most likely to make a transition within its own generation. The matrix elements become smaller, almost symmetrically, as one moves off the diagonal. The actual ranges of the elements are summarized in the following CKM matrix [25]:

$$|V_{ij}| = \begin{pmatrix} 0.97419 \pm 0.00022 & 0.2257 \pm 0.0010 & 0.00359 \pm 0.00016 \\ 0.2256 \pm 0.0010 & 0.97334 \pm 0.00023 & 0.0415^{+0.0010}_{-0.0011} \\ 0.00847^{+0.00026}_{-0.00037} & 0.0407 \pm 0.0010 & 0.999133^{+0.000044}_{-0.000043} \end{pmatrix}.$$

Based on this result, interactions that involve matrix elements that lie on the diagonal are considered "Cabbibo Favored" while those that involve off-diagonal elements are called "Cabbibo Suppressed" [26]. The CKM matrix is commonly parametrized by three mixing angles and a CP-violating phase. The standard choice is [27]

$$|V_{ij}| = \begin{pmatrix} c_{12}c_{13} & s_{12}c_{13} & s_{13}e^{-i\delta} \\ -s_{12}c_{23} - c_{12}s_{23}s_{13}e^{i\delta} & c_{12}c_{23} - s_{12}s_{23}s_{13}e^{i\delta} & s_{23}c_{13} \\ -s_{12}s_{23} - c_{12}c_{23}s_{13}e^{i\delta} & -c_{12}s_{23} - s_{12}c_{23}s_{13}e^{i\delta} & c_{23}c_{13} \end{pmatrix},$$

where $s_{ij} = \sin\theta_{ij}$, $c_{ij} = \cos\theta_{ij}$, and δ is the KM phase responsible for all CP-violating phenomena in the flavor-changing processes in the SM. The angles θ_{ij} can be chosen

to lie in the first quadrant so that s_{ij} and c_{ij} are positive. Experimentally, it has been found that $s_{13} \ll s_{23} \ll s_{12} \ll 1$. This hierarchy is reflected in the Wolfenstein parameterization, given by

$$s_{12} = \lambda = \frac{|V_{us}|}{\sqrt{|V_{ud}|^2 + |V_{us}|^2}}, \; s_{23} = A\lambda^2 = \lambda \left| \frac{|V_{cb}|}{|V_{us}|} \right|, s_{13}e^{i\delta} = A\lambda^3(\rho + i\eta). \tag{2.3}$$

This parametrization is an expansion using the parameter $\lambda \approx 0.23$, which is the sine of the Cabbibo angle for the up and strange quark coupling, as well as three additional real parameters: ρ, η, and A. The parameter η represents the CP-violating phase. Traditionally, the CKM matrix is expressed in terms of λ, ρ, η, and A in the following approximation:

$$|V_{CKM}| = \begin{pmatrix} 1 - \lambda^2/2 & \lambda & A\lambda^3(-i\eta) \\ -\lambda & 1 - \lambda^2/2 & A\lambda^2 \\ A\lambda^3(1 - \rho - i\eta) & -A\lambda^2 & 1 \end{pmatrix} + O(\lambda^4)$$

2.1.6 Weakly decaying V^0's

V^0's are relatively long-lived ($O(10^{-10}\,s)$) neutral particles containing one strange quark. The three particles in this category are K_s^0 mesons, Λ, and $\overline{\Lambda}$ baryons. V^0's demonstrate a weak decay involving a flavor change (Figures 2.3 and 2.4), which explains their long lifetime. Relevant properties of V^0-decays are summarized in Table 2.4.

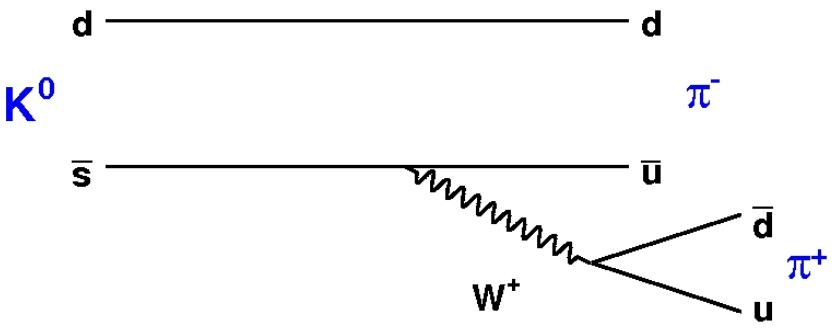

Figure 2.3: $K_s^0 \to \pi^+ \pi^-$ decay: we can observe the flavor change from an $\overline{s}$ to an $\overline{u}$ quark.

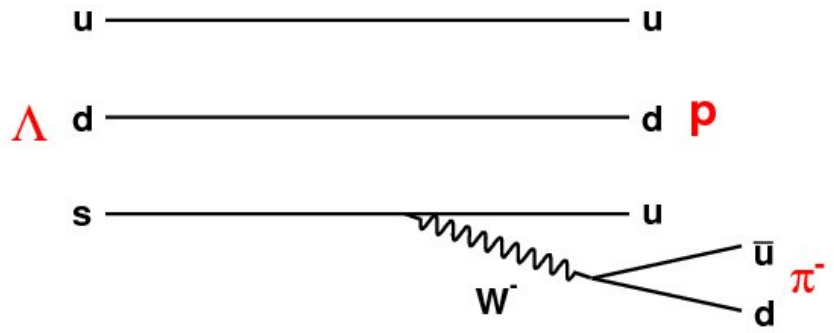

Figure 2.4: $\Lambda \to$ p π^- decay

Table 2.4: V^0 decay channels and other relevant quantities

particle	K_s^0	Λ	$\overline{\Lambda}$
quark content	$1/\sqrt{2}\ (d\bar{s} - s\bar{d})$	uds	$\bar{u}\bar{d}\bar{s}$
mass(MeV/c^2)	497.614 ± 0.024	1115.683 ± 0.006	1115.683 ± 0.006
primary decay	$K_s^0 \rightarrow \pi^+\pi^-$	$\Lambda \rightarrow$ p π^-	$\overline{\Lambda}\rightarrow \overline{p}\ \pi^+$
branching fraction	(69.2 ± 0.05) %	(69.3 ± 0.5) %	(69.3 ± 0.5) %
$c\tau$	2.6842cm	7.89 cm	7.89 cm

2.2 QCD

2.2.1 Lagrangian

Quantum chromodynamics (QCD) is the gauge theory of strong interaction. The chromo in the name is because in this theory, quarks possess an internal property called color. Gauge transformations in QCD are precisely local transformations between different colored quarks. There are eight gauge bosons that mediate the strong interactions, called the gluons. The mathematical notation that follows is that used by R.K. Ellis [28].

QCD Lagrangian density is as follows:

$$\mathcal{L}_{QCD} = \mathcal{L}_{classical} + \mathcal{L}_{gauge-fixing} + \mathcal{L}_{ghost} \tag{2.5}$$

2.2.2 Classical Density

The classical Lagrangian density, invariant under SU(3) gauge transformations, is

$$\mathcal{L}_{classical} = -\frac{1}{4}F^2[A] + \sum_{flavors} \bar{q_a}(i\not{D} - m)_{ab}q_b \tag{2.6}$$

These terms define the interaction of spin-1/2 quarks of mass m with massless spin-1 gluons. The field strength tensor $F^A_{\alpha,\beta}$ derived from the gluon field $\mathcal{A}^A_\alpha$ is,

$$F^A_{\alpha,\beta} = \left[\partial_\alpha \mathcal{A}^A_\beta - \partial_\beta \mathcal{A}^A_\alpha - g f^{ABC} \mathcal{A}^B_\alpha \mathcal{A}^C_\beta\right] \tag{2.7}$$

where the indexes A, B, C run over the eight degrees of freedom in color from the gluon field. The *non-Abelian* term gf^{ABC} distinguishes QCD from quantum electrodynamics (QED). It results in cubic and quartic gluon self-interactions as well as asymptotic freedom. The parameter g is the coupling constant that determines the strength of the interaction between colored quanta, and the f^{ABC} are the structure constants of the SU(3) color group. The sum $\sum_{flavors} \bar{q_a}(i\not{D} - m)_{ab} q_b$ runs over the different flavors of quarks. The q_a are the quark fields in the triplet representation of the color group, and $\not{D}$ is symbolic notation for $\gamma_\mu D^\mu$, where γ_μ are the gamma matrices, which are non-commutative, and D^μ are the covariant derivatives.

2.2.3 Gauge Fixing

The term $\mathcal{L}_{gauge-fixing}$ is introduced into the QCD Lagrangian to enable perturbation theory. It is not possible to define a propagator for the gluon field without choosing a gauge. Depending on which gauge is chosen, the ghost Lagrangian $\mathcal{L}_{ghost}$ may be needed to cancel unphysical degrees of freedom which would otherwise propagate in covariant gauges. As an example, the choice

$$\mathcal{L}_{gauge-fixing} = \frac{1}{2\lambda}\left(\partial_\alpha \mathcal{A}^A_\alpha\right)^2 \tag{2.8}$$

fixes the class of covariant gauges with gauge parameter λ. In QCD, it must be supplemented by a ghost Lagrangian given by

$$\mathcal{L}_{ghost} = \partial_\alpha \eta^{A\dagger}\left(D^\alpha_{AB}\eta^B\right) \tag{2.9}$$

where η^A is a complex scalar field that obeys Fermi statistics.

2.2.4 Asymptotic Freedom

Asymptotic freedom in QCD explains why perturbation methods are useful in the high energy regime. The problem is that the QCD gauge coupling, which is related to the strong coupling α_s via

$$\alpha_s = \frac{g^2}{4\pi} \tag{2.10}$$

is large. For excessively large values of α_s, reliable calculations are not possible with perturbation theory. Renormalization is required to remove divergences. This difficulty is avoided by using a coupling constant that is renormalized based on the energy scale. In QCD, this is called the running coupling constant. The running of α_s is determined by the β function (Figure 2.5), which has the expansion:

$$\beta(\alpha_s) = -b\alpha_s^2(1 + b'\alpha_s) + O(\alpha_s^4) \tag{2.11}$$

where the first coefficients are $b = \frac{(11C_A - 2N_f)}{12\pi}$ and $b' = \frac{(17C_A^2 - 5C_A N_f - 3C_f N_f)}{2\pi(11C_A - 2N_f)}$. The parameter N_f is the number of "active" light flavors.

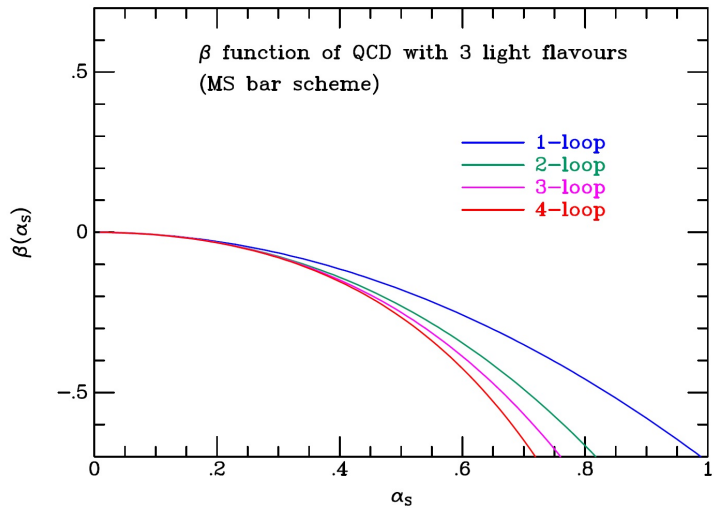

Figure 2.5: β as a function of α_s using 3 active light flavors [4].

This renormalization introduces a second mass scale μ, which indicates the point at which the divergences are to be removed. Therefore, the renormalized coupling α_s depends on the choice of the subtraction point μ.

$$\alpha_s\left(Q^2\right) = \frac{\alpha_s\left(\mu^2\right)}{1 + \alpha_s\left(\mu^2\right) b \ln \frac{Q^2}{\mu^2}} \tag{2.12}$$

As we move into the high energy regime, $\ln \frac{Q^2}{\mu^2}$ becomes large and α_s drops to zero, allowing for perturbation theory to be used. This property is called asymptotic freedom.

2.2.5 Confinement

Asymptotic freedom tells us that α_s becomes quite small at large Q, meaning that the coupling between quarks becomes weaker at shorter distances (corresponding to higher energy scales). It also follows that as Q becomes smaller, α_s becomes large, which implies that the coupling grows at larger distances. Therefore, we can never isolate a quark (or a gluon) at large distances because as we pull the quarks apart, the binding strength grows and we require more energy. When the energy contained in the string of bound gluons and quarks become large enough, the color-string breaks and more hadrons are created, resulting in more colorless hadrons, but no isolated colored quarks. This explains why neither gluons nor quarks have been seen in a laboratory. The only free particles which can be observed at macroscopic distances from each other are color singlets. This mechanism is known as quark confinement.

2.2.6 Color Wave-Functions

With the introduction of color, quarks of any kind may exist in three equivalent states. However, hadrons are neutral, or colorless. Therefore, the wave functions modeling baryons and mesons must cancel out the color quantum number.

Baryons must obey Fermi-Dirac statistics, and so their wave function must be antisymmetric [29]. However, it must also be color neutral. This requires all three

quarks to have a different color (e.g., red-green-blue = white or colorless). The color part of the wavefunction is given by

$$\psi = 1/\sqrt{6}\epsilon_{abc}q_a(1)q_b(2)q_c(3) \tag{2.13}$$

where ϵ is a totally antisymmetric tensor and the sum is taken over all color configurations of the three quarks. The wavefunction transforms as a color singlet, i.e., the bound state of the three quarks is color neutral.

Mesons are the bound states of a quark and an antiquark. Here, the color part of the wavefunction is

$$\psi = \frac{1}{\sqrt{3}}\delta_{ab}\bar{q}_a(1)q_b(2) \tag{2.14}$$

where δ_{ab} is the Kronecker delta. Being a superposition of color-anticolor combinations, the wavefunction once again transforms as a color singlet.

2.2.7 Multi-Hadron Production

Hadron production in high energy collisions is not fully understood. Despite this, there are many QCD-based phenomenological models which show good agreement with observed results. Often, e^+e- collisions are used to study strong interactions, since there are no spectator quarks which can mask the process of interest [30]. However, strangeness production in hadron-hadron collisions is also a good probe for QCD models, since there are no strange (valence) quarks in the initial state. Therefore, strange quarks must come from strong interactions. The most widely used model of parton fragmentation is based on partons splitting into quark-antiquark pairs that finally recombine into the observed hadrons.

Generally, hadron production follows two steps: Firstly, a parton shower in which an initial parton is far from the mass-shell evolves into a cascade of partons nearer to mass-shell. This stage can be modeled using perturbative QCD with certain assumptions. Secondly, the process of hadronization occurs, in which the partons close to the mass shell form hadrons. This process becomes non-perturbative, and is where

phenomenological models are used. There are two models that are widely used to simulate hadron production based on these processes. These are the HERWIG model [5] and the Lund model [31].

2.2.8 Parton Shower

A parton shower is an iterative Markov branching process in which a highly excited $q\bar{q}$ system evolves to a system of partons with lower virtuality by radiating gluons and producing new $q\bar{q}$ pairs according to the leading log QCD probabilities [30]. The basic picture of the parton shower development is illustrated in Figure 2.6. Each vertex represents the splitting of a parton into two others of lower virtualities. The probability of such a splitting is proportional to the running coupling constant α_s at an appropriate scale [5].

2.2.9 Hadronization

After the parton shower process, the partons close to the mass shell join to form hadrons. This is usually described by two methods: clusters and string fragmentation.

The cluster scheme is simple; in the later stage of hadronization, when the virtual mass of a parton reaches a certain cutoff (m_g), the evolution of this parton stops. As well, final gluons are forced to split into $q\bar{q}$ pairs. Neighboring $q\bar{q}$ pairs along the color flux lines are combined to form colorless clusters. These clusters decay into one or two hadrons. Such hadrons include both final particles and resonances which will decay further. This is the scheme used in the HERWIG [5] model.

String fragmentation is based on the confinement between quarks. Since QCD suggests a force which grows proportionally with the distance between quarks, this model assumes that this force is provided by a string that holds them together. As the $\bar{q}$ and the q move apart in a boosted $q\bar{q}$ pair, their kinetic energy is gradually converted to potential energy stored in the string. Fluctuations in the system can lead to a transition where energy stored in the string is converted into a new quark-antiquark pair. A new $q\bar{q}$ pair is created at the breaking point from the string, and the original system becomes two separate color singlets, i.e., $q\bar{q} \rightarrow q\bar{q'} + q'\bar{q}$ [6] as

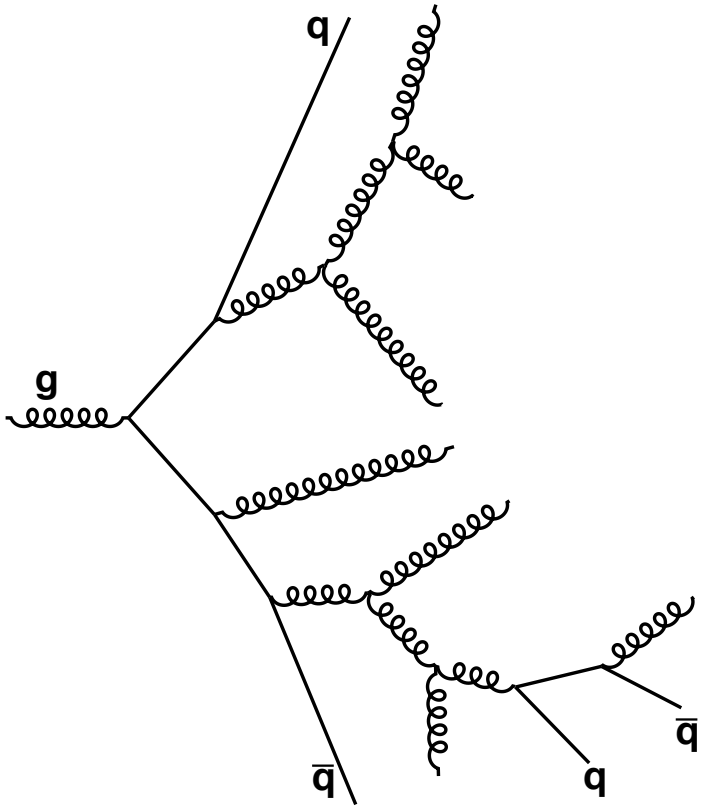

Figure 2.6: Perturbative QCD branching process following g $\rightarrow q\bar{q}$ [5].

pictured in Figure 2.7. This is the scheme used by the Lund model [31] which is used in PYTHIA.

2.2.10 Strange Quark Production

Strange quark production is an area of opportunity in non-perturbative QCD. So far, it is understood that strange quarks are produced mainly in the fragmentation stage, when the color field in the string provides enough energy to create an $s\bar{s}$ pair. Since there are no spectator s quarks present in hadron-hadron collisions, the observation of strange particles such as V^0's is a good probe for hadronization models.

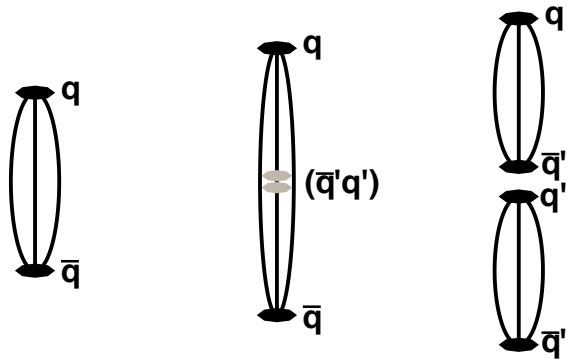

Figure 2.7: Schematic picture of the formation of hadrons by the string breaking process [6].

Chapter 3

The LHCb Experiment

3.1 The Large Hadron Collider (LHC)

The Large Hadron Collider (LHC) is a high energy circular synchrotron accelerator. It sits in a tunnel with a circumference of 27 km that previously housed the LEP accelerator. The tunnel is buried around 50 to 175 m underground. It is situated between the Swiss and French borders on the outskirts of Geneva (Figure 3.1). It is designed for colliding two opposing circulating beams of protons and lead nuclei at a center of mass energy of 14 TeV and 2.8 TeV, respectively.

Figure 3.1: Aerial view of the LHC with SPS [7].

Before particles reach the LHC, they are accelerated in several steps by a series of accelerators (Figure 3.2). A brief description of the proton cycle used is as follows: Protons are obtained from hydrogen gas inside a metal cylinder called the Duoplasmatron. There, an electrical field is used to break down the gas into its constituent protons and electrons. Protons are then accelerated by an accelerating voltage of 90 kV and leave the Duoplasmatron at 1.4 % of the speed of light. Afterwards they are sent to a radio frequency quadrupole (RFQ), an accelerating component that both speeds up and focuses the particle beam. After reaching an energy of 750 keV, the particles are sent from the quadrupole to the linear accelerator (LINAC2). There, the protons are accelerated up to 50 MeV and fed to the BOOSTER where they are boosted to 1 GeV before entering the Proton Synchrotron (PS) and being accelerated to 26 GeV. After the PS, the proton bunches enter the Super Proton Synchrotron (SPS) where they are energized up to 450 GeV and finally enter the LHC through the T12 and T18 tunnels.

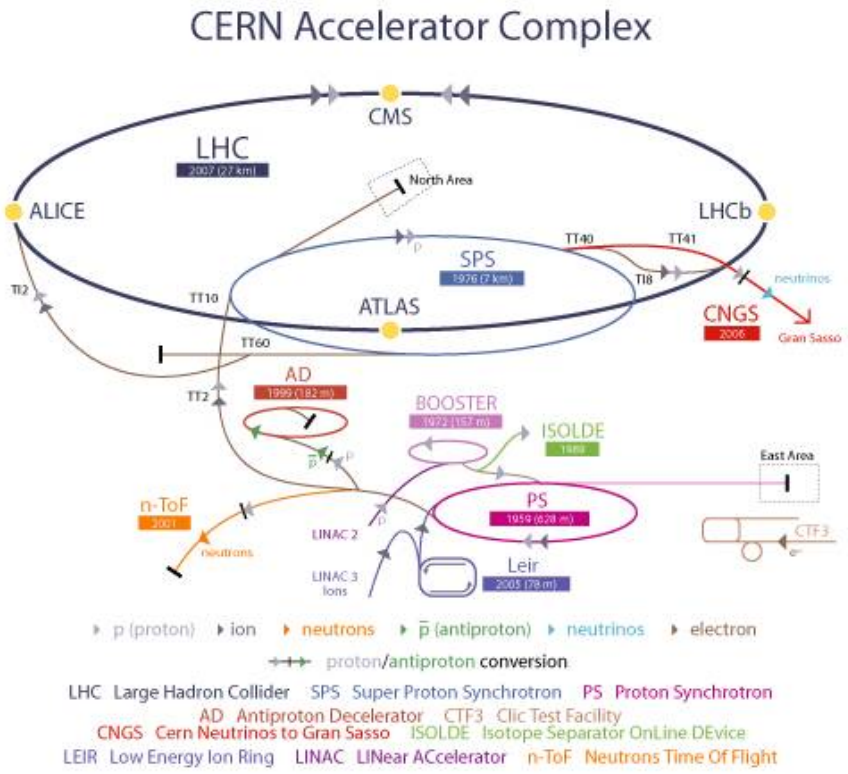

Figure 3.2: The CERN Accelerator Complex [8].

In the LHC, protons circulate in both a clockwise and an anticlockwise direction. To keep the proton beams circulating inside the ring, the LHC has around 1200 dipole magnets (Fig 3.3) that provide a magnetic field of 8.34 T (for 7 TeV beams). These are superconducting magnets cooled down to 1.9 K using superfluid helium. Additionally, the beam is focused by around 400 quadrupole magnets, and is accelerated by radiofrequency (RF) cavities. At nominal conditions, the LHC should collide proton bunches at a frequency of 40 MHz, and provide a luminosity of 10^{34} cm^{-2}s^{-1} at the interaction points.

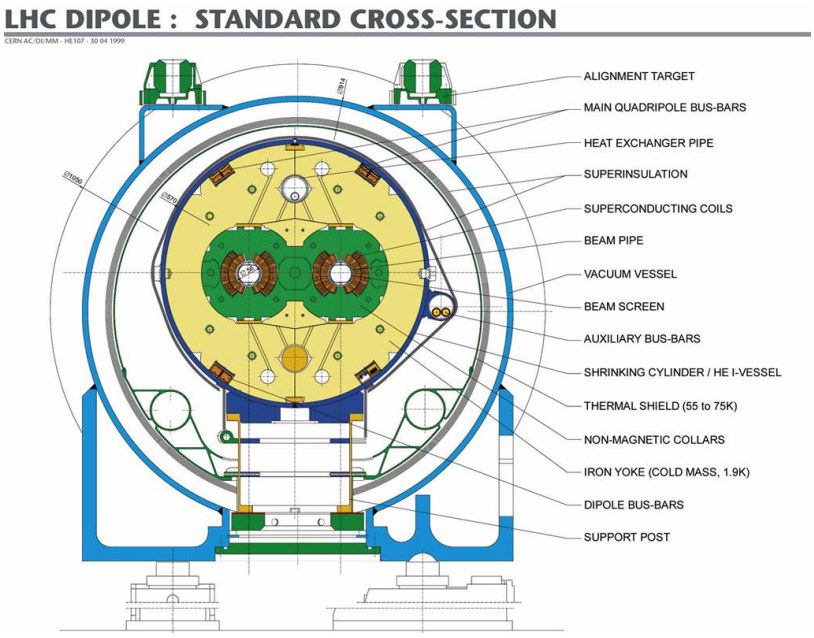

Figure 3.3: Cross-section schematic view of an LHC dipole magnet [9].

Figure 3.4 shows the location of the four major experiments on the LHC: ATLAS (A Toroidal LHC ApparatuS), CMS (Compact Muon Solenoid), ALICE (A Large Ion Collider Experiment), and LHCb (Large Hadron Collider beauty). ATLAS and CMS are focused on finding the Higgs Boson and evidence for supersymmetry. ALICE studies quark-gluon plasma formed in Pb-Pb collisions. LHCb focuses on studying CP violation and rare decays in the B sector.

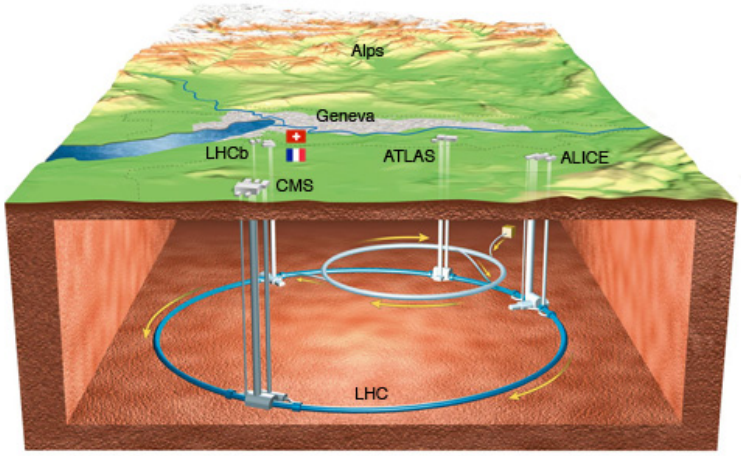

Figure 3.4: Map of the LHC showing the stations for its four major experiments [7].

3.1.1 LHC Performance

In November 2009, the LHC succeeded in colliding protons at an energy of 450 GeV per beam. In 2010, the multi-TeV era started when $\sqrt{s} = 7$ TeV collisions were achieved with a peak luminosity of $0.2{\times}10^{33}$ cm^{-2}s^{-1}, delivering a total integrated luminosity of 47 pb^{-1}. In 2011, the collision energy continued at $\sqrt{s} = 7$ TeV, with a peak luminosity of $3.6{\times}10^{33}$ cm^{-2} s^{-1} and a total integrated luminosity of 5.5 fb^{-1} [32]. It was in 2012 that the LHC raised the collision energy up to $\sqrt{s} = 8$ TeV, and more than 20 fb^{-1} were delivered at the main interaction points.

3.2 The LHCb Experiment

In high energy hadronic collisions, $b\bar{b}$ pairs are mostly produced by gluon-gluon fusion. This mechanism consists of two virtual gluons that collide to form a quark anti-quark pair. Due to the momentum distribution of the gluons inside the colliding protons, in most cases the collision happens between one gluon carrying a large part of the proton momentum and another gluon with much less momentum. This causes the $b\bar{b}$ produced by this interaction to be strongly boosted in the forward direction. Consequently, the hadronization results in B and $\bar{B}$ mesons with a very narrow angular distribution (Figure 3.5). This fact led to LHCb's single–arm spectrometer design.

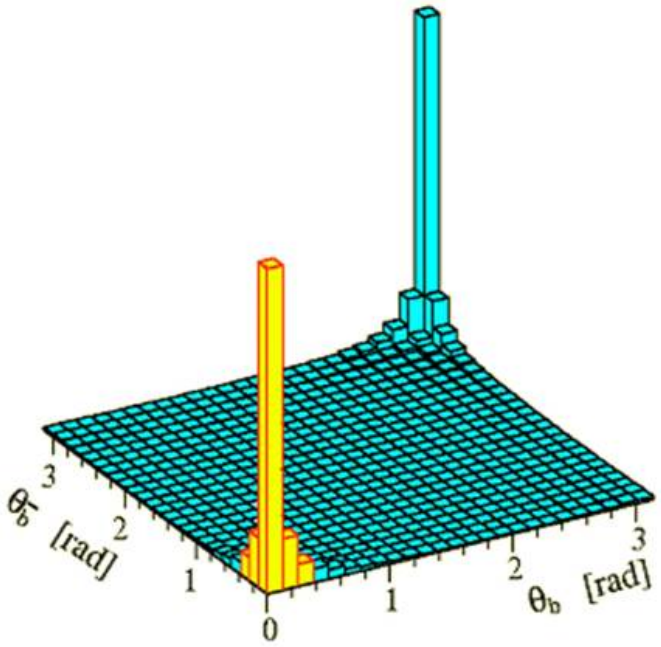

Figure 3.5: Angular distribution of $b\bar{b}$ pairs produced in high energy pp collisions [10].

The angular acceptance of the LHCb detector extends from approximately 10 mrad around the beam axis to 300 mrad in the magnetic bending plane and 250 mrad in the non-bending plane [11].

What follows is a brief description of the functions of the LHCb subdetectors shown in Figure 3.6 (from left to right):

- VELO (Vertex Locator): accurately reconstructs the primary and secondary vertices of heavy flavor decays.
- RICH1: provides particle identification for low momentum particles (from 1 to 60 GeV/c).
- TT (Tracker Turicensis): observes the trajectories of low momentum particles.
- Magnet: a 4 Tm magnet used to bend the trajectories of particles in order to allow for the measurement of their momentum.
- T1, T2, and T3 stations: observe the trajectories of the particles.
- RICH2: provides particle identification for high momentum particles.
- ECAL: measures the energy of electromagnetic interacting particles.
- HCAL: measures the energy of hadronic particles.
- Muon Stations: separate muons from the other charged particles.

3.3 Tracking

The principle task of the tracking system is to provide efficient reconstruction of charged-particle tracks. These are then used to determine the momenta of charged particles and to reconstruct primary vertices. The LHCb tracking system consists of the vertex locator system (VELO), the Tracker Turicensis(TT) upstream of the dipole magnet, and the T Stations T1-T3 downstream of the magnet. T1-T3 are composed of silicon microstrip detectors in the region close to the beam pipe (Inner Tracker IT) and straw tubes on the outer region (Outer Tracker OT). VELO and TT are fully equipped with silicon microstrip detectors. The TT and IT were developed in a common project called the Silicon Tracker (ST).

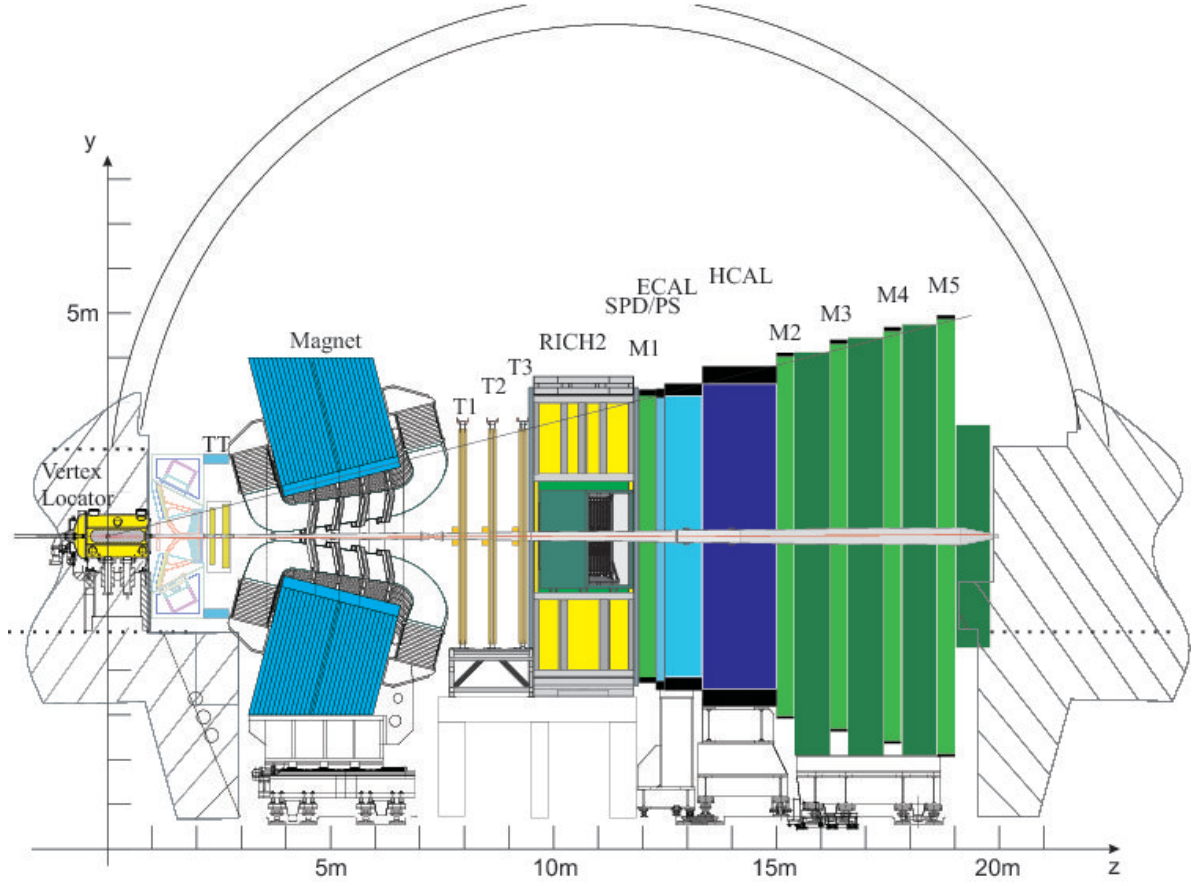

Figure 3.6: z view of the LHCb Detector [11].

3.3.1 Vertex locator

The Vertex Locator (VELO) plays a fundamental role in the LHCb detector because it is able to precisely measure track coordinates close to the interaction region, which are used to accurately build the primary and secondary vertices of the decays of short-lived particles. This vertex identification and separation is essential for CP Violation measurements using B mesons, in order to provide an accurate measurement of their lifetimes and the impact parameter of the particles. The VELO consists of a series of 42 (21 on each side) half-circular silicon modules (Figure 3.7) arranged along the beam axis. Each module provides a measurement of the r and ϕ coordinates, and is placed around the interaction region (Figure 3.8, Top).

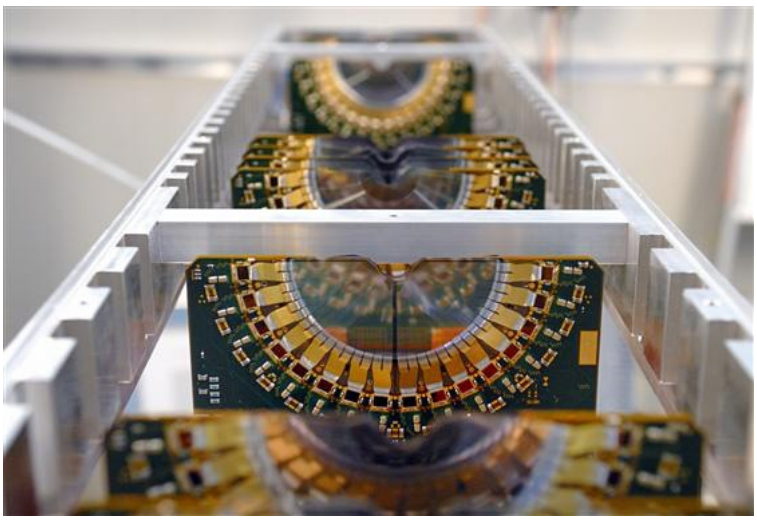

Figure 3.7: VELO's silicon detector modules [11].

The VELO sensors have to be retracted from the beam line during injection in order to prevent damage from the LHC proton beams. When the beam is stable and everything is ready for data acquisition, the sensors are moved into the closed position, in which the two halves of the VELO overlap (Figure 3.8, Bottom).

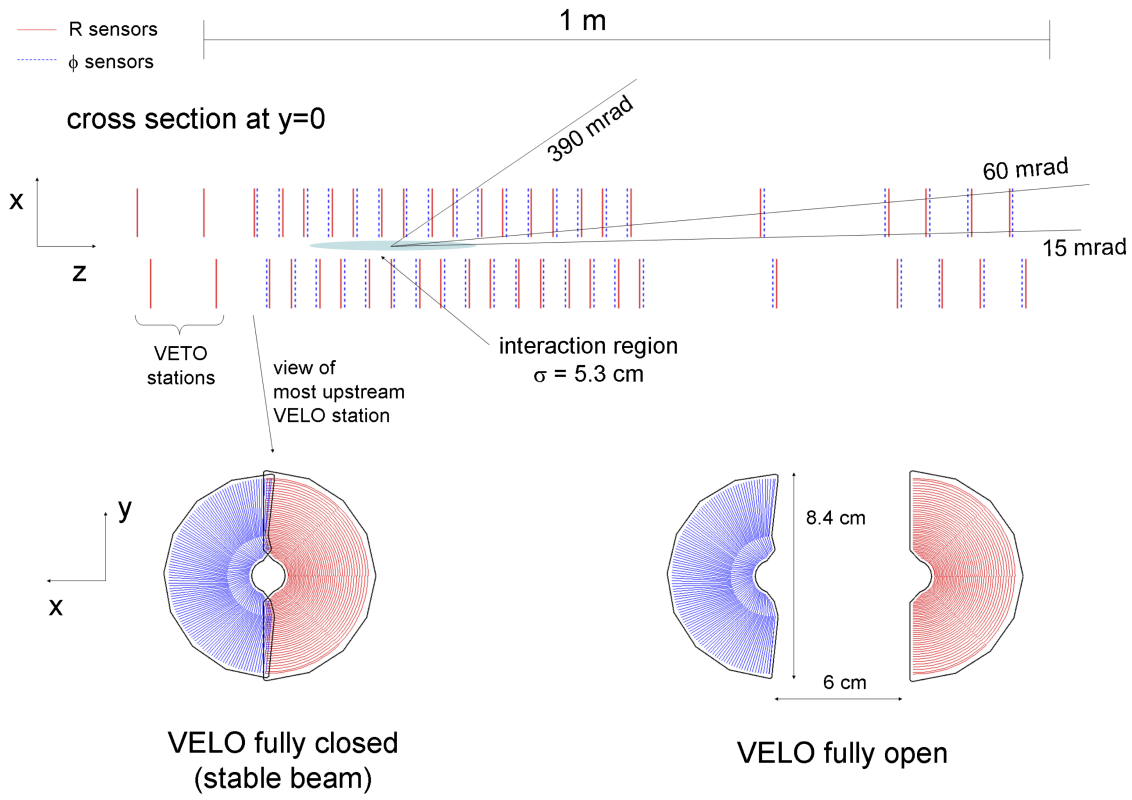

Figure 3.8: Top: Cross-section of the VELO sensors in the xz-plane, indicating the angular acceptance of the detector and the relative arrangement of the stations. The distance from the first to the last station is 106.5 cm. Bottom: Sketch of a VELO station in the closed and fully open positions [11].

In order to perform an efficient vertex reconstruction that meets the performance requirements of the LHCb experiment, the VELO was designed with the following criteria:

- A signal to noise ratio (S/N) greater than 14.
- An overall channel efficiency of at least 99%.
- A spatial cluster resolution of around 4 μm.
- Less than 0.3 of the peak signal remaining after 25 ns.
- An angular acceptance in the pseudorapidity range $1.6 < \eta < 4.9$ for particles emerging from the primary vertex in the range $|z| \leq 10.6$ cm.
- Full azimuthal acceptance; to facilitate alignment, the two detector halves are required to overlap (Figure 3.8).
- Cylindrical geometry (Rϕ coordinates) to enable fast reconstruction of tracks and vertices in the LHCb trigger, and to achieve optimal impact parameter resolution.

The sensors use n-implants in n-bulk technology with strip isolation achieved through the use of a p-spray. The minimum pitch achievable using this technology was approximately 32 μm. This choice was due to the severe radiation environment close to the beam axis. For both the R and ϕ sensors the minimum pitch is designed to be at the inner radius in order to optimize the vertex resolution (Figure 3.9). Both sensors are 300 μm thick.

For the R-sensors, the diode implants are concentric semi-circles with their center at the nominal LHC beam axis. Each strip is divided into four 45° regions to minimize occupancy. The pitch increases linearly from 38 μm at the inner radius to 101.6 μm in the outer radius. The ϕ sensor is intended to report the orthogonal coordinate to the R-sensor. To avoid high occupancy, it is divided into inner and outer regions as shown in Figure 3.9. The pitch varies proportional to the radius in both regions.

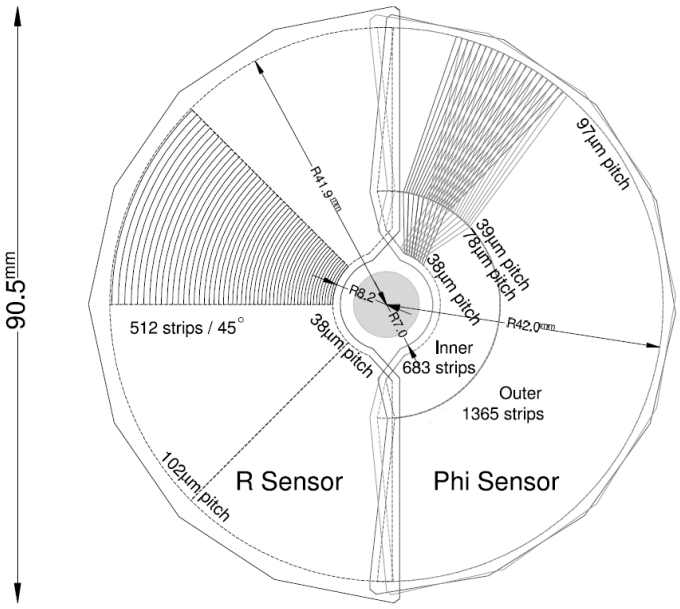

Figure 3.9: Sketch illustrating the Rϕ geometry of the VELO sensors [11].

The outer region has a pitch of 39.3–97 μm, while the inner has a pitch of 38–78.3 μm; the separation between them is given by the radius of 17.25 mm. In total, there are 42 R sensors and 42 ϕ sensors in both VELO halves.

3.3.2 Tracker Turicensis

The Tracker Turicensis (TT) is located downstream of RICH 1 and in front of the entrance of the LHCb dipole magnet. It has a double purpose: to provide fast tracking information on high IP tracks (mainly their transverse momentum) to the Level-1 trigger, and, in offline analysis, to reconstruct the trajectories of long-lived neutral particles that decay outside the VELO, as well as low momentum particles which are bent out of the LHCb experiment before reaching stations T1-T3.

Figure 3.10 shows a view of the TT layout. It consists of four layers. The first and last have vertical readout strips (x-layers) and the second and third (inner)

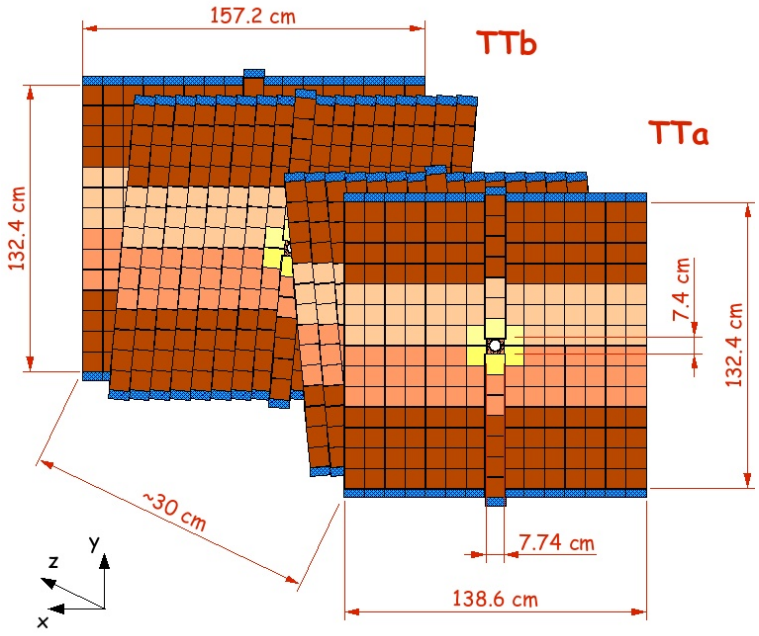

Figure 3.10: Schematic showing the xuvx layout of the TT [12].

layers have readout strips rotated by a stereo angle of $+5°$ and $-5°$, respectively. The four layers are arranged into two pairs or stations, and the approximate separation between stations is 27 cm. The first station (TTa) is centered around z = 232 cm, and the second (TTb) around z = 262 cm. In total, the TT has an active area of 8.4 m^2, covered by silicon microstrip detectors. The active area covers the nominal acceptance of the LHCb detector, i.e., ± 300 mrad in the horizontal plane and ± 250 in the vertical. For TTa this means a width of 143.5 cm and a height of 118.5 cm, and for TTb a width of 162.1 cm and a height of 133.8 cm.

Sensors are organized in half-modules, two of which are required to cover a layer from side to side. The layout of the half-modules is illustrated in Figures 3.11(a) and 3.11(b). They consist of seven silicon sensors with a stack of two or three readout hybrids at one end. Half-modules close to the beam pipe (4-2-1 type) are situated where the particle density is highest, and the seven sensors are organized into three readout sectors: L, M, and K (Figure 3.11(a)). In the other half-modules (4-3 type) the sensors are organized into two readout units, L and M (Figure 3.11(b)). The silicon sensors are 500 μm thick, single-sided p^+-on-n sensors. They are 9.64 cm wide and 9.44 cm long, and carry 512 readout strips with a strip pitch of 183 μm.

3.3.3 Inner Tracker

In each of the tracking stations T1-T3, the Inner Tracker covers a cross-shaped area around the beam pipe (Figure 3.12). This covers only 1.3 % of the sensitive area of the T Tracking stations, but approximately 20 % of all charged particles produced close to the interaction point and passing through the previous tracking stations pass through this area. Each of the three IT stations consists of four detection layers, in a similar way to the TT. The IT layers feature an xuvx arrangement, with x-layers (Figure 3.13(a)) having vertical readout strips and stereo layers (u- or v- layers, Figure 3.13(b)) with strips rotated by a stereo angle of $\pm 5°$.

Each detector layer consists of seven modules. Adjacent modules in a layer are separated by 4 mm in the z direction and overlap by 3 mm in the x direction to

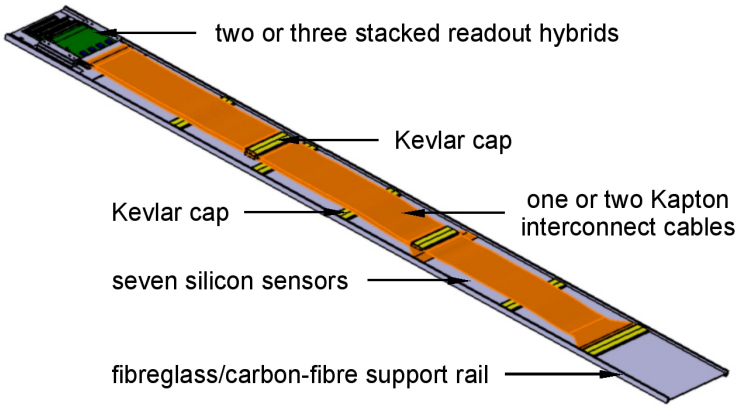

(a) 4-2-1 type

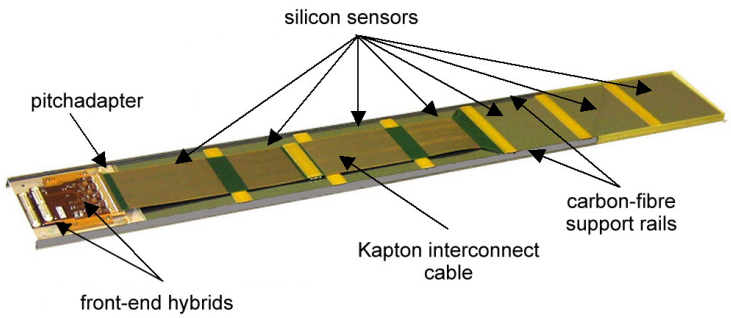

(b) 4-3 type

Figure 3.11: TT detector modules [11].

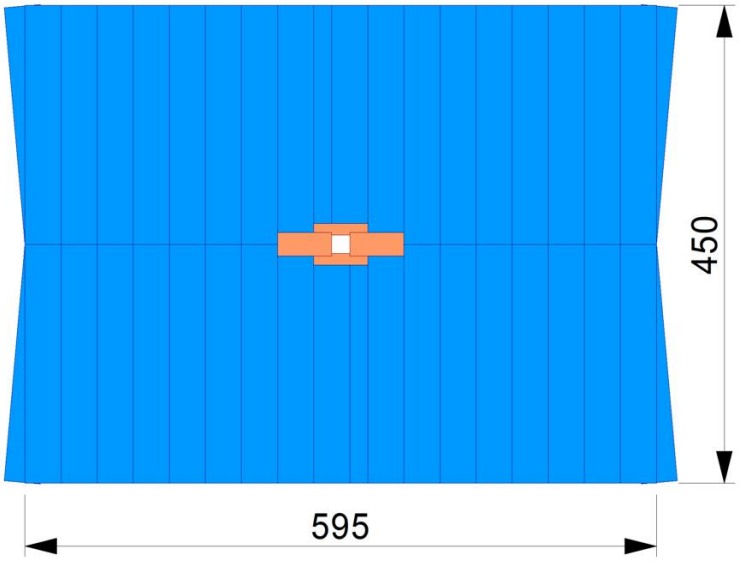

Figure 3.12: Front view of a T station [11].

avoid acceptance gaps and to facilitate relative alignment of the modules. As seen in Figures 3.13(a) and 3.13(b), detector modules on the left and right of the beam pipe consist of two silicon sensors and a readout hybrid, while the modules above and below the beam pipe consist of only a single silicon sensor and a readout hybrid.

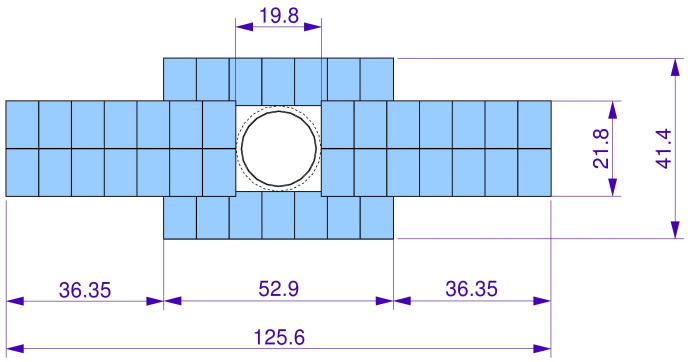

(a) x-layer

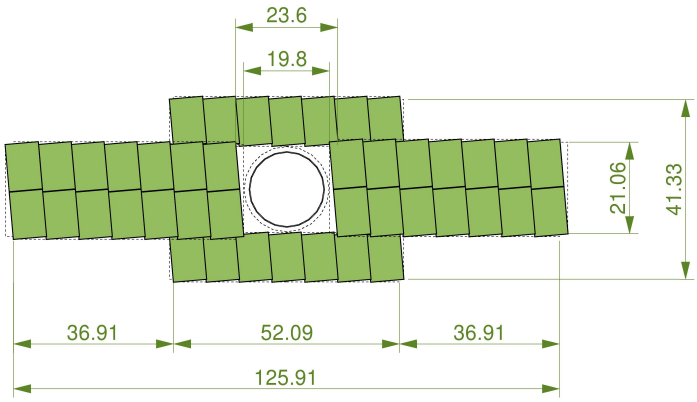

(b) stereo layer

Figure 3.13: IT detector modules layouts. Dimensions are given in cm and refer to the sensitive surface covered by the Inner Tracker [11].

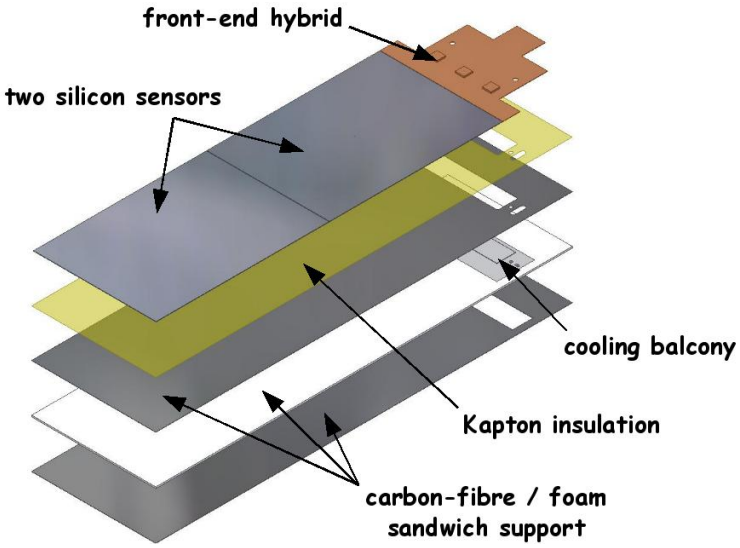

Figure 3.14: Schematic view of a two-sensor IT module [11].

In both types of modules, the silicon sensors are single-sided p^+-on-n sensors, 7.6 cm wide and 11 cm long, and carry 384 readout strips with a pitch of 198 μm. For the one-sensor modules, the silicon sensors are 320 μm thick, and for the two-sensor modules they are 410 μm thick.

3.3.4 Outer Tracker

The LHCb Outer Tracker (OT) is intended to cover most of the acceptance of the LHCb experiment ($\pm$ 300 mrad horizontally and $\pm$ 250 mrad vertically). Situated downstream of the magnet, this corresponds to an active area of $5971 \times 4850\,\mathrm{mm}^2$. The OT is a drift-time detector composed of several modules of gas-tight straw tubes. Detector modules are arranged in three stations (Figure 3.15). Similar to the IT, each station consists of four layers arranged in an x-u-v-x geometry.

Each module has two staggered layers of drift tubes with inner diameters of 4.9 mm (Figure 3.16). The filling of the tubes is a gas mixture made up of argon (70%)

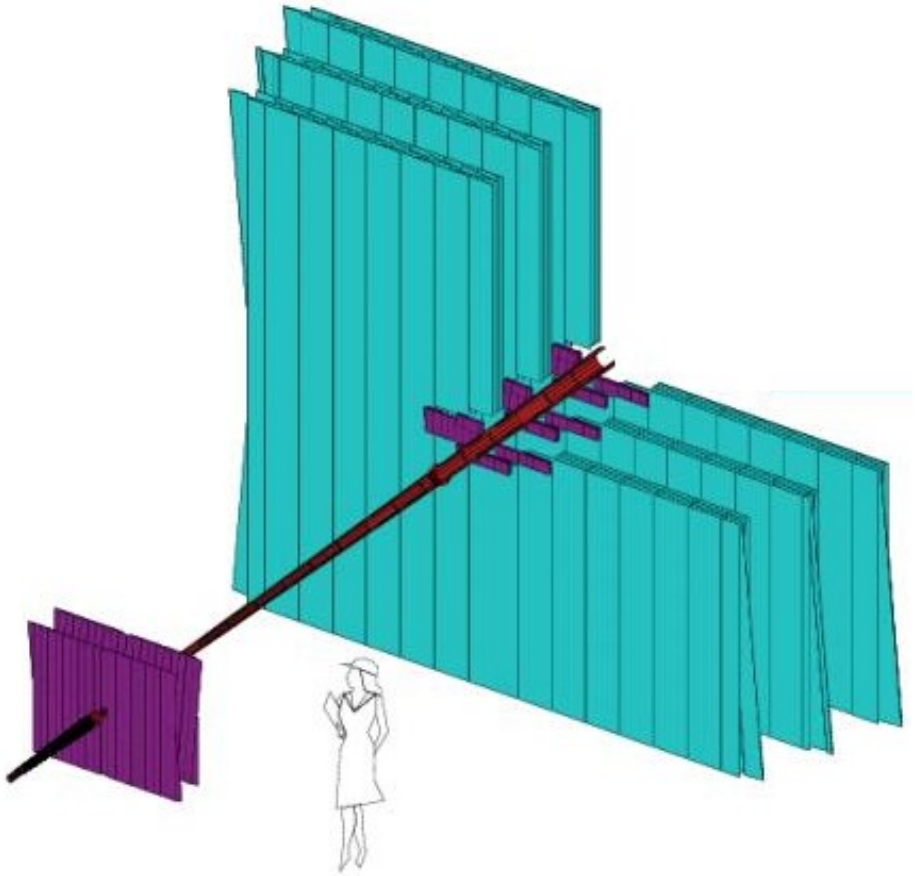

Figure 3.15: Arrangement of OT straw-tube modules in layers and stations [11].

and CO_2 (30%), which results in a drift time below 50 ns and a drift-coordinate resolution of around 200 μm. The intended momentum resolution is $\delta p/p = 4$ %, in order to achieve a mass window of 10 MeV/c^2 for the $B_s^0 \rightarrow D_s^- \pi^+$ channel.

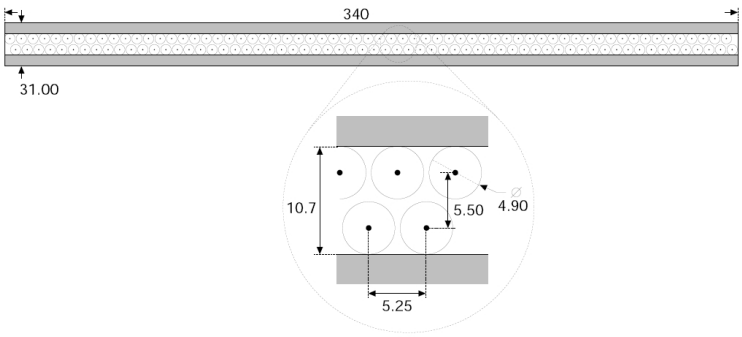

Figure 3.16: Cross section of an OT module [11].

3.4 RICH

In order to obtain a good performance in measuring B hadron decays, it is essential to separate kaons from pions, and therefore, particle identification (PID) is fundamental for the LHCb. At large polar angles the momentum spectrum is softer, while at small polar angles the momentum spectrum is harder. To account for this, the LHCb detector has 2 RICH subdetectors (RICH1 and RICH2) to cover the full momentum spectrum. In both RICH subdetectors, the focusing of the Cherenkov light is accomplished using a combination of spherical and flat mirrors to reflect the image out of the spectrometer's acceptance. Both use Hybrid Photon Detectors (HPD's) to detect the Cherenkov photons in the wavelength range from 200–600 nm.

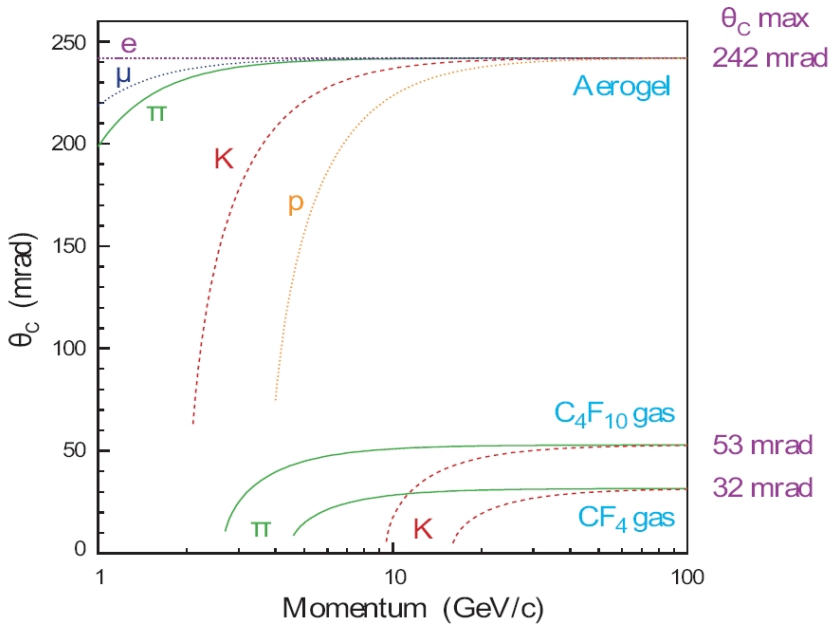

Figure 3.17: Cherenkov angle versus particle momentum for the RICH radiators [11].

3.4.1 RICH1

The RICH 1 subdetector is situated right after the VELO and before the TT, upstream of the LHCb dipole magnet. It covers the full LHCb acceptance from ± 25 mrad to ± 300 mrad on the horizontal plane and ± 250 mrad on the vertical plane, and is intended to provide particle identification for low momentum particles (from 1 to 60 GeV/c). It contains aerogel and fluorobutane (C_4F_{10}) gas radiators. As shown in Figure 3.18, it has a vertical optical layout. RICH1 was designed to respect the following constraints:

- The restriction on the amount of material within the RICH1 acceptance requires the use of lightweight spherical mirrors, with the rest of the components of the optical system situated outside of the acceptance. The total radiation length of RICH1, including the radiators, is 8% X_0.

- RICH1s low angle acceptance limit is given by the 25 mrad section of the beryllium beam pipe which passes through the detector.
- The HPDs need to be shielded from the field of the LHCb dipole magnet (up to 50 mT). Large iron boxes are used, since local shields of high permeability alloy were not sufficient.

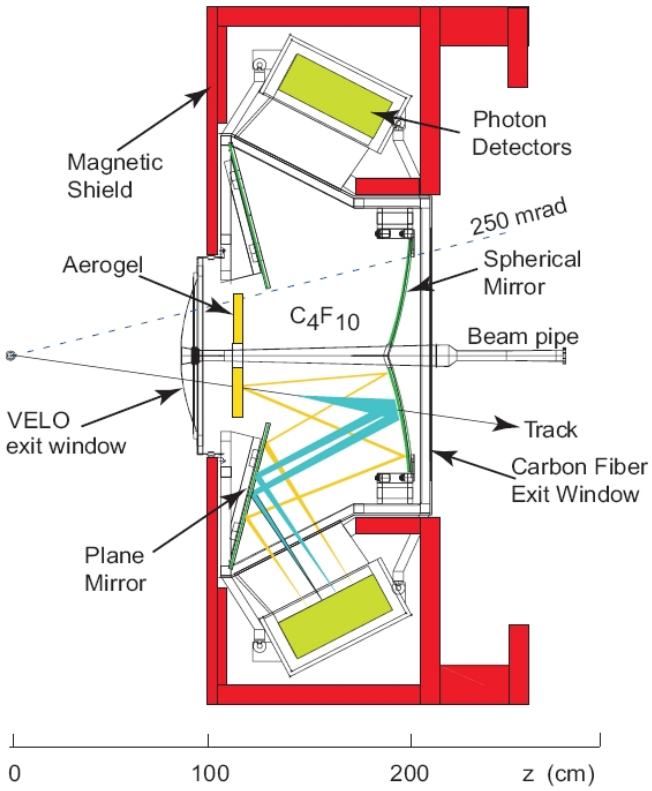

Figure 3.18: Side view schematic layout of the RICH1 detector [11].

3.4.2 RICH2

The RICH2 subdetector is intended to provide particle identification for high momentum particles (from 15 to 100 GeV/c). It is located between the last tracking station

and the first muon station, downstream of the LHCb dipole magnet. It has a limited angular acceptance of ± 15 mrad to ± 120 mrad on the horizontal plane and ± 100 mrad on the vertical plane, but covers the region where the high momentum particles are produced. It uses a CF_4 radiator (Figure 3.19), and the optical component and the readout are placed horizontally. Similar to the RICH1, which was restricted by the main LHCb detector setup, RICH2 had to be designed to respect the following constraints:

- The supporting structures and the photon detectors had to be placed outside the acceptance of the spectrometer, with the photon detectors located to the left and right of the beamline, where the iron shielding is accommodated. The total radiation length of RICH2, including the gas radiator, is about 0.15 X_0.
- The lower acceptance of the RICH2 detector (15 mrad) is limited by the necessary clearance of 45 mm around the beam pipe.
- Similar to RICH1, the HPDs are located in large iron boxes in order to shield them from the fringe of the LHCb dipole magnet (up to 50 mT).

3.5 Magnet

The LHCb dipole magnet is used to bend the trajectories of charged particles so that their momentum can be measured. It is a warm magnet with saddle-shaped coils in a window frame yoke, with sloping poles to match the detectors acceptance (± 250 mrad vertically and ± 300 mrad horizontally). The magnet is designed to provide a field integral of 4 T·m, balancing the restrictions of having a field level inside the RICHs of less than 2 mT and a field level as high as possible between the VELO and the TT (see Table 3.1). Figure 3.20 shows the layout of the LHCb dipole magnet. The field provided by the LHCb dipole magnet has its principal component in the y axis (in general LHCb coordinates), so it generates a bending plane in the x-z plane.

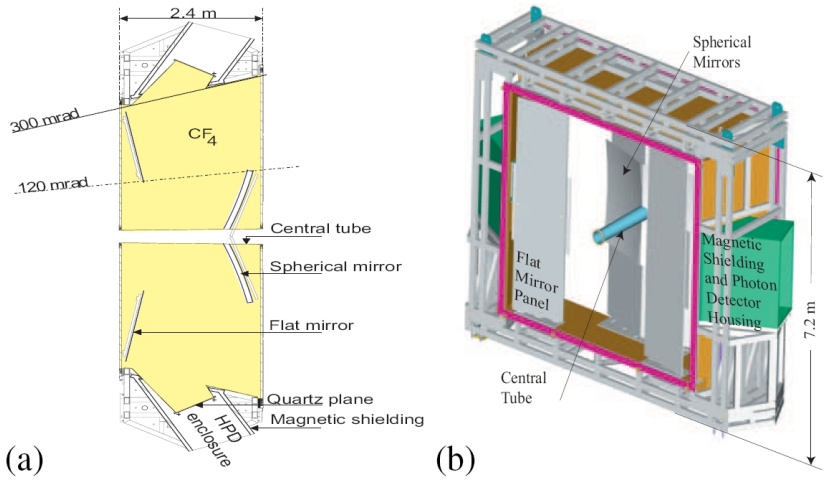

Figure 3.19: a) Top view schematic layout of the RICH2 detector, b) Schematic layout of the RICH2 detector [11].

Table 3.1: Measured main parameters of the LHCb dipole magnet

Non-uniformity of $\|x\|$	± 1 in xy planes of 1 m^2 from z=3 to z=8 m
$\int \mathrm{B}dl$ upstream TT region (0-2.5m)	0.1159 T·m
$\int \mathrm{B}dl$ downstream TT region (2.5-7.95m)	3.615 T·m
Max field at HPD's of RICH1	20×10^{-4} T
Max field at HPD's of RICH2	9×10^{-4} T
Electric power dissipation	4.2 MW
Inductance L	1.3 H
Nominal / maximum current in conductor	5.85 kA/6.6 kA
Overall dimensions H × V × L	11 m × 8 m × 5 m
Total weight	1600 tons

3.6 Calorimeter system

The LHCb calorimeter system performs the identification of electrons, photons, and hadrons, as well as the measurement of their energies and positions. It also selects high transverse energy hadron, electron, and photon candidates for the first trigger level (L0). High accuracy reconstructions of π^0 and prompt photons are essential for the study of B-meson decays, i.e., a good calorimeter is important for the

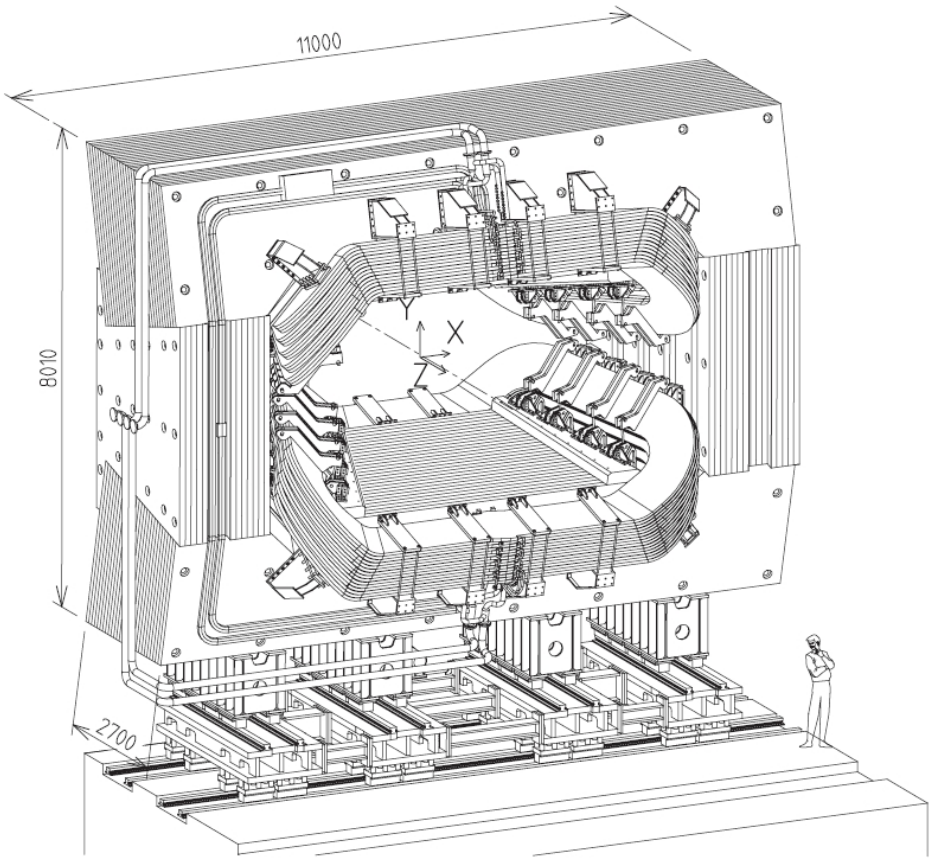

Figure 3.20: Schematic layout of the LHCb dipole magnet [11].

LHCb physics program. The calorimeter system is designed to obtain a high performance in terms of resolution and shower separation. The LHCb calorimeter system has a classical structure, made up of an electromagnetic calorimeter (ECAL) followed by a hadron calorimeter (HCAL). It consists of several layers: the Scintillating Pad Detector (SPD), the Pre-Shower Detector (PS), the shashlik-type Electromagnetic Calorimeter (ECAL), and the scintillating tile iron plate Hadron Calorimeter (HCAL).

3.6.1 SPD/PS

The SPD determines whether particles hitting the calorimeter system are charged or neutral, while the PS indicates the electromagnetic character of the particle (i.e., whether it is an electron, if charged, or a photon, if neutral). They are used at the trigger level in association with the ECAL to indicate the presence of electrons, photons, and neutral pions.

The SPD and PS consist of scintillating pads with a thickness of 15 mm, interspersed with a 2.5 X0 lead converter. Light is collected using wavelength-shifting (WLS) fibers (Figure 3.21). Almost four turns of fiber are inserted and glued in the round groove of each square pad, and both ends of the WLS fiber are used to transmit the light to multi-anode photomultipliers (MAPMTs) located at the periphery of the detector. The SPD and PS both contain about 6000 pads, each of which is equipped with an embedded individual light emitting diode (LED) for monitoring detector stability.

3.6.2 ECAL

The LHCb electromagnetic calorimeter uses a shashlik calorimeter, which consists of a sampling scintillator/lead structure readout by plastic WLS fibers. Its design requirement is to give an energy resolution of σ_E/E = 10 % / $\sqrt{E} \oplus$ 1.5% (E in GeV) [33]. This results in a π^0 mass resolution of 8 MeV/c^2. The calorimeter is placed 12.5 m from the interaction point. Its outer dimensions projectively match

Figure 3.21: Loops of wavelength-shifting (WLS) fibers [13].

those of the tracking system, $\theta_x < 300$ mrad and $\theta_y < 250$ mrad; the inner acceptance is limited by $\theta_{x,y} < 25$ mrad around the beam pipe due to the substantial radiation dose level. It is subdivided into inner, middle, and outer sections (see Table 3.2) to account for the fact that the hit density is a steep function of the distance from the beam pipe. The ECAL modules (Figure 3.22) are built from alternating layers of 2 mm thick lead, 120 μm thick white reflecting paper, and 4 mm thick scintillator tiles. In depth, the 66 Pb and scintillator layers form a 42 cm stack corresponding to 25 X_0. The Moliere radius of the stack is 3.5 cm.

Table 3.2: Main parameters of the LHCb electromagnetic calorimeter

	Inner section	Middle section	Outer section
Inner dimension, x ×y, cm^2	65 × 65	194 × 145	388 × 242
Outer dimension, x ×y, cm^2	194 × 145	399 × 242	776 × 630
Cell size cm^2	4.04 × 4.04	6.06 × 6.06	12.12 × 12.12
# of modules	176	448	2688
# of channels	1536	1792	2688
# of cells per module	9	4	1
# of fibers per module	144	144	64
Fibre density, cm^{-2}	0.98	0.98	0.44

Figure 3.22: Outer, middle, and inner type ECAL modules [11].

3.6.3 HCAL

The LHCb hadron calorimeter is placed right behind the electromagnetic calorimeter. It consists of iron plates interspersed with scintillating tiles. The orientation of the tiles is such that they run parallel to the beam axis. In the lateral direction, the tiles are separated by 1 cm of iron, and in the longitudinal direction the length of tiles and iron spacers corresponds to the hadron interaction length λ_I in steel. The light inside the tiles is collected by WLS fibers running along the detector towards the back side, where the photomultiplier tubes (PMTs) are located (Figure 3.23). The total weight of the HCAL is about 500 tons.

The requirements for the HCAL energy resolution make it possible to obtain a ratio of active to passive material as low as 0.18. The total length of the HCAL is 5.6 λ_I, due to the limited space available. The upstream ECAL adds another 1.2 λ_I. Energy resolution was determined using the CERN SPS test beam; the fit to the data at several energies is given by σ_E/E = (69±5) % / $\sqrt{E} \oplus$ (9±2)% (E in GeV).

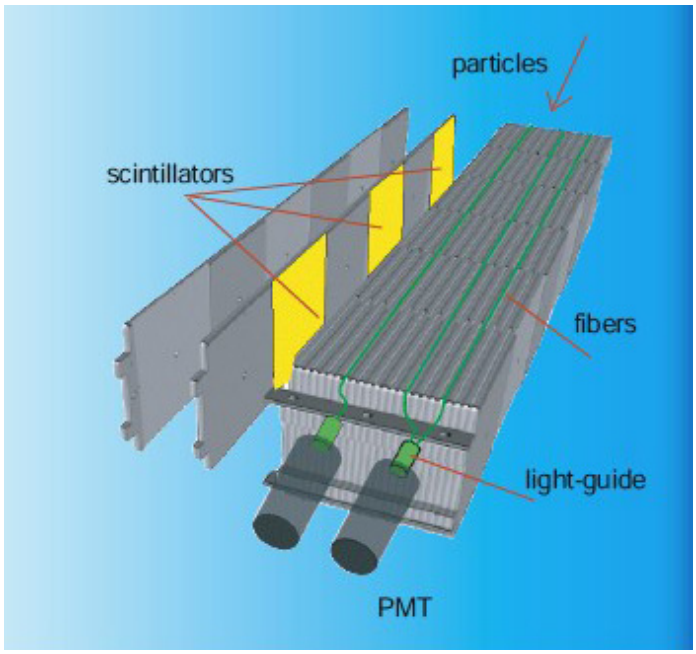

Figure 3.23: Schematic view of an HCAL Module [11].

3.7 Muon system

The muon system provides fast information to the high-p_T muon trigger at the earliest level (L0), as well as muon identification for the high-level-trigger and offline analysis. Located at the far end of the detector, it is composed of five stations (M1-M5; see Figure 3.24) covering an acceptance of ±300 mrad (horizontally) and ±250 mrad (vertically). Rectangular stations are placed along the beam axis, and their combined total area is 435 m^2. Each station contains multi-wire proportional chambers filled with gas mixtures made up of $Ar/CO_2/CF_4$, with 40 % Ar and variable concentrations of CO_2/CF_4. The passing muons react with this mixture, and wire electrodes detect the signal. In total, the muon system contains 1,380 multi-wire proportional chambers.

The layout of the muon stations is shown in Figure 3.24. Station M1 is placed in front of the calorimeter system and is used to improve p_T measurement in the trigger. Stations M2-M5 are situated after the calorimeter system, and are interspersed with 80 cm thick iron absorbers in order to select penetrating muons. The total absorber thickness, including the calorimeter system, is around 20 interaction lengths; therefore, the minimum momentum of a muon required to cross the muon system is approximately 6 GeV/c.

3.8 Trigger

The designed operating luminosity of the LHCb experiment is 2×10^{32} $cm^{-2}s^{-1}$, motivated by the requirements for low occupancy and tolerable radiation damage to the detector and electronics. The nominal LHC bunch crossing frequency is 40 MHz. At this crossing rate and nominal luminosity, the interaction rate visible to the LHCb spectrometer is 10 MHz. Of this 10 MHz, only a few events contain decays that are interesting for physics analysis. The role of the trigger is to select such events, limiting the output to 2 kHz, at which rate the events are recorded to storage. This is achieved using two trigger levels (Figure 3.25): Level-0 (L0) and the High Level

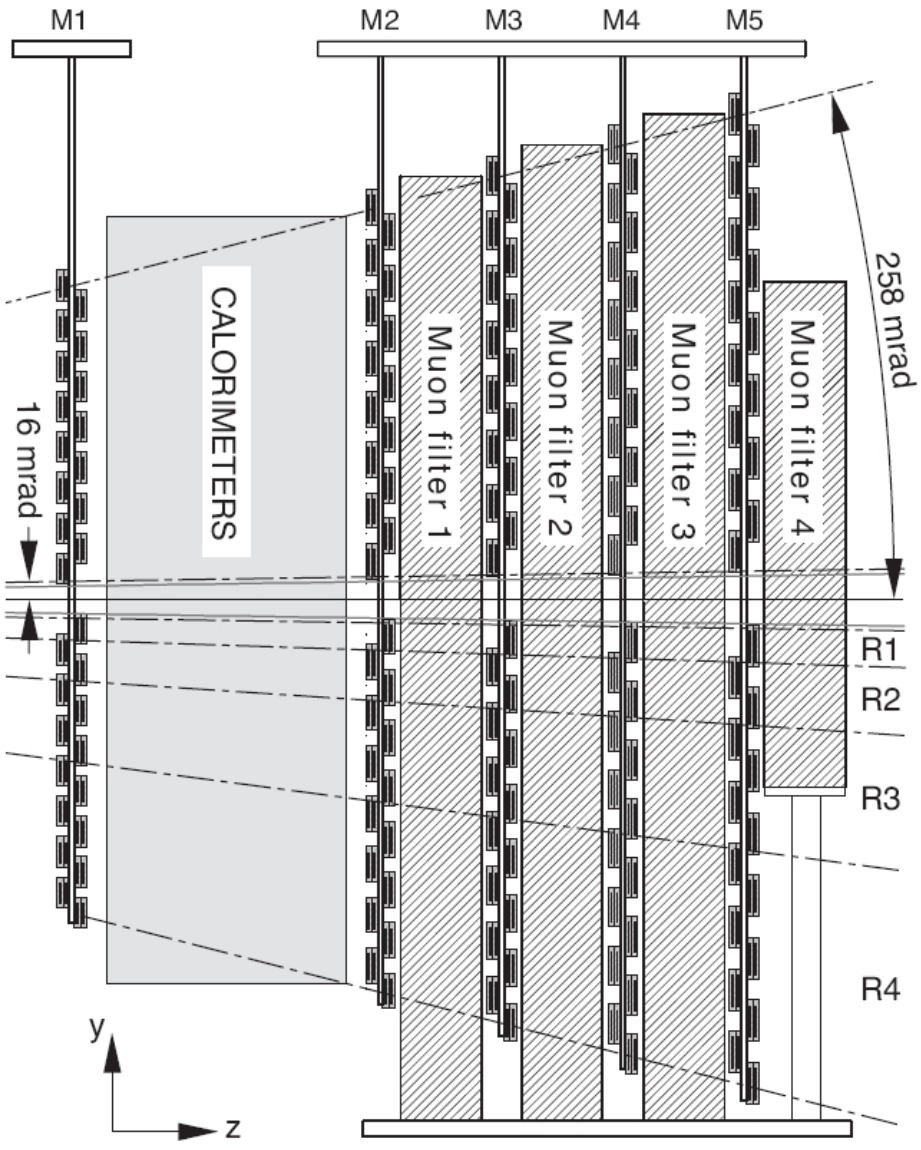

Figure 3.24: Schematic side view of the muon system [11].

Trigger (HLT).

3.8.1 L0 trigger

The role of the L0 trigger is to reduce the LHC beam crossing rate from 40 MHz to 1 MHz, with which the entire detector can be read out. Its event selection criteria are based on the main LHCb's purpose, which is to reconstruct B mesons, i.e., it looks for particles with large transverse momentum (p_T) and energy (E_T). Decays of B mesons often produce such particles.

The L0 trigger attempts to quickly reconstruct:

- The highest E_T hadron (h), electron (e), and photon (γ) clusters in the calorimeters.
- The two highest p_T muons (μ) in the muon chambers.

Then, together with an estimate of the number of primary pp interactions, performed by the pile-up system in the VELO, and another estimate of the total number of tracks, performed by the SPD (based on the number of hits), it makes a quick decision to accept or reject an event which will be processed later by the HLT.

3.8.2 HLT trigger

The role of the HLT trigger is to reduce the rate from 1 MHz (i.e., the output of the L0 trigger) to 2 kHz. For this, it makes use of the full event data. The HLT trigger is subdivided into two stages, HLT1 and HLT2. In the HLT1 stage it reconstructs μ, e, and h candidates found by the L0 trigger using the VELO and T stations, and in the case of γ and π^0 candidates it confirms the absence of a charged particle associated with them. After this, it divides the candidates into independent alleys (Figure 3.26).

In the HLT2 stage, HLT1 candidates are selected using very loose cuts from their momentum and impact parameter, and are afterwards used to form composite particles such as $K^* \to K^+\pi^-$, $\phi \to K^+K^-$, $D^0 \to$ hh, $D_s \to K^+K^-\pi^-$, and $J/\psi \to \mu\mu$. This is

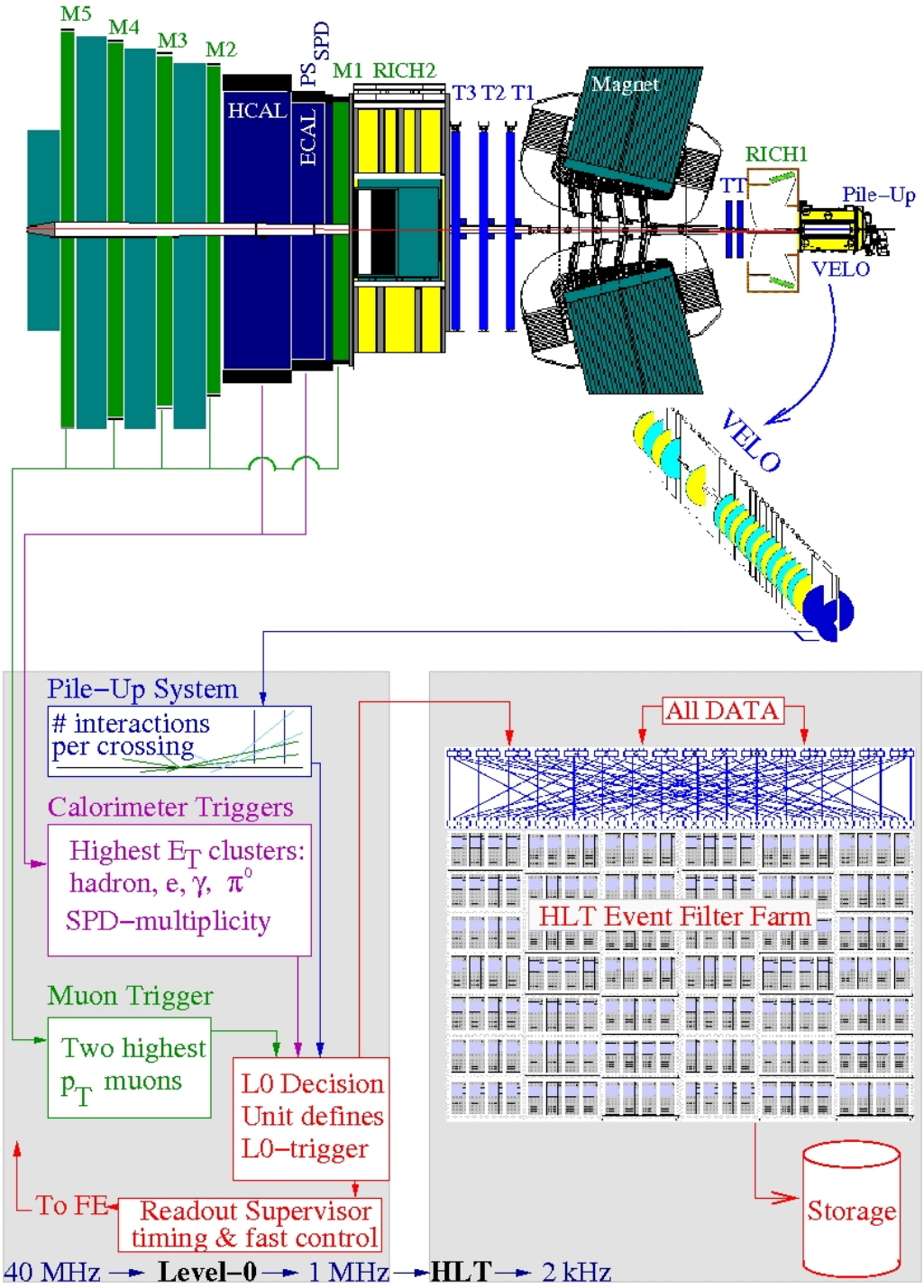

Figure 3.25: Schematic representation of the trigger system

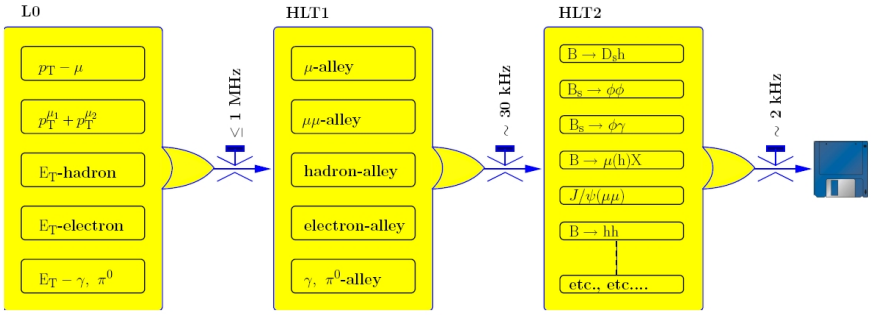

Figure 3.26: Flow diagram of the trigger sequence [11].

done using very elementary information, since the HLT tracks differ from the off-line track reconstruction in not having been fitted with a Kalman filter. After this, the HLT2 combines such particles to form B candidates by performing cuts on the invariant mass and/or pointing of the B momentum towards the primary vertex. After HLT2, the output should already be less than 2 kHz.

3.8.3 VELO Microbias Trigger

The trigger chosen for data acquisition in early May 2010 was a VELO microbias trigger (Hlt1MBMicroBiasRZVeloDecision), in order to prepare a reference data set for general physics purposes. The L0 trigger was in pass-through mode, while at the HLT at least one track, reconstructed with VELO information, should be found to accept the event.

Chapter 4

Analysis Preface

4.1 DATA and MC Sample

This analysis was run over the dataset collected by the LHCb experiment in May 2010, which recorded pp collisions at a center-of-mass energy of $\sqrt{s} = 7$ TeV. It will be referred to throughout the document as DATA2010. Only runs of adequate quality, with no prescaling and a 100% trigger efficiency, are included. Data recorded for the two field-polarities of the spectrometer magnet, referred to in the following as "Magnet Up" and "Magnet Down", are analyzed separately. The luminosity was determined using the central LHCb luminosity project [34], based on the calibration constants given by the conditions database tag "head-20100715". The data sample was placed under the Microbias line in the Reco05Stripping09 production. Datasets are summarized in Table 4.1 :

Table 4.1: Summary of data samples used for the analysis (DATA2010)

Run number	Magnet Polarity	N Events (x10^6)	Integrated Luminosity (nb^{-1})
71806-71816	Down	36.77	0.60±0.06
71474-71530	Up	73.49	1.2 ± 0.12

MC studies for this measurement were performed on 18 million simulated minimum bias events (10 million for Magnet Down and 8 million for Magnet Up) of type MC2010 (ν=1, Sim04Reco03).

4.2 Detector Performance

The event selection performed in this analysis is purely geometrical, based on initial reconstruction parameters as described in Chapter 5. Therefore, the selection efficiency is highly correlated with the resolution of such parameters. The following subsections describe reconstruction information relevant to understanding both the selection efficiency and systematic uncertainties (Chapter 7).

4.2.1 Primary Vertex and IP Resolutions

The primary vertex (PV) resolution is determined in the following way:

- For each event, the VELO track sample is divided into two subsamples.
- The PV position is estimated with each subsample.
- The distribution of the differences between the two PVs then has an rms-width that is $\sqrt{2}$ times the actual resolution.

Figures 4.1(a) and 4.1(b) show the X and Y resolution as a function of the number of tracks used in the estimate. Although the data and simulation are in qualitative agreement, statistically significant differences are observed and must be considered as a source of systematic uncertainty for analyses relying on PV information.

The Impact Parameter (IP) is defined as the distance of closest approach of a track to the PV. It is essential to discriminate between prompt and non-prompt particles. Figures 4.2(a) and 4.2(b) show the X and Y resolution as a function of the number of tracks used in the estimation. In this case the data and simulation clearly have different IP resolutions, which has to be taken into account for systematic studies, because it affects selection efficiencies.

4.2.2 Tracking Efficiency

The tracking efficiency is defined as the probability of a particle emitted in the detector's acceptance having a corresponding reconstructed track [14]. This involves the

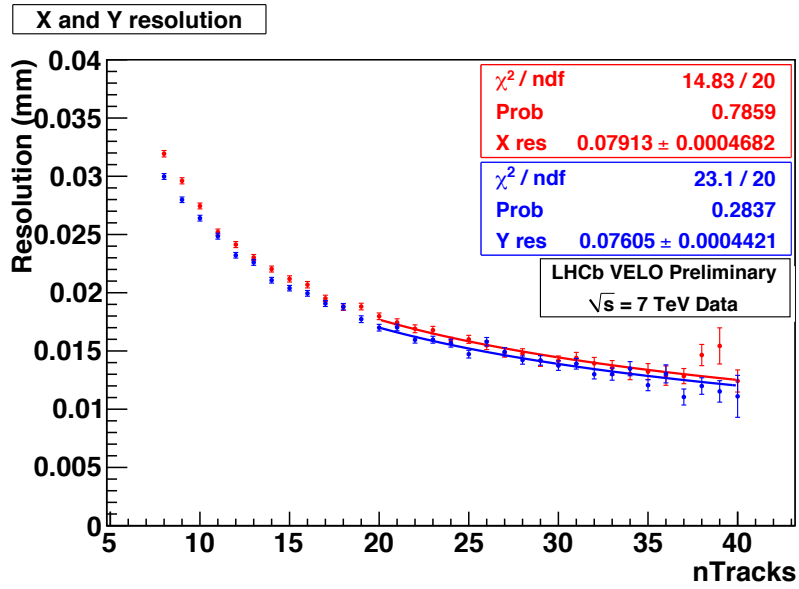

(a) Data

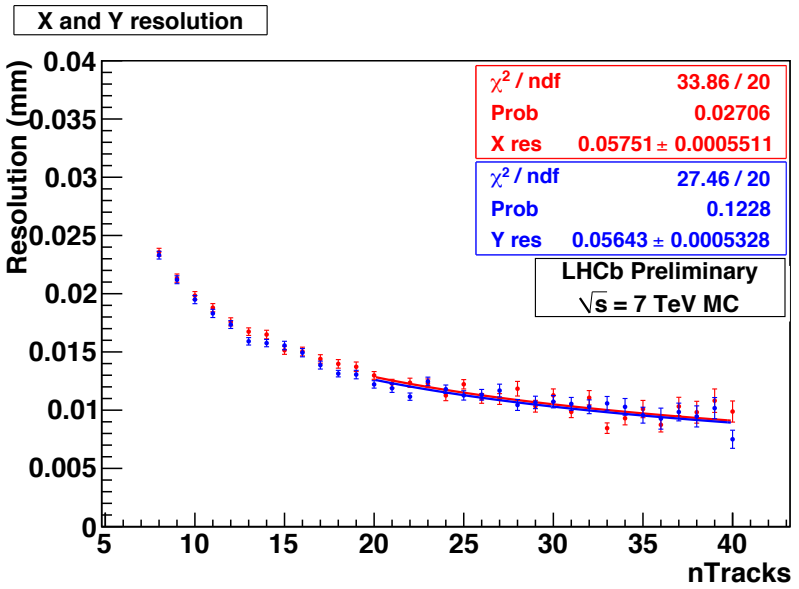

(b) MC

Figure 4.1: Primary Vertex (PV) X and Y resolution plotted as a function of the number of tracks used for its calculation, for (a) early 2010 data and (b) MC [14].

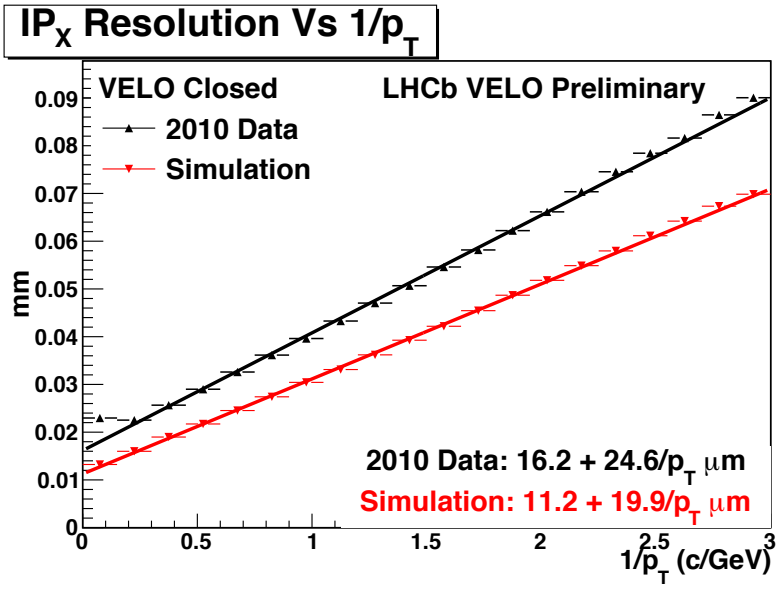

(a) Data

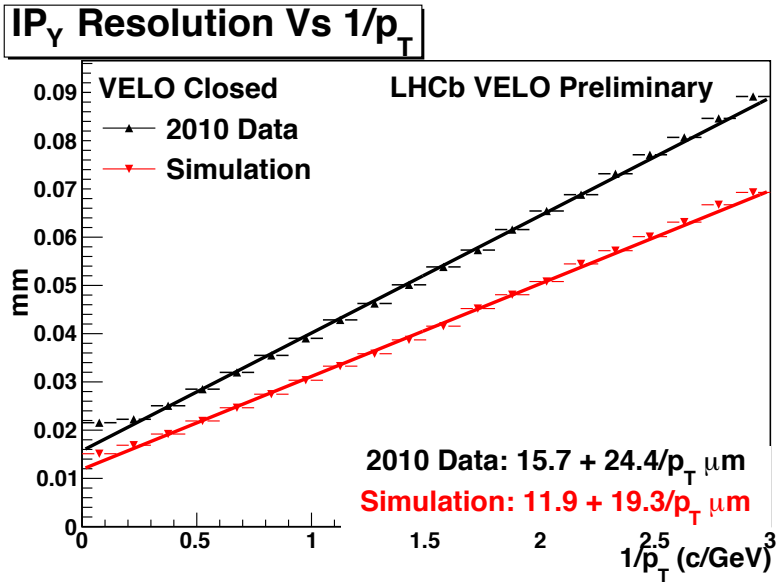

(b) MC

Figure 4.2: IP resolution for X and Y coordinates plotted as a function of $1/p_T$ for (a) early 2010 data [15] and (b) MC.

particle having remained within acceptance all the way up to the very last tracking station. Included in this definition are the hit efficiency and the track reconstruction efficiency, excluding any acceptance related efficiency. To obtain the best possible momentum estimate, long tracks (tracks that traverse all of the tracking subdetectors) are used. One of the two methods used to estimate tracking efficiency uses K_s^0 decays into a $\pi^+\pi^-$ final state. With this method, after the selection of K_s^0 candidates is complete, the sample is split into two types of candidates: candidates with two oppositely charged long tracks, and candidates with one long track and one VELO track with an associated calorimeter cluster (to ensure that the pion remains in acceptance). Fig 4.3 shows the signal yields obtained for both types of candidates. The difference comes from the probability of having a reconstructed track segment in the IT, or OT for the VELO track. Figure 4.4 shows the tracking efficiency as a function of transverse momentum p_T of the mother particle; here we can observe good agreement between the data and simulation.

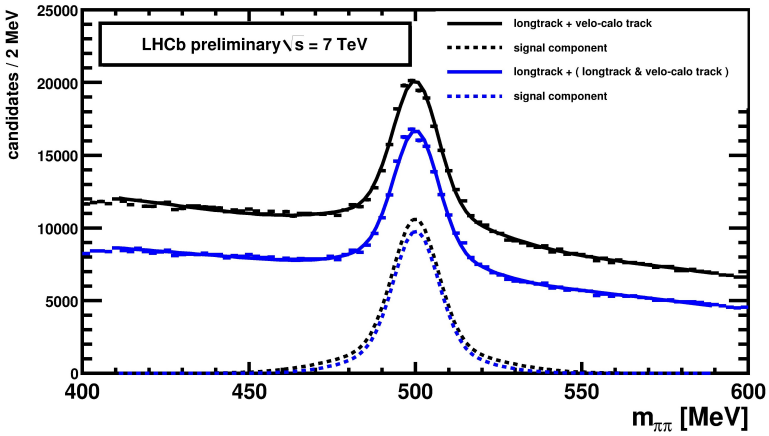

Figure 4.3: K_s^0 signal for two types of candidates: two long tracks (solid black histogram), and one long track and one VELO track with an associated calorimeter cluster (solid blue histogram). Dashed lines represent the yields after background subtraction for each selection [14].

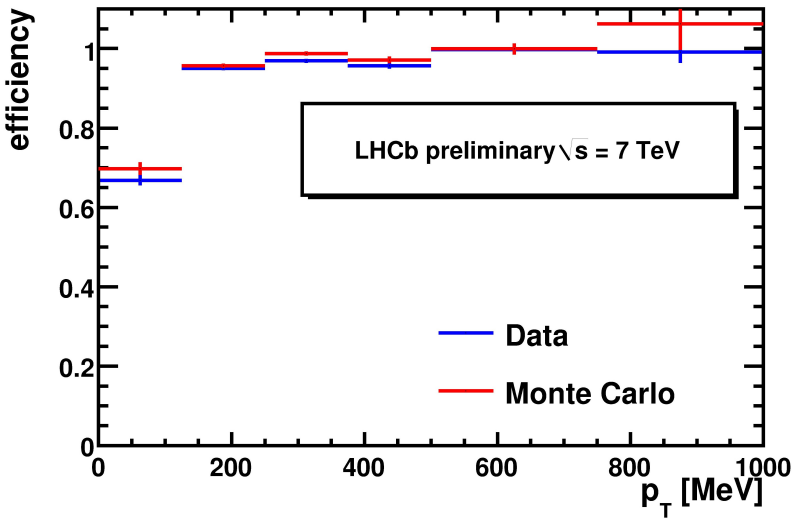

Figure 4.4: Tracking efficiency as a function of transverse momentum p_T for K_s^0 reconstruction [14].

4.2.3 RICH Particle Identification

After particles traverse the RICH's radiator material, the emitted Cherenkov Radiation is projected by a system of mirrors onto the photon detectors. There, the distribution of the Cherenkov photons is analyzed and compared to the expected ring profiles corresponding to the kaon, pion, and proton hypotheses (Figure 4.5). The discrimination between kaons, pions, and protons is done numerically by means of a delta-log-likelihood variable, defined as

$$\mathrm{DLL}(a-b) \equiv \ln L_a - \ln L_b = \ln \frac{L_a}{L_b} \tag{4.1}$$

where L_a is the likelihood of the hypothesis for particle a and L_b is the likelihood of the hypothesis for particle b. Therefore, when DLL(a-b) ≥ 0, the Cherenkov photon distribution is more likely to have been created by a particle of type a rather than type b. RICH performance studies have been performed on the data taken in the first half of 2010 [16]. Figure 4.6 shows the kaon PID efficiency versus momentum using the cut DLL(K-π) ≥ 5. The upper curve (red symbols) shows the efficiency

for real kaons and the lower one (black symbols) for real pions. Since the observed misidentification efficiency for pions is very low, we can obtain very pure K samples for a wide momentum range. Similarly, Figure 4.6 shows the proton PID efficiency versus momentum using the cut DLL(p-π) ≥ 5 for protons and pions.

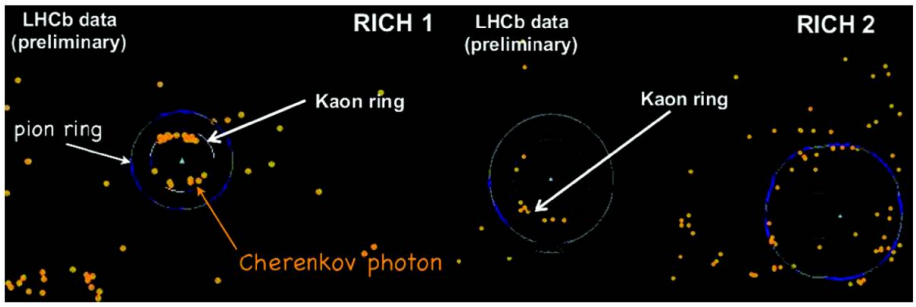

Figure 4.5: Cherenkov photon profiles measured in RICH1 and RICH2. Blue circles indicate the kaon and pion hypotheses [16].

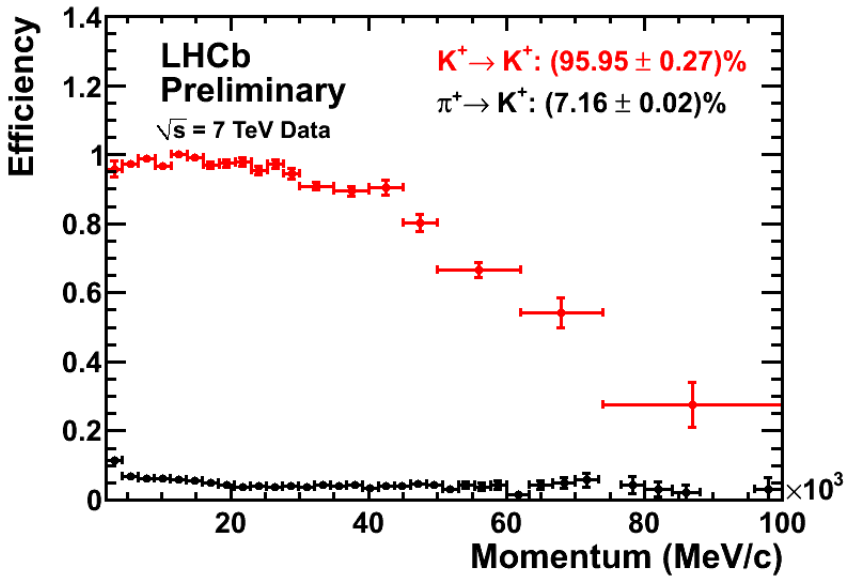

Figure 4.6: Kaon PID efficiency for kaons (black squares) and pions (red squares) [16].

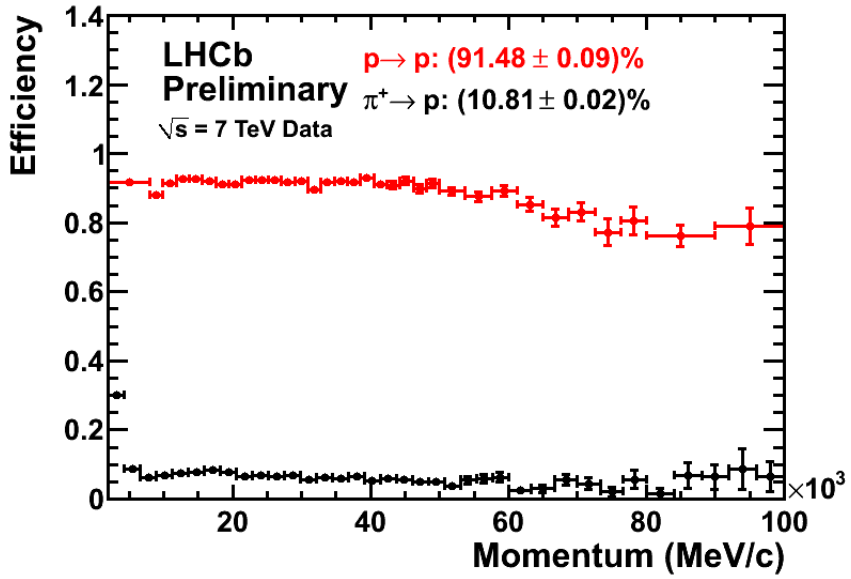

Figure 4.7: Proton PID efficiency for protons (black squares) and pions (red squares) [16].

4.3 General Strategy

The production of three strange particles (K^0_s, Λ, and $\overline{\Lambda}$ as seen in Table 2.4) is analyzed. The term V^0 will be used to refer to the three particles when it applies generally; for particular reference to each resonance the specific name will be given. The analysis is performed in bins of V^0 phase space. The kinematic variables used are the V^0 transverse momentum p_T, defined as $\sqrt{p_x^2 + p_y^2}$, and the rapidity $y = \ln((\mathrm{E}+p_z)/(\mathrm{E}\text{-}p_z))$, where (E,$p_x$,$p_y$,$p_z$) is the V^0 four-momentum defined in the pp center-of-mass system.

The selected range for the kinematic variables is $0 \leq p_T \leq 2.4$ GeV/c, $2.5 \leq$ y ≤ 4.5 for K^0_s, and $0.2 \leq p_T \leq 2.4$ GeV/c, $2.5 \leq y \leq 4.0$ for Λ and $\overline{\Lambda}$. This binning was chosen to guarantee sufficient data statistics in each bin. For consistency, the same selection (Chapter 5) is applied to all V^0-resonances. All V^0 candidates are reconstructed in their main decay modes, namely, $K^0_s \to \pi^+ \pi^-$, $\Lambda \to$ p π^-, and $\overline{\Lambda} \to \overline{p}\ \pi^+$ (as seen in Table 2.4).

Cross-sections are measured using only information from each bin (i,j) in terms of p_T and rapidity as

$$\sigma_{i,j} = \frac{N_{i,j}^{Obs}}{\epsilon_{i,j} L_{int}}, \tag{4.2}$$

where:

- $N_{i,j}^{Obs}$: the number of reconstructed and selected V^0-decays with p_T and y in bin (i,j) from DATA2010.
- $\epsilon_{i,j}$: the detector efficiency for reconstruction and selection, determined for MC2010.
- L_{int} : the integrated luminosity.

Finally, to cancel out any possible effects on the reconstruction efficiency due to the detector's geometry (Subsection 7.4), the observed cross-sections from both magnet polarities are combined via an unweighted average as

$$\sigma_{i,j} = \frac{1}{2}\sigma_{i,j}^{Down} + \frac{1}{2}\sigma_{i,j}^{Up}. \tag{4.3}$$

4.3.1 Yields

The number of reconstructed and selected V^0-decays ($N_{i,j}^{Obs}$) is obtained from the signal yields in DATA2010 using the event selection described in Chapter 5. Yields are measured from the invariant mass distributions of V^0-decays for each p_T and y bin. For this purpose, each component track of the candidate is given the mass of the corresponding positive and negative daughter particles for each decay ($\pi^+\pi^-$ for K_s^0, $p\pi^-$ for Λ, and $\pi^+\bar{p}$, proton for $\overline{\Lambda}$). This is done to calculate the four-momentum of each daughter particle and combine to build that of the mother particle, from which its invariant mass is obtained. Figures 4.8 and 4.9 show the distributions for K_s^0-decays in DATA2010 and MC2010, respectively, where a prominent peak is positioned at the known value for this resonance (498 MeV/c^2) [PDG reference], and practically no background is present. It can be seen that the peaks are not fully symmetric, due

to radiative tails and the detector's momentum-dependent resolution. To prevent any possible bias that might arise from fitting a signal shape, yield extraction performed by background subtracted event counting is chosen for this analysis. The same holds for Λ and $\overline{\Lambda}$-decays (Figures 4.10, 4.11), which also present a clear mass peak in the PDG value (1115.7 MeV/c^2) which is not symmetrical. In this case we see a fairly linear background with a positive slope.

Having the invariant mass distributions ready, the yield extraction procedure is as follows: directly count the entries in the signal region and subtract the background estimated from the sidebands, based on the cubic background assumption [35] as

$$N_{bckg} = \frac{3(N_b + N_c) - (N_a + N_d)}{2}, \tag{4.4}$$

where N_{bckg} is the estimated background, and N_a, N_b, N_c, and N_d are the number of entries in the sideband regions (of equal size), specified in Table 4.2 and shown in Figures 4.8, 4.9, 4.10, and 4.11. The regions for each of the different V^0-decays were assigned to guarantee that the majority of the signal was accounted for.

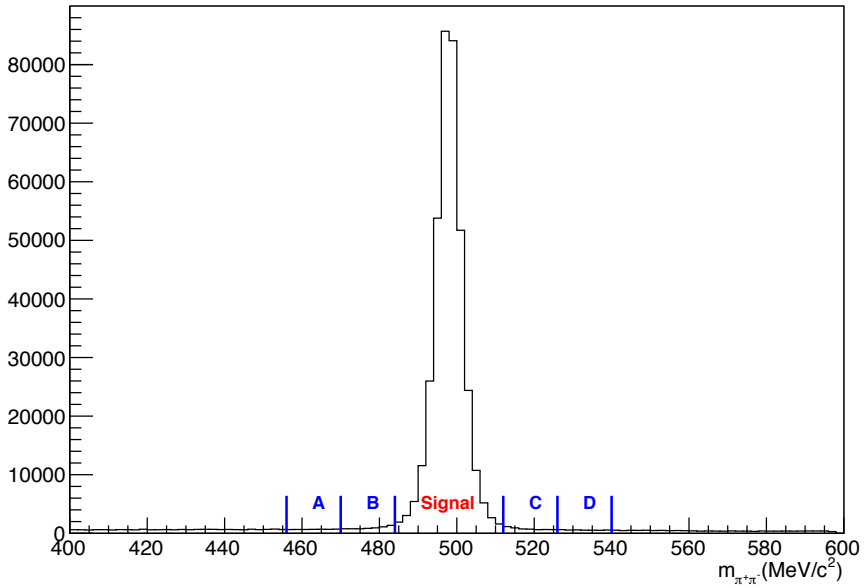

Figure 4.8: Invariant mass distribution for K^0_s candidates on DATA2010.

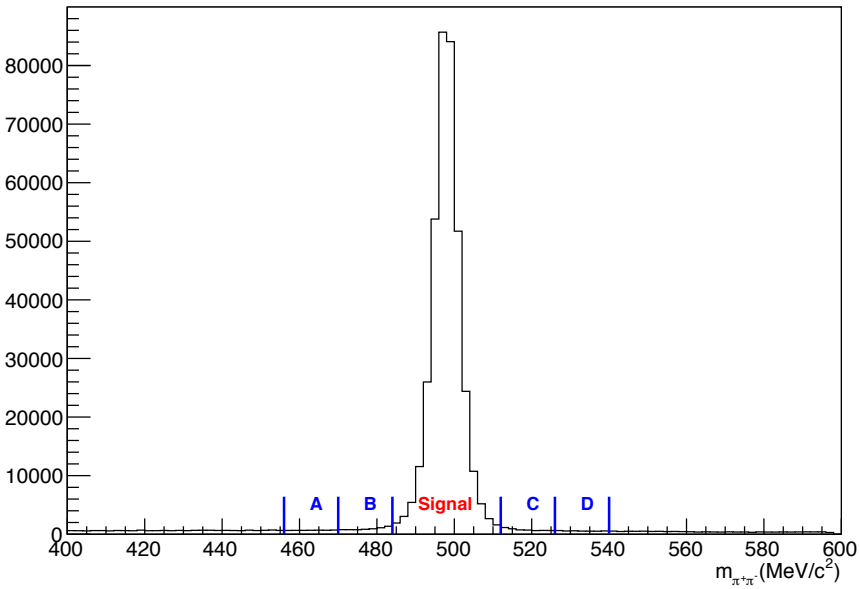

Figure 4.9: Invariant mass distribution for K^0_s candidates from MC2010.

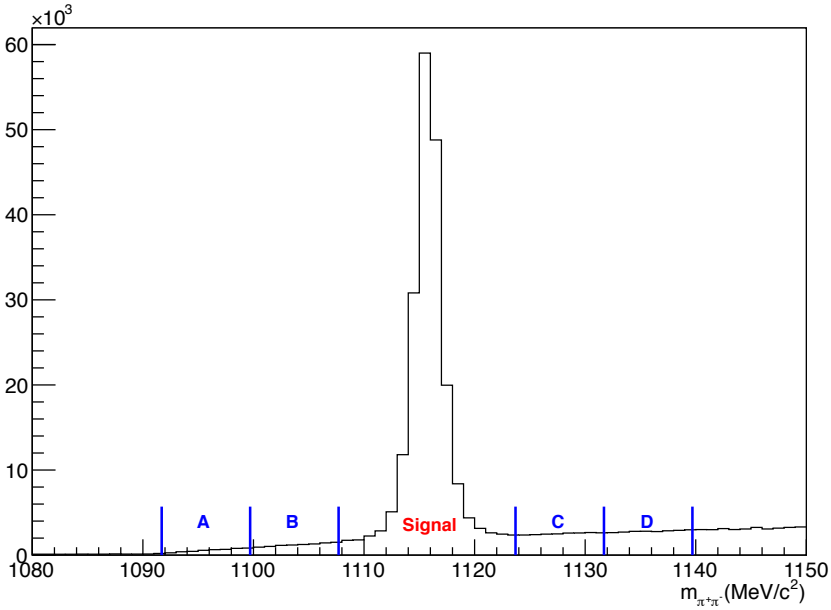

Figure 4.10: Invariant mass distribution for Λ and $\overline{\Lambda}$ candidates from DATA2010.

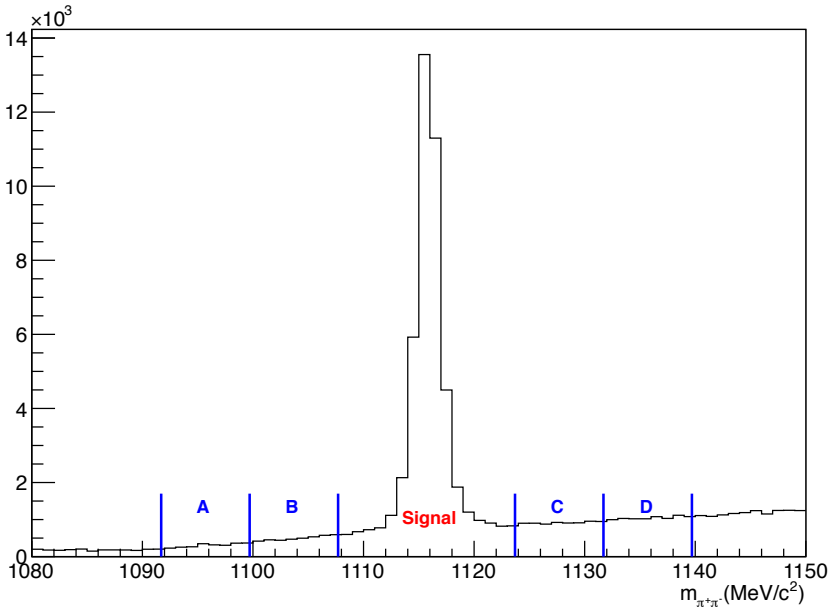

Figure 4.11: Invariant mass distribution for Λ and $\overline{\Lambda}$ candidates from MC2010.

Table 4.2: Signal and sideband regions

Particle	Signal	A	B	C	D
K^0_s	[484,512]	[456,470]	[470,484]	[512,526]	[526,540]
Λ,$\overline{\Lambda}$	[1107.7,1123.7]	[1091.7,1099.7]	[1099.7,1107.7]	[1123.7,1131.7]	[1131.7,1139.7]

4.3.2 Efficiencies

Efficiencies for reconstructing and selecting prompt V^0-decays are measured for MC2010 for each p_T and y bin by the following:

$$\epsilon_{i,j} = \frac{N^{Obs}_{i,j}(MC)}{N^{Gen}_{i,j}(MC)}, \tag{4.5}$$

where:

- $N^{Obs}_{i,j}(MC)$: the number of reconstructed and selected V^0-decays with p_T and y in bin (i,j), for MC2010, measured as in DATA2010 via background subtracted yields.

- $N_{i,j}^{Gen}(MC)$: the number of generated prompt V^0-decays for MC2010. For this purpose, only V^0's which do not include p-p interaction particles with a mean lifetime (τ) greater than 10^{-10}s (Section 7.2) in their decay chain are taken into account.

To understand the enclosed effects in $\epsilon_{i,j}$, the following partitioning is performed:

$$\epsilon_{i,j} = \epsilon(trig|sel)_{i,j}\epsilon(sel|rec)_{i,j}\epsilon(rec)_{i,j} \tag{4.6}$$

Here $\epsilon(rec)_{i,j}$ is taken from MC and is well known to reproduce data reconstruction efficiency. With 3% uncertainty on the single track reconstruction efficiency [36], a systematic uncertainty of 6% is assigned to the V^0reconstruction efficiency estimated from the simulation.

The quantity $\epsilon(sel|rec)_{i,j}$ is the selection efficiency, namely how many of the reconstructed V^0-decays survive the selection criteria. This is analyzed thoroughly in Section 5.4. Different kinematics between DATA and MC cause discrepancies; a correction factor is calculated from the observed differences in $\epsilon(sel|rec)_{i,j}$ between DATA2010 and MC2010, and is applied to the cross-section measurements to correct for this error.

Finally, $\epsilon(trig|sel)_{i,j}$ is the trigger efficiency. The trigger used for this analysis, MicroBiasTriggered, does not have any further requirements at the L0 level as compared to a track reconstructed with the VELO and found by the HLT. Therefore, this trigger configuration is intrinsically 100 % efficient for reconstructed V^0-decays after selection (Chapter 5), because they are formed from two long tracks. Because no prescaling was applied for this trigger on the selected data samples, we can proceed to take $\epsilon(trig/sel)_{i,j} = 1$.

Chapter 5

Event Selection

5.1 General requirements

The requirements for an event to be processed by the algorithm are:

- VELO microbias trigger on HLT1 (Subsection 3.8.3).
- Two or more long tracks (tracks which traverse all of the tracking subdetectors, as shown in Figure 5.1).
- At least one reconstructed primary vertex.
- Geometrical variable $\omega \geq 5.5$ (see Section 5.2).

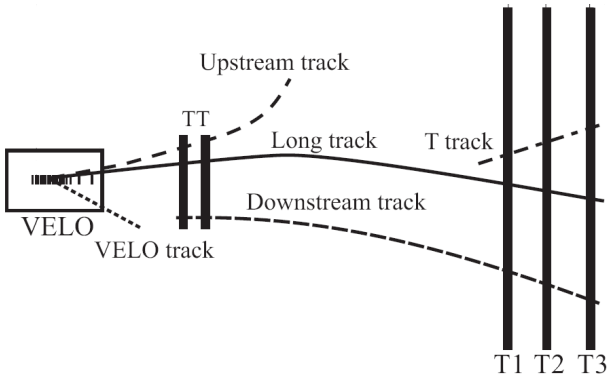

Figure 5.1: Schematic illustration of the various track types, classified by the tracking subdetectors traversed.

5.2 Geometrical candidate selection (ω)

In an ideal $V^0 \rightarrow h^+h^-$ decay we would obtain planar geometry, meaning that the momentum of the V^0 and its daughters would all be on the same plane. However, due to detector resolution, the measured configuration is, in general, not planar. If we take the vector resulting from the cross product of the momentum of both daughter particles, $\hat{\mathbf{n}} = \tilde{\mathbf{p}}_\mathbf{1} \times \tilde{\mathbf{p}}_\mathbf{2}$, then the geometry splits into two planes orthogonal to $\hat{\mathbf{n}}$ (Figure 5.2). Standard notation is used, where $\tilde{\mathbf{r}}$ stands for a 3-vector and $\hat{\mathbf{r}}$ for a unit 3-vector.

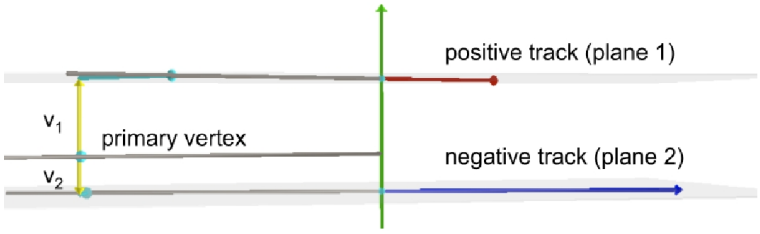

Figure 5.2: Schematic view of the planes formed by the V^0 daughter particles' tracks. The vector $\hat{n}$ is shown at the beginning of the positive and negative daughters as a green arrow, and its projection into the primary vertex as a yellow arrow, where v_1 and v_2 are measured.

We then have observables perpendicular to $\hat{\mathbf{n}}$ (Figure 5.3) such as:

- $\mathbf{d_1}, \mathbf{d_2}$: 2-dimensional signed impact parameters of the positive and negative daughters, respectively, at the primary vertex measured perpendicular to $\hat{\mathbf{n}}$. The sign comes from the orientation of the impact parameter vector with respect to the momentum of the V^0, namely, the sign of the scalar product $(\tilde{\mathbf{d}}_\mathbf{i} \cdot (\tilde{\mathbf{p}}_\mathbf{1} + \tilde{\mathbf{p}}_\mathbf{2}))$.

- **d:** 2-dimensional impact parameter of the V^0 candidate at the primary vertex calculated perpendicular to $\hat{\mathbf{n}}$.

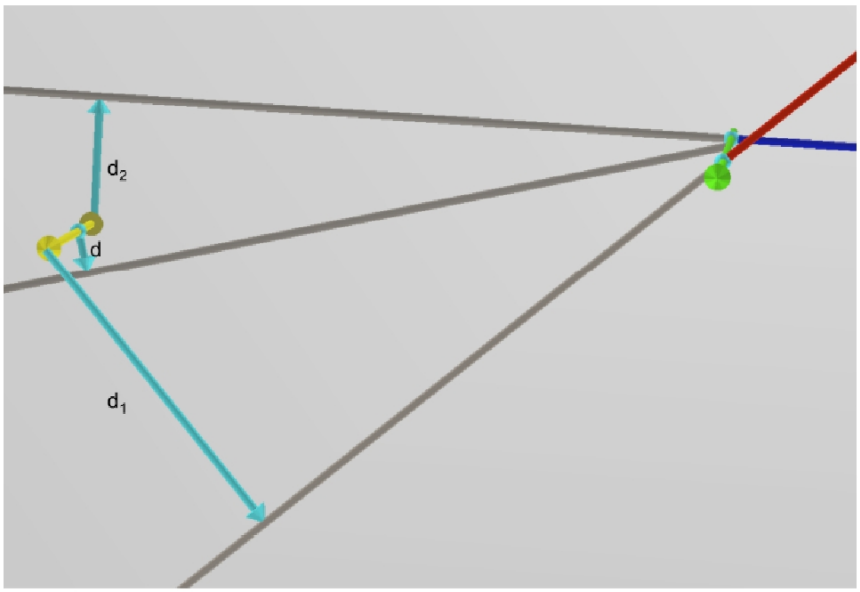

Figure 5.3: 3-D schematic view of a simulated V^0 decay showing d, d_1, and d_2. The red and blue lines are the initial momentum directions of the positive and negative daughters, respectively. In between the green knobs is the candidate's decay vertex. Gray lines illustrate the projection of the candidate and daughters' momentum towards the primary vertex (in between the yellow knobs), from which d, d_1, and d_2 are calculated.

Parallel to $\hat{\mathbf{n}}$ (Figure 5.2):

- $\mathbf{v_1}, \mathbf{v_2}$: the perpendicular distance from each plane to the primary vertex.

From this information, we construct the dimensionless variable ω (Equation 5.1) which is expected to be large for V^0-decays.

$$\omega = \ln \frac{d_1 d_2}{d^2 + v_1^2 + v_2^2} \tag{5.1}$$

Similarly, it is expected that $\mathbf{d_1}, \mathbf{d_2} > 0$. For real V^0-decays the tracks generated by the daughter particles should appear ahead of the decay vertex; therefore, the dot product $(\tilde{\mathbf{d}}_\mathbf{i} \cdot (\tilde{\mathbf{p}}_\mathbf{1} + \tilde{\mathbf{p}}_\mathbf{2}))$ should be positive.

5.3 Separation of $V^0$from background using ω

Before proceeding with further analysis, it is appropriate to explicitly define the terminology which will be used:

- Candidate: the combination of two of fully reconstructed, oppositely charged tracks. Their momentum and position information is combined to obtain the momentum and decay vertex of the expected mother particle (V^0-decay).
- True MC: those candidates whose component tracks both come from the same V^0 particle which was generated in MC2010 by PYTHIA 6.4, and for whom the V^0 mother particle is confirmed to be prompt.
- Combinatorial background: all candidates which are not real V^0-decays (identified as non-true MC in MC2010), assumed to be just random combinations of tracks, not arising from the same mother particle.

Now, we will show how ω is a good selection variable, because it was tailored to isolate V^0's from the combinatorial background. As was mentioned in the preface, V^0's have long lifetimes, so they decay a long distance from where they were created. Because we are looking for prompt particles, namely, particles which come directly from the primary vertex, this long distance between the primary vertex and the decay vertex gives the geometry of the decay some distinctive features: Firstly, the impact parameter of the candidate (d) should be small, which is easy to understand as the

momentum of the candidate should point directly towards the primary vertex if it actually came from there. Secondly, the impact parameters of the tracks that compose the candidate (d_1, d_2) should be large in comparison to d. As can be seen in Figure 5.3, the projection of the momentum of the tracks is further away from the primary vertex than the projection of the candidate. Finally, the distance from the primary vertex to the planes of the positive and negative tracks (v_1, v_2), as seen in Figure 5.2, should be small if the candidate is a well-reconstructed V^0-decay coming from the primary vertex, and not just a random track combination. It is then expected that candidates which are actually prompt V^0-decays would have a large ω value as compared to the rest of the particles and combinatorial background. This assumption is verified in Figure 5.4, where the distribution of the ω variable shows a clear separation between true MC candidates and the combinatorial background. The area to the right of the line represents the chosen selection cut of $\omega \geq 5.5$, where the true MC candidates clearly dominate over the combinatorial background.

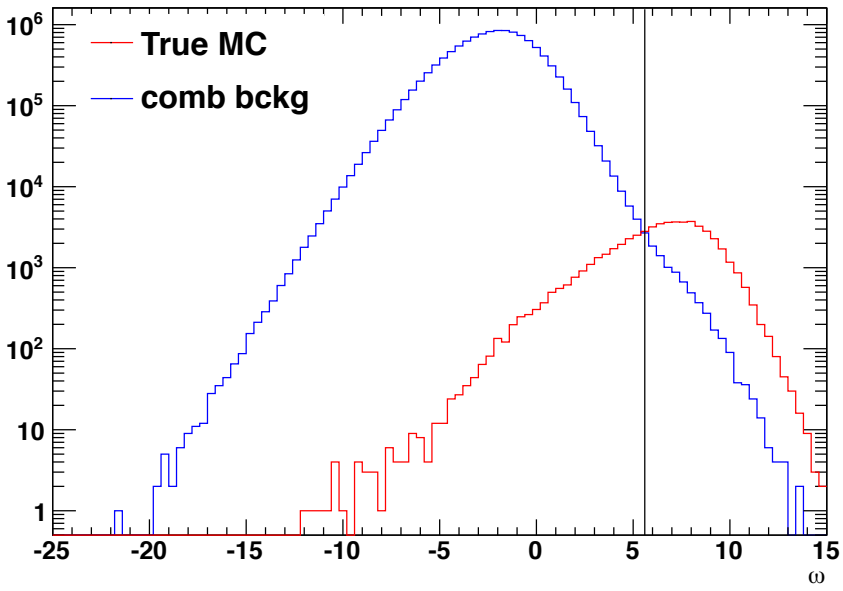

Figure 5.4: ω distribution for true MC candidates (solid red histogram) and combinatorial background (solid blue histogram) for MC2010.

5.4 Selection efficiency

The selection efficiency was checked for consistency and possible systematic corrections. The first step was to use true MC V^0candidates for MC2010 and count how many survived selection, similar to the way in which the selection cut $\omega \geq 5.5$ was defined in Section 5.3. Then, background subtracted yields for MC2010 were used to observe the effects of reconstruction efficiency and yield extraction (comparing to the counts of true MC candidates). Finally, the yields were measured on DATA2010 to observe how well MC2010 describes the data. Details are presented later in this section.

Selection efficiency is measured as follows:

$$\epsilon(sel|rec)_{i,j} = \frac{I(sel)_{i,j}}{I(sel)_{i,j} + I(nsel)_{i,j}} \tag{5.2}$$

Where $I(sel)_{i,j}$ is the number of reconstructed V^0-decays accepted by the selection, and $I(nsel)_{i,j}$ is the number of reconstructed V^0-decays that are rejected. The indices (i,j) indicate the p_T,y bin. Since this selection involves only one variable, (ω), it is straightforward to define $\epsilon(sel|rec)_{i,j}$ in terms of ω:

$$\epsilon(sel|rec)_{i,j} = \frac{I(\omega \geq 5.5)}{I(\omega \geq 5.5) + I(\omega \leq 5.5)} \tag{5.3}$$

The acceptance region ($\omega \geq 5.5$) was selected to optimize the selection of V^0candidates. In Figures 5.6 and 5.7 we can observe that candidates with $\omega \leq 5.5$ have a uniform $\pi\pi$ invariant mass distribution, meaning that they are mostly combinatorial background. On the other hand, the candidates $\omega \leq 5.5$ appear in a very dense area around the K^0_s mass and very sparsely elsewhere.

Figure 5.5 shows the ω distribution for K^0_s-decays in the acceptance region. The area to be taken into account for comparison between DATA2010 and MC2010 is $\omega \geq 2$. Here, the background subtracted yield extraction is still reliable. For values $\omega \leq 2$ the simulation shows that background contributions remain. The region $\omega \leq 2$ is therefore not used in the determination of the efficiency correction factor. Since ω doesn't show a correlation in the $\pi\pi$ invariant mass distribution, and the background

is quite homogeneous for DATA2010 and MC2010 (Figures 5.6 and 5.7), it is reliable to use background subtracted yields to estimate its distribution.

Comparing the background subtracted distribution for MC2010 to DATA2010 for non-selected ($2 \leq \omega \leq 5.5$) and selected ($\omega \geq 5.5$) V^0-decays, it is observed that:

- MC/DATA ≥ 1 for $\omega \geq 5.5$, so I(sel) is overestimated.
- MC/DATA ≤ 1 for $2 \leq \omega \leq 5.5$, so I(sel) is underestimated.
- Therefore $\epsilon(sel|rec)_{i,j}$ is overestimated by MC2010.

To measure this overestimation of $\epsilon(sel|rec)_{i,j}$, truncated estimates for MC2010 and DATA2010 are calculated using background subtracted yields in both cases as follows:

$$\hat{\epsilon}(sel|rec)_{MC} = \frac{I(\omega \geq 5.5)_{MC}}{I(2 \geq \omega \leq 5.5)_{MC} + I(\omega \geq 5.5)_{MC}} \tag{5.4}$$

$$\hat{\epsilon}(sel|rec)_{DATA} = \frac{I(\omega \geq 5.5)_{DATA}}{I(2 \geq \omega \leq 5.5)_{DATA} + I(\omega \geq 5.5)_{DATA}} \tag{5.5}$$

and from those estimates the correction factor for the MC estimate is obtained:

$$\hat{k} = \frac{\hat{\epsilon}_{DATA}}{\hat{\epsilon}_{MC}} \tag{5.6}$$

This correction factor $\hat{k}$ is applied to the efficiency calculated from simulation data $\epsilon(sel|rec)_{i,j}$ (Eq 5.3) to estimate the actual reconstruction efficiency.

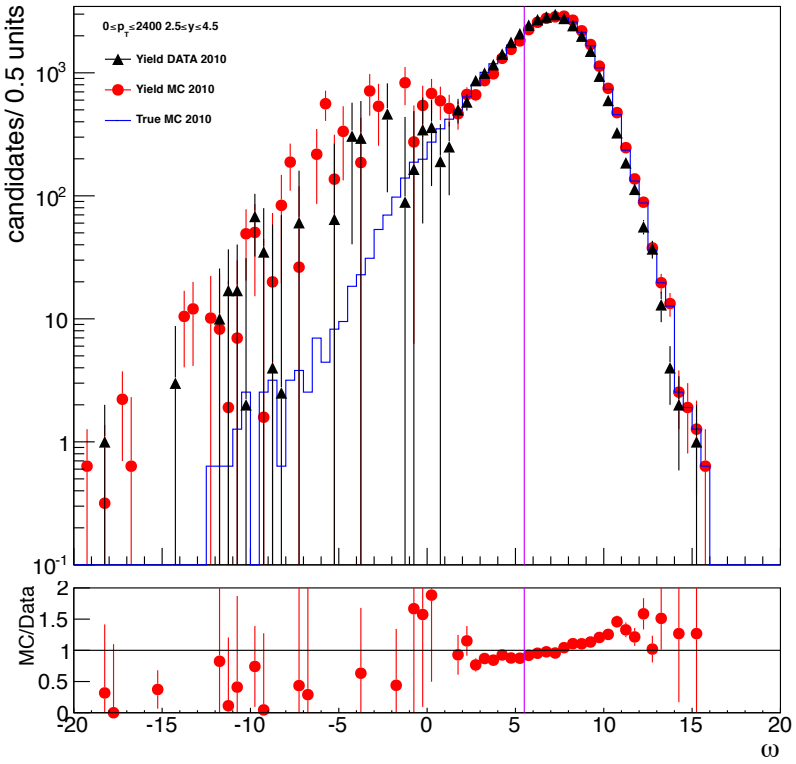

Figure 5.5: K^0_s's ω distribution from the background subtracted yields in DATA2010(black filled triangles), MC2010 (red filled circles), and true MC particles (solid blue histogram). The ratio plot shows how the simulated data underestimates data for candidates of $\omega \leq 5.5$ and starts overestimating for $\omega \geq 5.5$, hence the need for the correction factor $\hat{k}$ (Eq 5.6).

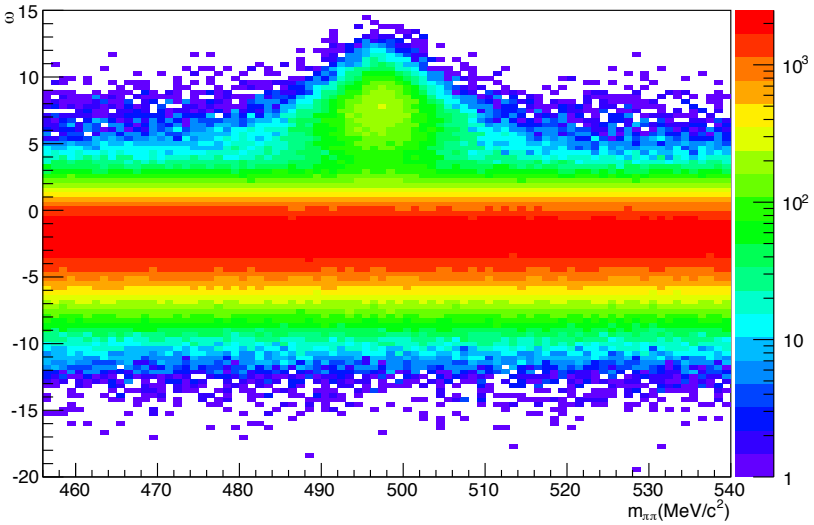

Figure 5.6: ω vs $\pi\pi$ invariant mass on DATA2010.

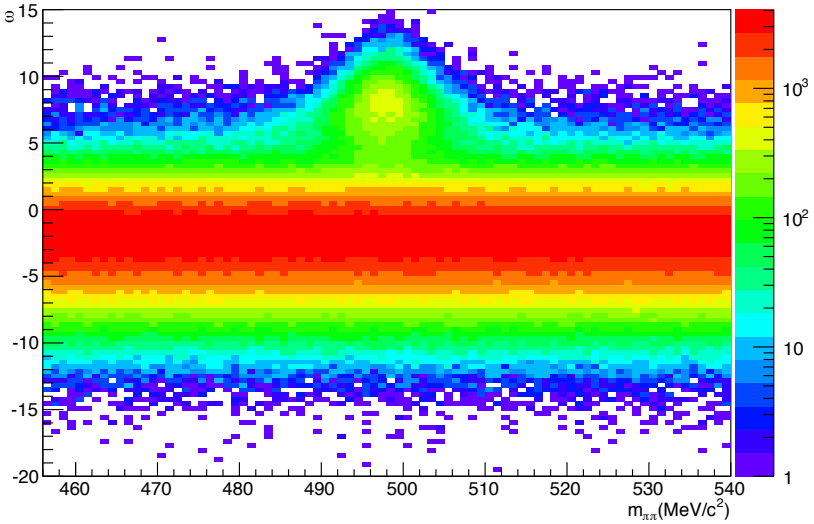

Figure 5.7: ω vs $\pi\pi$ invariant mass for MC2010.

The correction factor is measured in different ranges of transverse momentum and rapidity to check for phase space dependence. Table 5.1 shows the measured $\hat{k}$ values. The selected p_T,y bins are chosen such that there are still enough entries to see the ω distribution using background subtracted yields. The observed mean value of $\bar{k} = 0.94 \pm 0.024$ was checked for consistency with the conforming bins using a χ^2 test, which gave a p-value of 0.44, i.e., within the accuracy of this measurement there is no evidence for a phase space dependence of the correction factor. Therefore, the correction factor of $\hat{k}$=0.94 is applied uniformly for all measured p_T,y bins. The assigned systematic correction is 3% (rounding the error of $\bar{k}$). The area, which is not taken into account ($\omega \leq 2$), was measured in true MC and found to be only 7% of the total area; therefore, its contribution to $\hat{k}$ is not significant, and the small uncertainty due to truncation is already covered by the assigned systematic uncertainty.

Table 5.1: Observed $\hat{k}$ values for K^0_s-decays

p_T-y	2.5-3	3-3.5	3.5-4	4-4.5
0-600	0.98 ± 0.027	0.94 ± 0.016	0.95 ± 0.018	0.90 ± 0.036
600-2400	0.93 ± 0.017	0.97 ± 0.018	0.94 ± 0.016	0.94 ± 0.03

For Λ and $\overline{\Lambda}$, the same over-estimate of $\epsilon(sel|rec)_{i,j}$ is observed (Figure 5.8). As in the case of the K^0_s-decays, ω does not show any trend in the invariant mass distribution for DATA2010 and MC2010 (Figures 5.9 and 5.10), so obtaining its distribution via background subtracted yields is reliable. Table 5.2 shows the measured values for different p_T,y bins. The overall mean of $\hat{k} = 0.92 \pm 0.034$ is applied uniformly as a correction factor for all measured p_T,y bins. The χ^2 test in this case gives a p-value of 0.88; therefore, there is no evidence for a phase space dependence.

Table 5.2: Observed $\hat{k}$ values for Λ, $\overline{\Lambda}$,-decays

p_T-y	2.5-3	3-3.5	3.5-4
200-800	0.90 ± 0.11	0.94 ± 0.06	0.93 ± 0.11
800-2400	0.96 ± 0.09	0.86 ± 0.05	0.92 ± 0.07

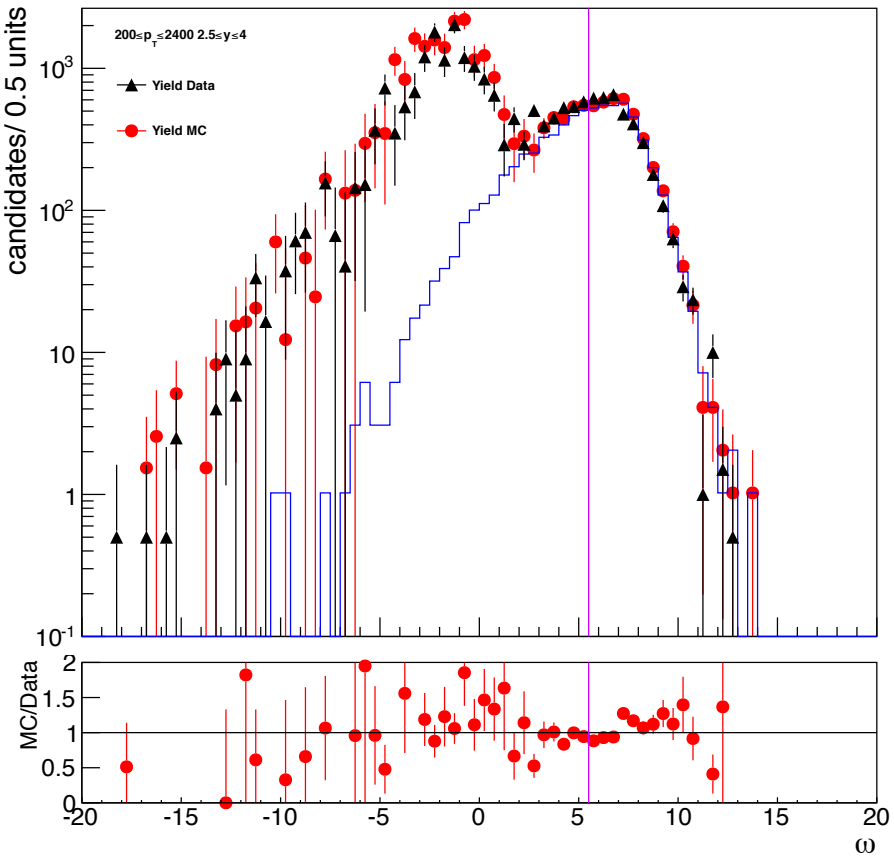

Figure 5.8: Λ, $\overline{\Lambda}$'s ω distributions from background subtracted yields in DATA2010 (black filled triangles), MC2010 (red filled circles), and true MC particles (solid blue histogram).

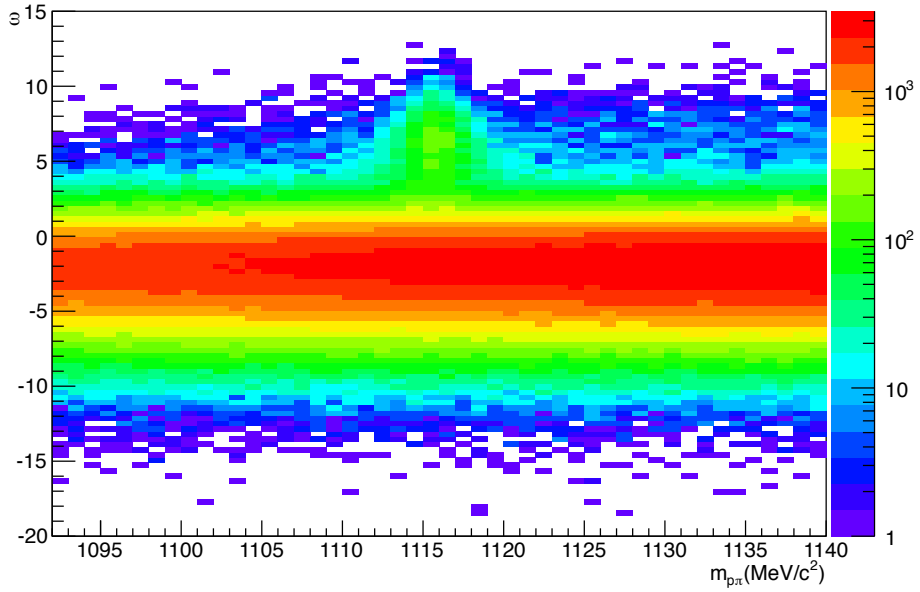

Figure 5.9: ω vs $\pi\pi$ invariant mass on DATA2010

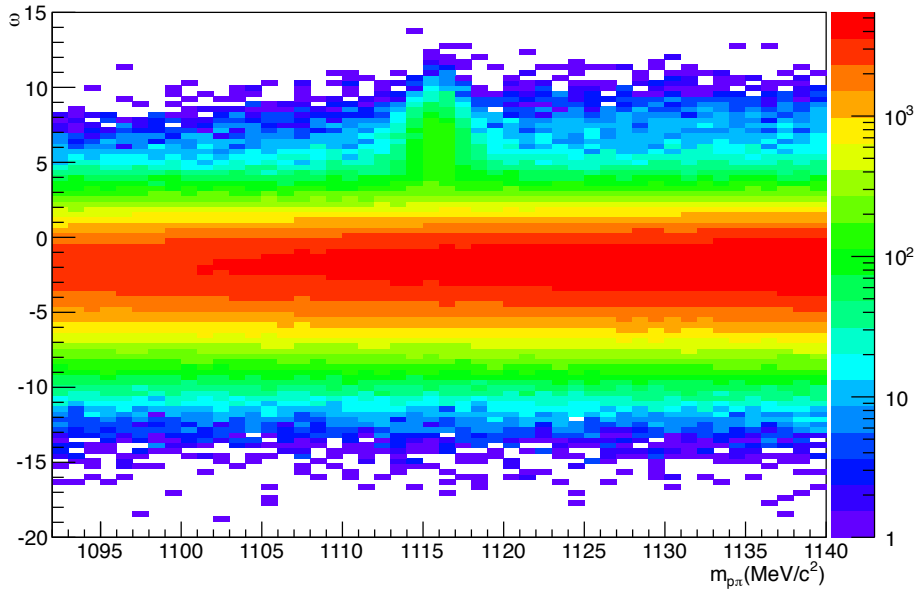

Figure 5.10: ω vs $\pi\pi$ invariant mass on DATA2010

5.5 Kinematic Analysis with Armenteros Variables

To test the event selection, we can perform a kinematic analysis using only the momentum information of the tracks via an Armenteros-Podolansky plot (Figure 5.12). Taking the components of the two daughter particles' momenta with respect to the V^0 (Figure 5.11), we plot the transverse momentum of either one (p_T) on the ordinate, and the asymmetry of the longitudinal momenta on the abscissa,

$$a_L = \frac{p_L^+ - p_L^-}{p_L^+ + p_L^-}, \tag{5.7}$$

where p_L^+, p_L^- are the longitudinal momenta of the positive and negative daughter, respectively.

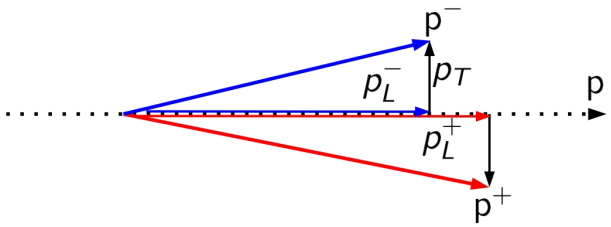

Figure 5.11: Visualization of the V^0 decay and its momentum components.

Results indicate that the selection based on ω is quite effective in isolating V^0-decays from the combinatorial background. As we can observe from Figure 5.12, after selecting candidates of $\omega \geq 5.5$, we obtain a clear structure for all V^0-decays: K_s^0-decays which can have either positive or negative a_L since both of the daughters have the same mass. Λ-decays always have positive a_L since their positive daughter, the proton, carries most of the momentum. The opposite holds for the $\overline{\Lambda}$-decays, whose heavy daughter is the negatively charged anti-proton. It is important to notice

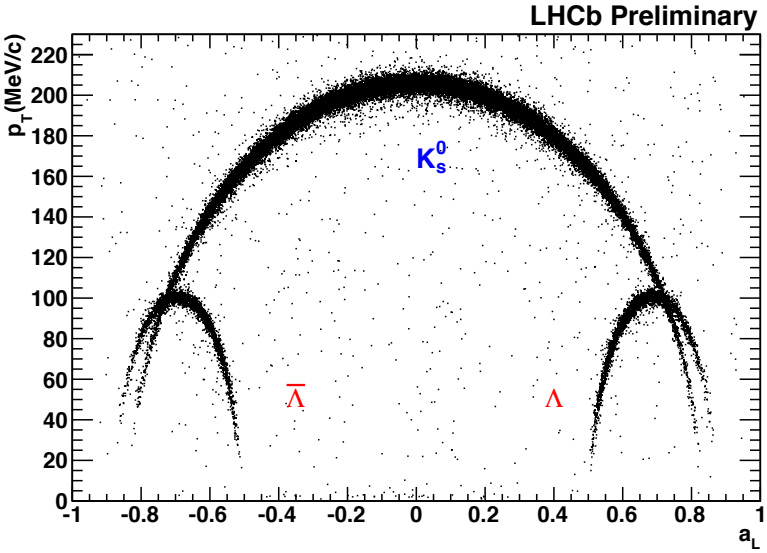

Figure 5.12: Armenteros-Podolansky plot showing the defined structure for K_s^0's and Λ's.

the intersection between K_s^0-decays and Λ-decays ($0.750 \leq a_L \leq 0.775$), where both particles overlap in phase space; this is mainly seen in the Λ invariant mass distributions as a K_s^0 background (Fig 5.13), and is fairly linear. Therefore, the linear background subtraction is reliable enough to remove the K_s^0 background on Λ-decays, and no additional cuts are required. The same holds for $\overline{\Lambda}$-decays.

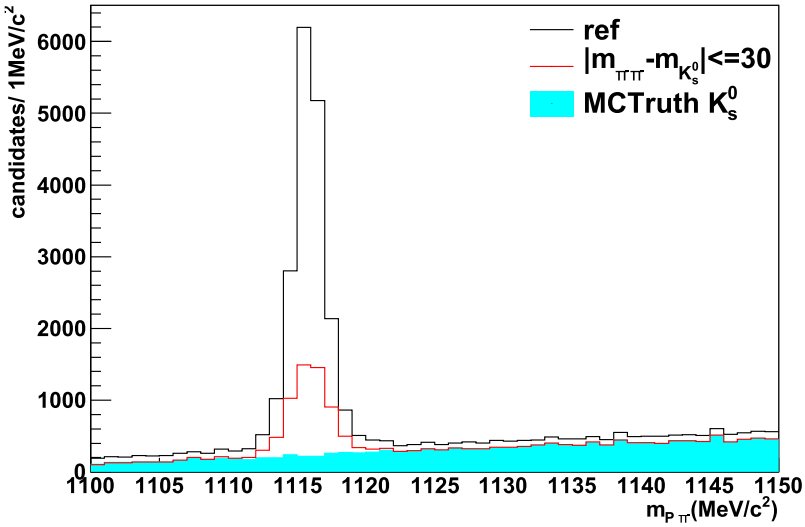

Figure 5.13: Λ-invariant mass distribution after $\omega \geq 5.5$ selection (black histogram) for MC2010, showing K_s^0 contamination from true identified K_s^0-decays(cyan filled histogram), and estimated by $|m_{\pi\pi} - 498\text{MeV/c}^2| \leq 30\text{MeV/c}^2$ (solid red histogram).

5.6 Systematic analysis of the discriminant variable ω

In order to better understand the causes behind the discrepancy in ω between MC2010 and DATA2010, its constituent variables were analyzed. The components of omega are geometric quantities. For prompt V^0's, d, v_1, and v_2 are expected to be zero, and d_1, d_2 to be affected by the decay kinematics. Due to the finite resolution of the tracking system, d, v_1, and v_2 have non-zero values, but are nevertheless smaller than d_1 and d_2. Further details are discussed in this section.

5.6.1 V^0impact parameter d

The impact parameter d is calculated geometrically, taking into account only the momentum information of the V^0-candidate. Since prompt V^0's should point to the primary vertex, it is expected for them to have small d values. Figure 5.14 shows the true MC V^0's double-binned ω vs d distribution. One can observe that most prompt

V^0's fall into the low d region. Similarly, it can be seen that the selection cut ($\omega \leq 5.5$) doesnt affect the densely populated V^0region.

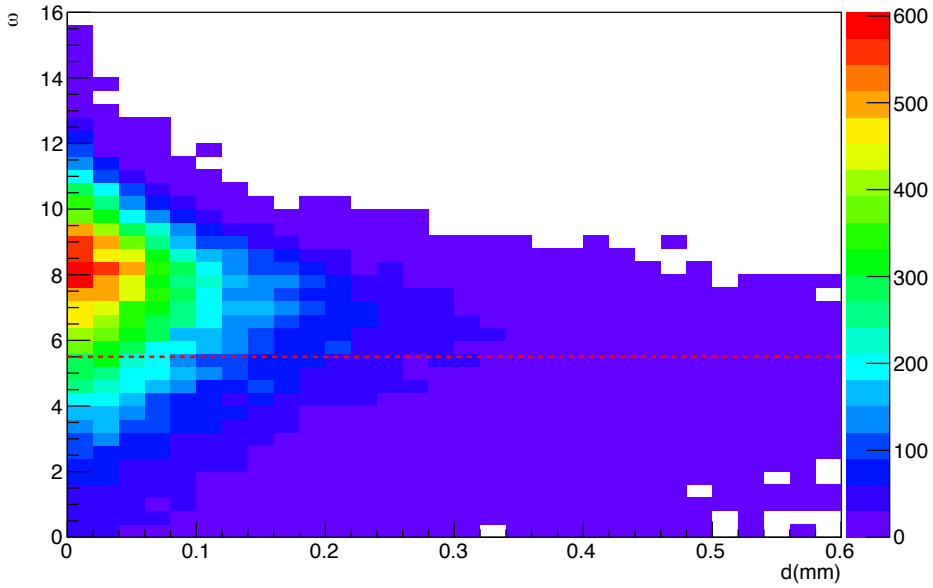

Figure 5.14: ω vs d distribution for true MC V^0's for MC2010.

Figure 5.15 shows the discrepancy between MC2010 and DATA2010 in d, which occurs mainly in the lower d values; this means that there are less events with fine resolution in DATA2010 than there are in MC2010. For this reason, there are less entries at high ω values in DATA2010. In an attempt to compensate for this discrepancy, the d distribution in MC2010 was smeared by a Gaussian distribution with σ= 0.005mm (the value which achieved the best consistency with DATA2010). The result is the red curve in Figure 5.15, which is more consistent with DATA2010 at high occupancy bins, especially in the first fine resolution bin. Chi-square values for the comparison of both MC2010 distributions versus DATA2010 are listed in Table 5.3, which show that the effect of the smearing is significant.

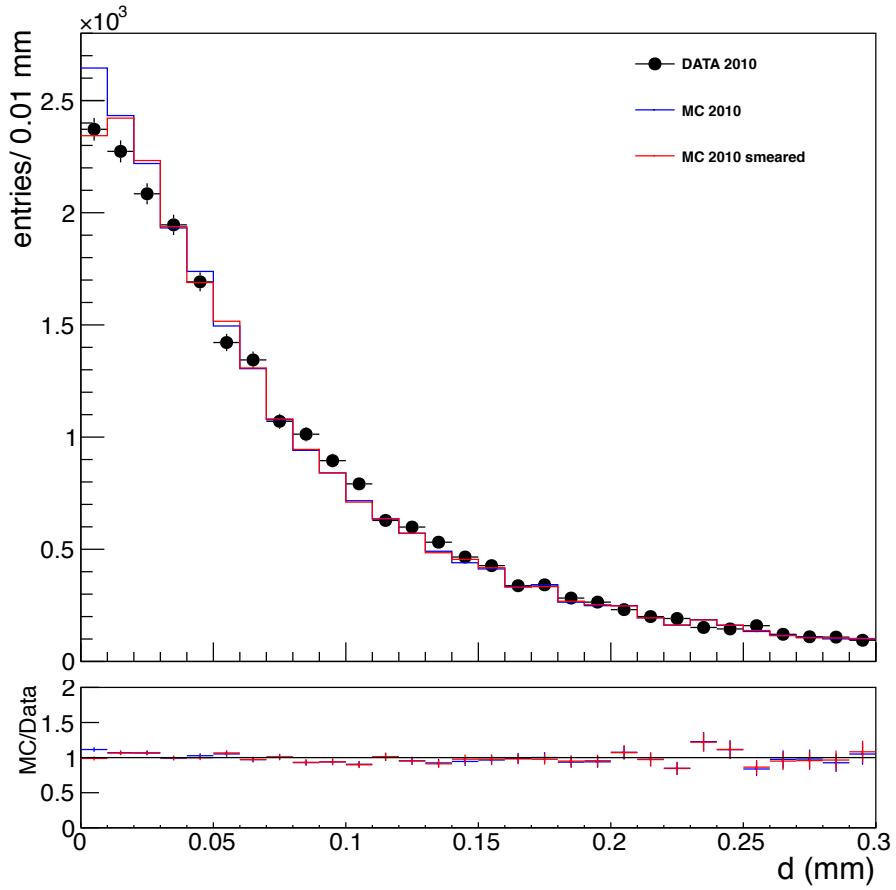

Figure 5.15: d distribution for selected candidates from DATA2010 (black filled circles), and MC2010 before and after smearing (solid blue and red histograms).

Table 5.3: Weighted chi-square test values for comparison of d from MC2010 vs DATA2010, before and after smearing.

variable	χ^2	p-value
d regular	47.6	0.016
d smeared	32.5	0.30

5.6.2 v_1 and v_2

Similarly to d, v_1 and v_2 should be very small and due only to the resolution. As well, large ω values necessarily involve small v_1 and v_2, as is shown in Figures 5.16 and 5.17. It can also be seen that non-selected ($\omega \leq 5.5$) events have a wider spread in v_1 and v_2 than selected events. This confirms the observation made from the d distribution that selected events in general have better resolution than non-selected.

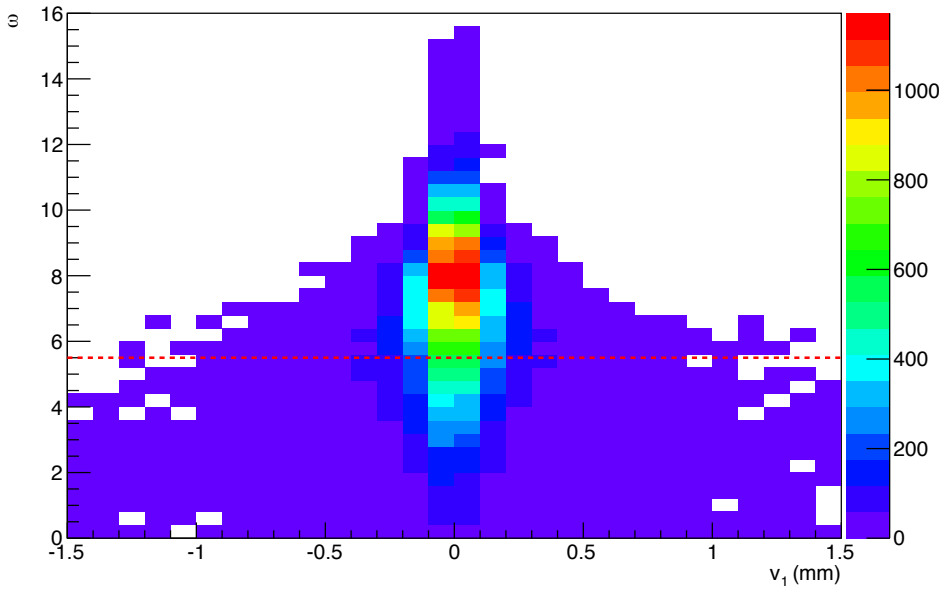

Figure 5.16: ω vs v_1 distribution of true MC V^0's for MC2010.

To prove the hypothesis that v_1 and v_2 are the result of the resolution and not kinematics, scatter plots of v_1 and v_2 against the flight length (Figure 5.18, 5.19) are presented, which show no correlation between the plotted variables.

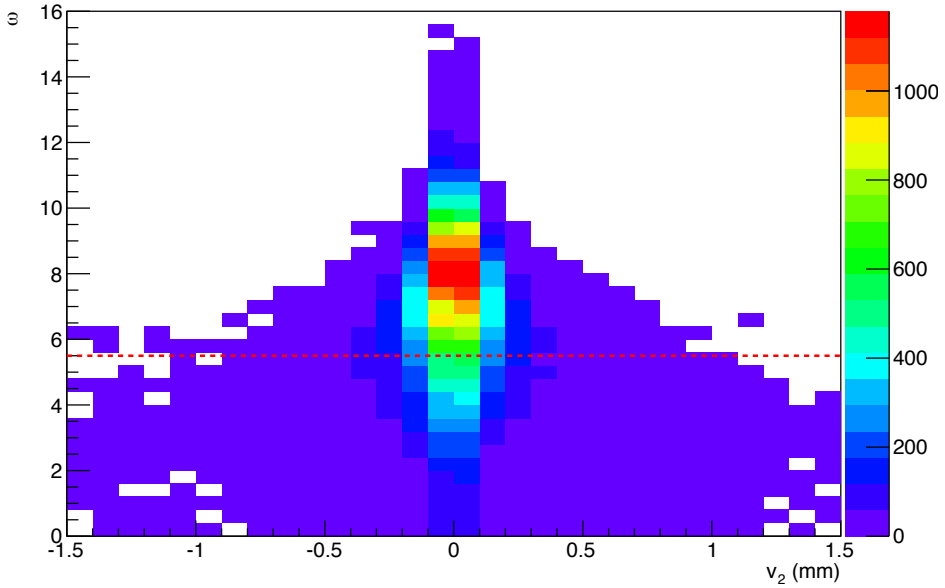

Figure 5.17: ω vs v_2 distribution of true MC V^0's for MC2010.

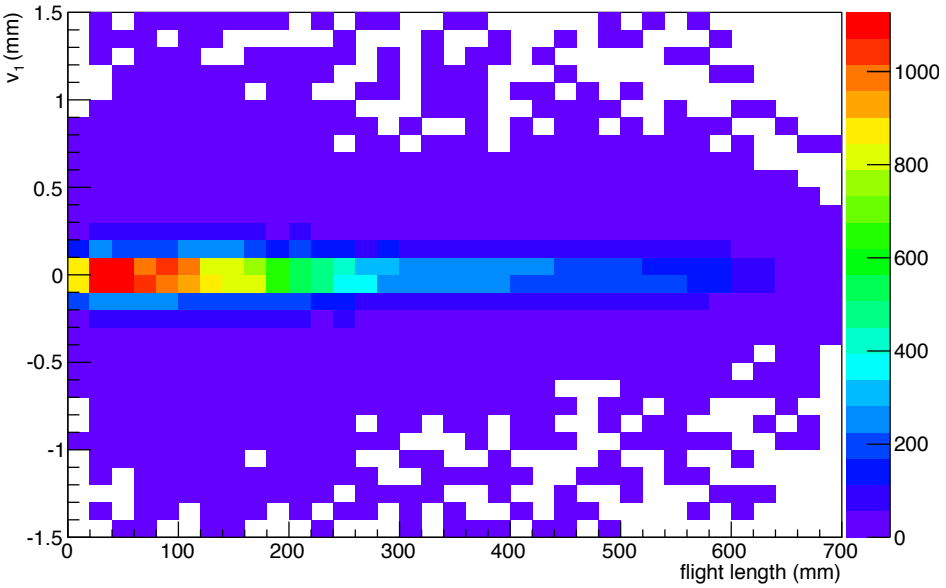

Figure 5.18: v_1 vs flight length distribution of true MC V^0's for MC2010.

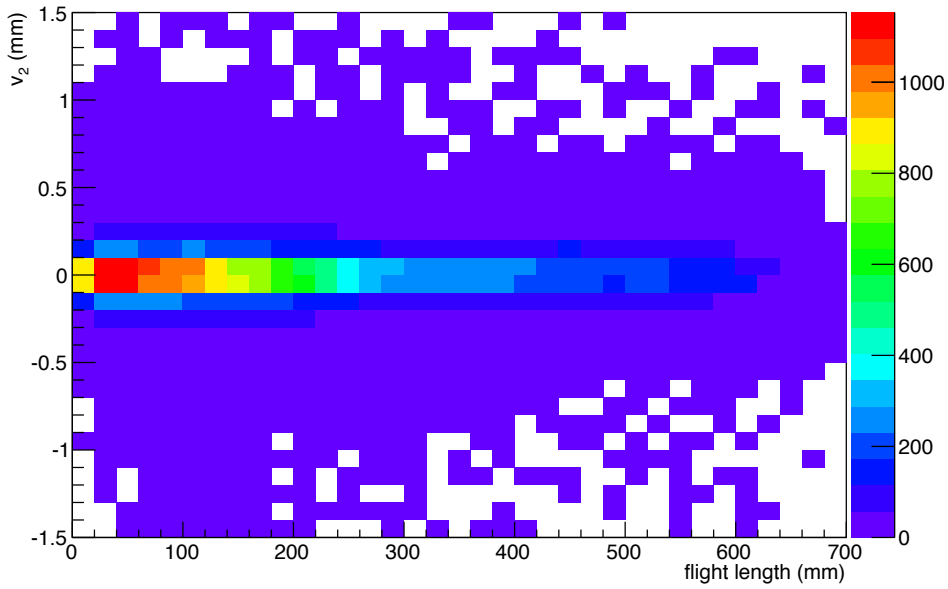

Figure 5.19: v_2 vs flight length distribution of true MC V^0's for MC2010.

In order to make v_1 and v_2's MC2010 distribution consistent with the data, the variables were smeared by a Gaussian distribution with σ= 0.015 mm (the value which achieved the best consistency with DATA2010). The resulting smeared variables are more consistent with DATA2010 (Figures 5.20, 5.21), the effect being more significant in the center bins, which have large statistics and which contribute to large ω values. Chi-square values for the comparison of both MC2010 distributions versus DATA10 are listed in Table 5.4, showing that the smeared distributions are more consistent with DATA2010. From this it is understood that MC2010 has better resolution than that observed in DATA2010.

Table 5.4: Weighted chi-square test value for comparison of v_1, v_2 for MC2010 vs DATA2010, before and after smearing.

variable	χ^2	p-value
v_1 regular	36.8	0.15
v_1 smeared	27.7	0.53
v_2 regular	31.96	0.32
v_2 smeared	26.59	0.59

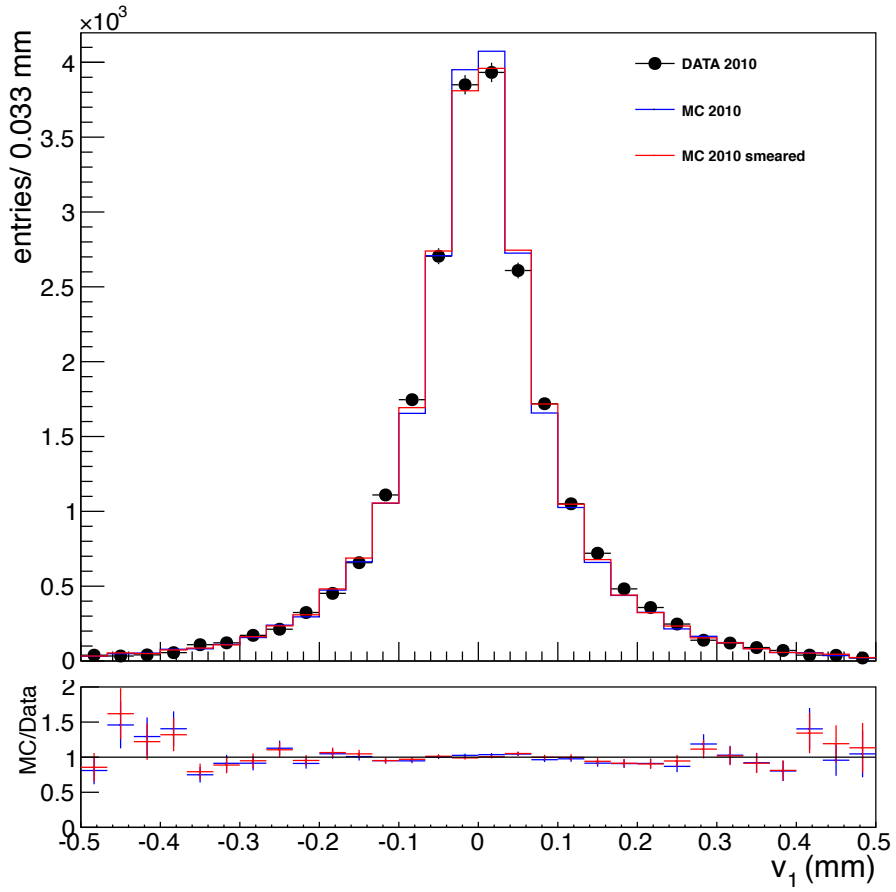

Figure 5.20: v_1 distribution for selected candidates from DATA2010 (black filled circles),and MC2010 before and after smearing (solid blue and red histograms).

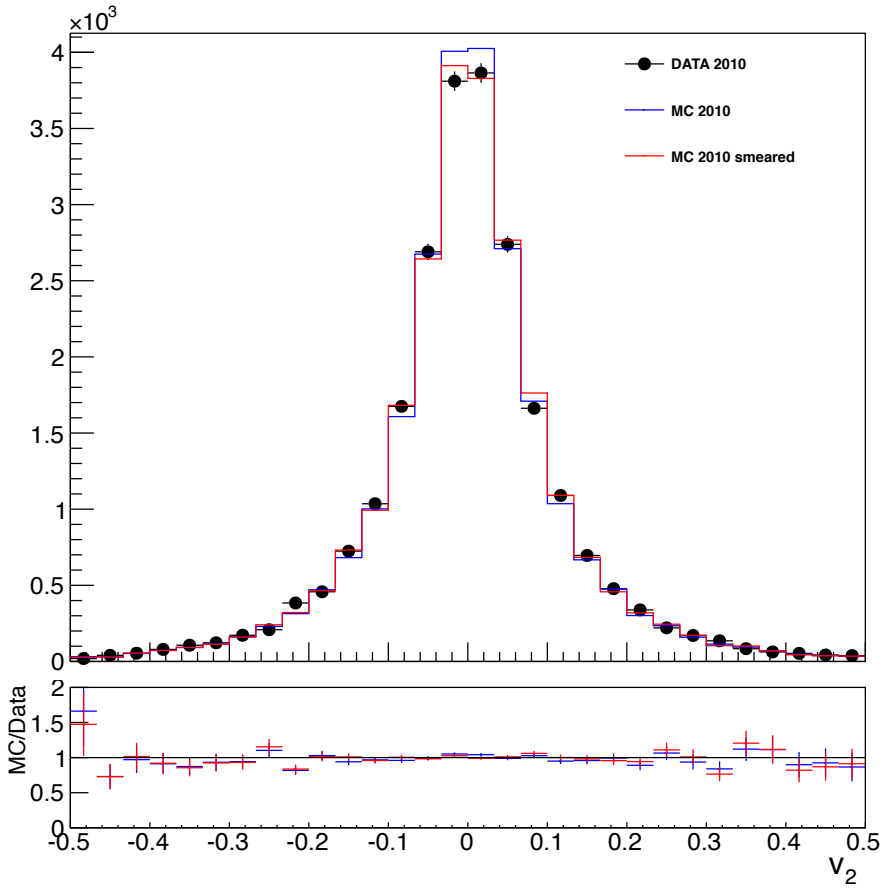

Figure 5.21: v_2 distribution for selected candidates from DATA2010 (black filled circles),and MC2010 before and after smearing (solid blue and red histograms).

5.6.3 Track impact parameters d_1 and d_2

In contrast to d,v_1, and v_2, the parameters d_1 and d_2 are more strongly related to the kinematics of the V^0-decay than to the resolution, and should depend on the flight length. The more the V^0's fly away from the primary vertex, the more the projection of the daughters momentum move further away from the primary vertex. Figures 5.22 and 5.23 illustrate the direct dependence between d_1 and d_2 and the flight lengths of the V^0-candidates. It can be observed that large d_1 and d_2 values necessarily involve long flight distances, and vice-versa.

The impact of d_1 and d_2 on the selection variable ω is clearly expected to be a direct dependence. This is confirmed in Figures 5.24 and 5.25. It is also observed that selected candidates ($\omega \geq 5.5$) have larger d_1 and d_2 values than non-selected ($\omega \leq 5.5$). Consequently, because d_1 and d_2 are directly correlated with flight length, selected candidates also have longer flight lengths than non-selected. The distribution of d_1 and d_2 for MC2010 is consistent between MC2010 and DATA2010. The values are smeared by the same factor as used for v_1 and v_2, and no observable difference is shown between the smeared and regular distributions of d_1 and d_2.

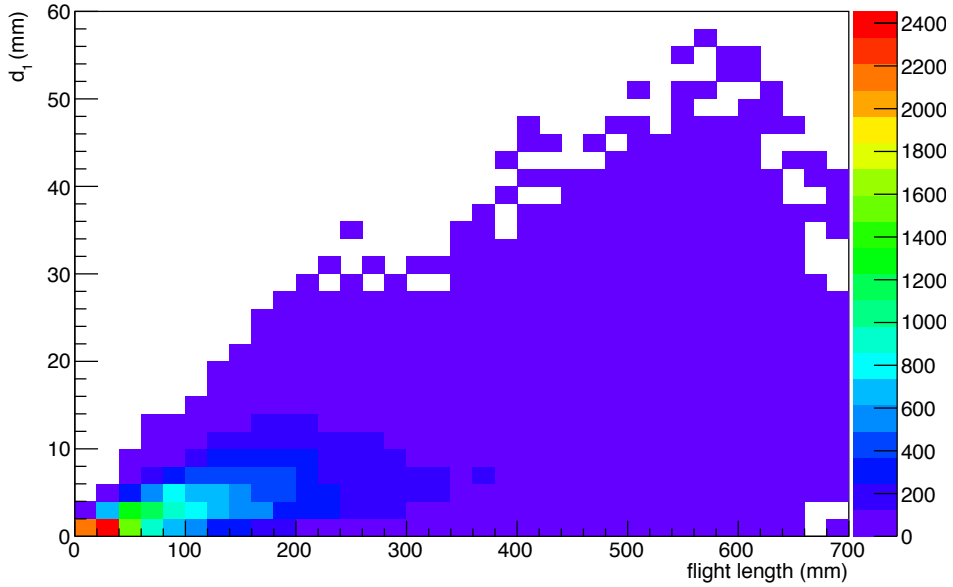

Figure 5.22: d_1 vs flight length distribution of true MC V^0's for MC2010.

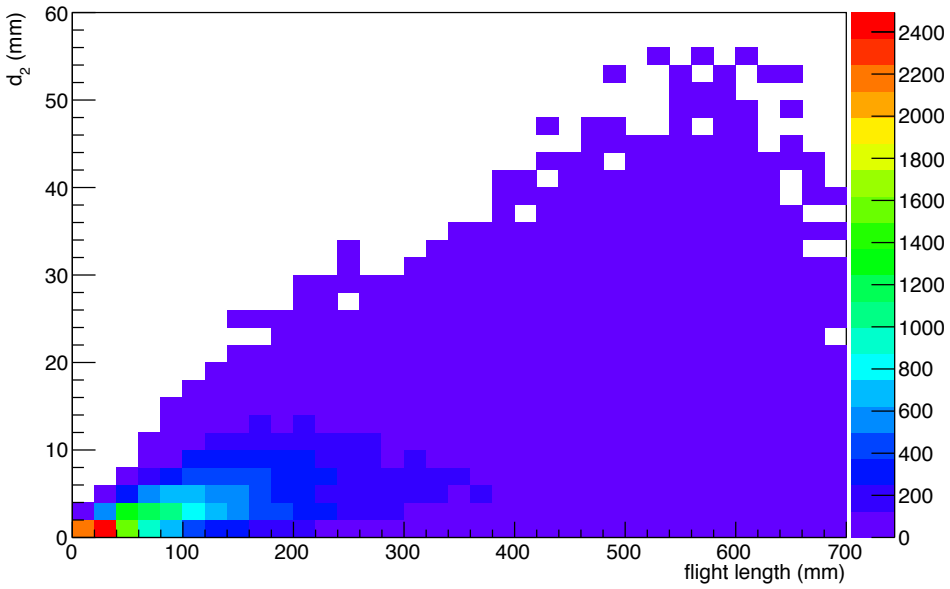

Figure 5.23: d_2 vs flight length distribution of true MC V^0's for MC2010.

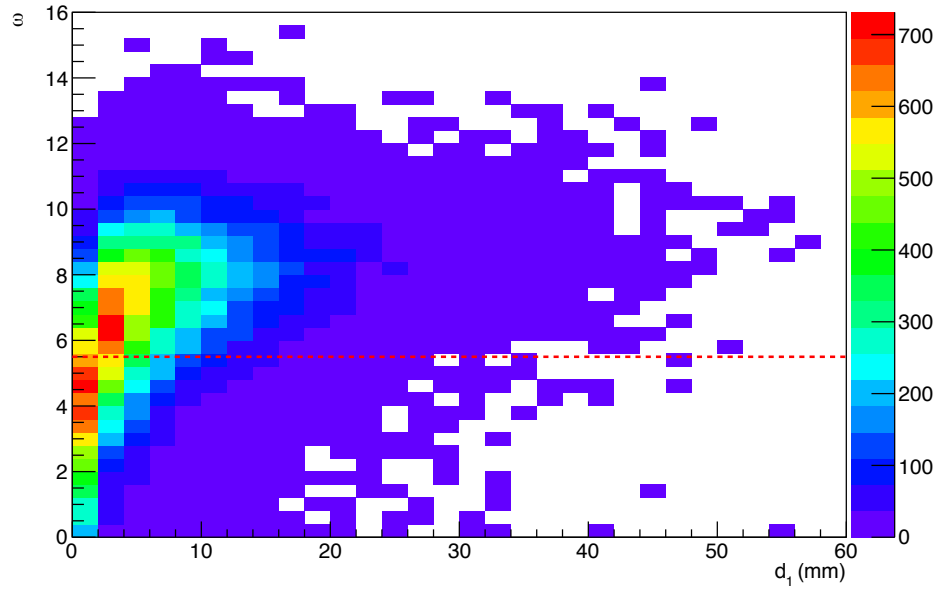

Figure 5.24: ω vs d_1 distribution of true MC V^0's for MC2010.

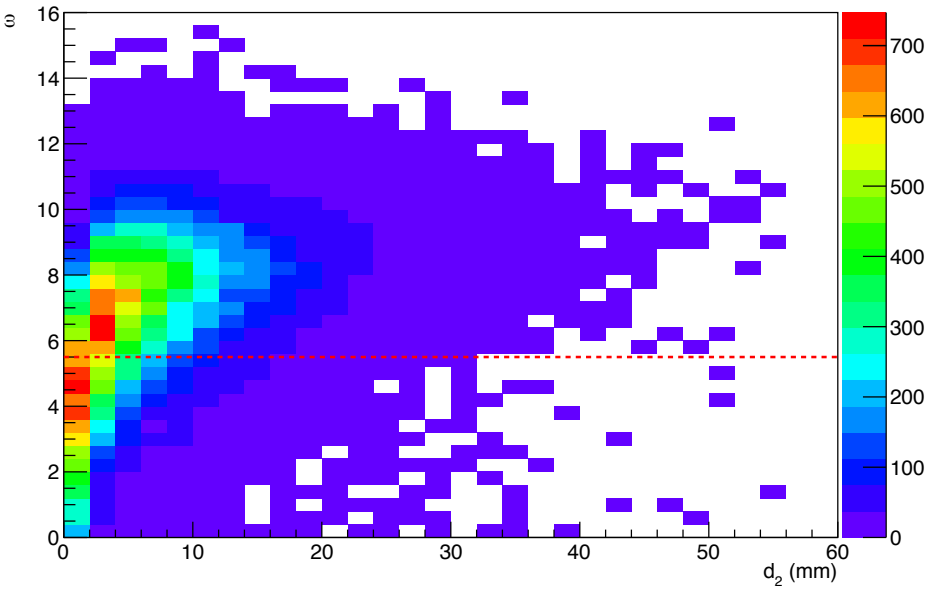

Figure 5.25: ω vs d_2 distribution of true MC V^0's for MC2010.

5.6.4 Resolution effect on ω

The observed improvement in consistency with the data for d, v_1, and v_2 obtained by smearing was implemented on ω. For this purpose, ω's distribution was recalculated using smeared d, v_1, and v_2 values, assuming that they are independent variables, which can be confirmed by Figures 5.28 and 5.29. Figure 5.30 shows the comparison of the original distribution for MC2010 before (blue histogram) and after smearing (red histogram). Clearly, after smearing, the ω's distribution in MC2010 is more consistent with DATA2010, especially for large ω values. It can be seen that the MC/DATA ratio after smearing approaches closer to 1 than before. It is therefore understood that one of the main causes for the different ω distributions is the difference in resolution. Nevertheless, the smearing is used only to understand the origin of the discrepancy. The correction in the selection efficiency is estimated by the correction factor k described in section 5.4.

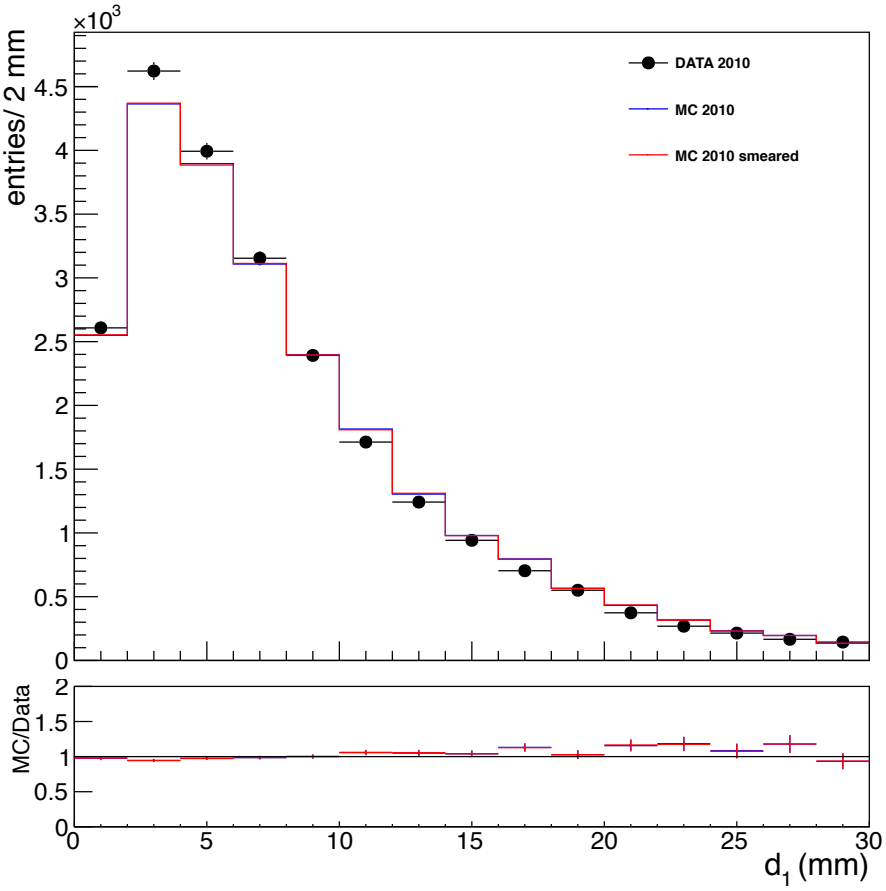

Figure 5.26: d_1 distribution for selected candidates from DATA2010 (black filled circles), and MC2010 before and after smearing (solid blue and red histograms).

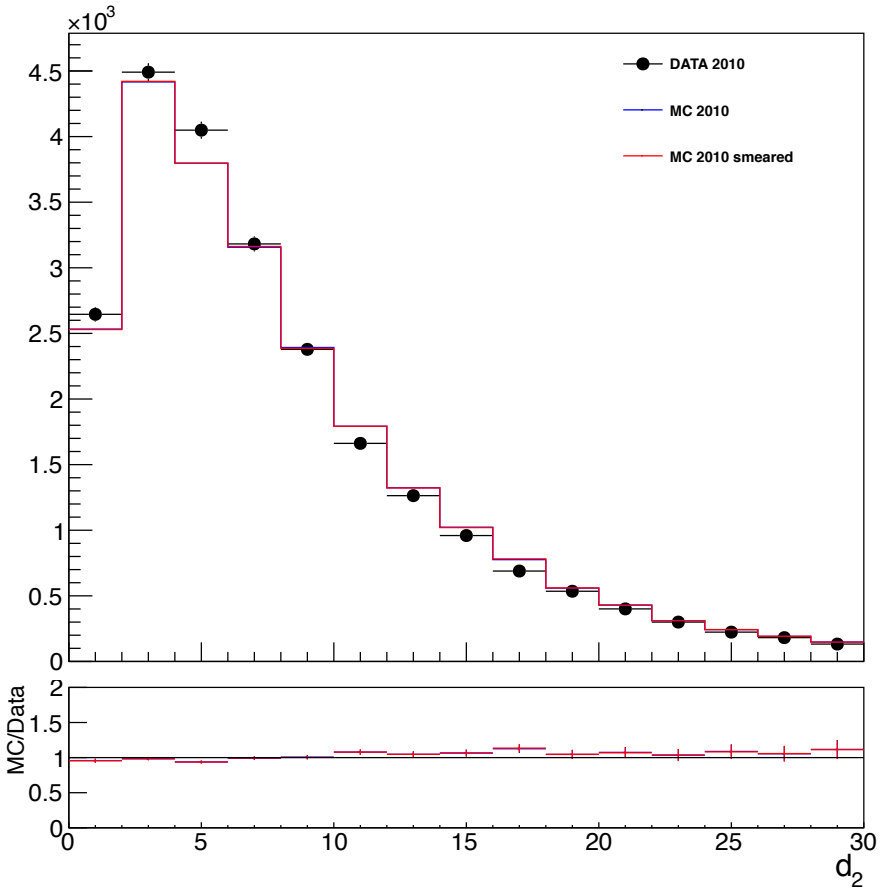

Figure 5.27: d_2 distribution for selected candidates from DATA2010 (black filled circles), and MC2010 before and after smearing (solid blue and red histograms).

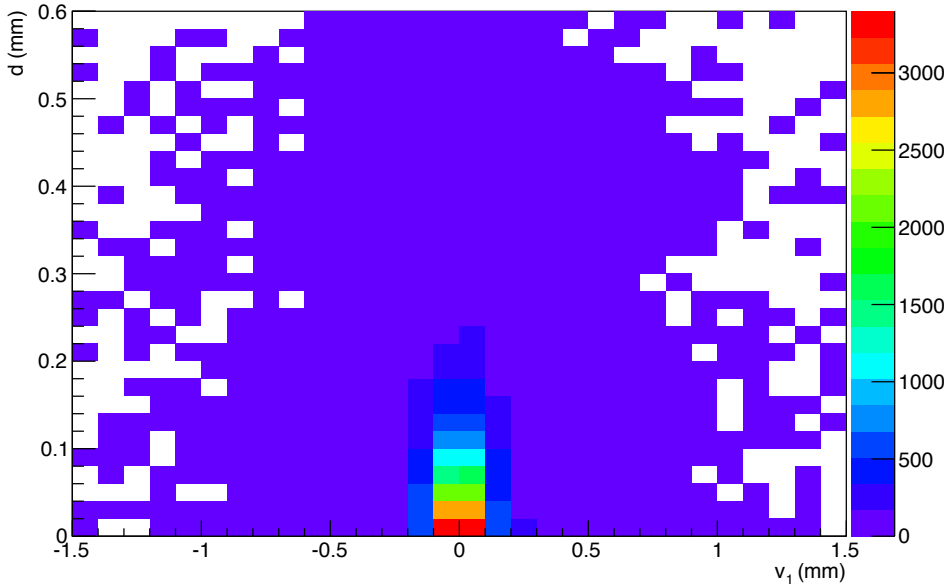

Figure 5.28: d vs v_1 distribution of true MC V^0's for MC2010.

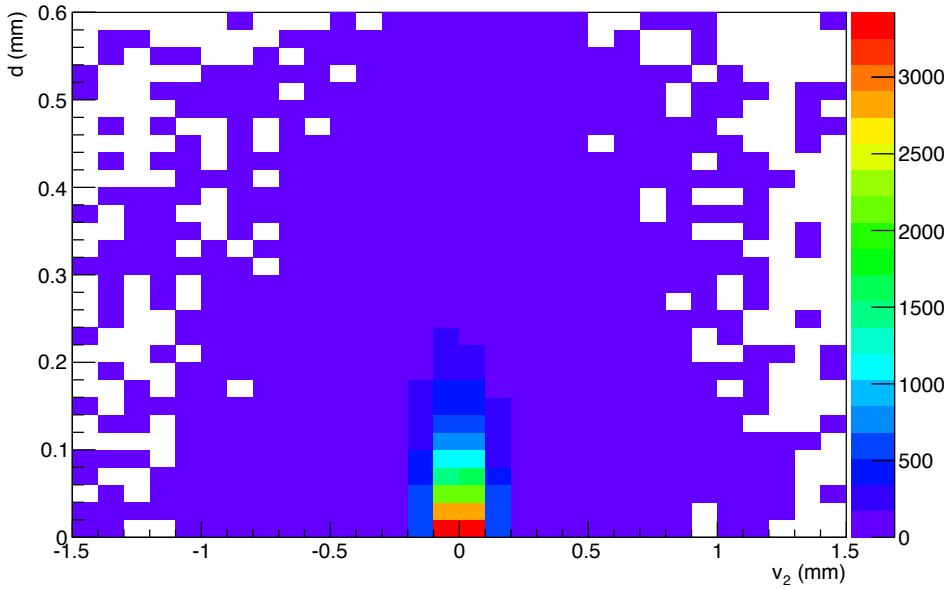

Figure 5.29: d vs v_2 distribution of true MC V^0's for MC2010.

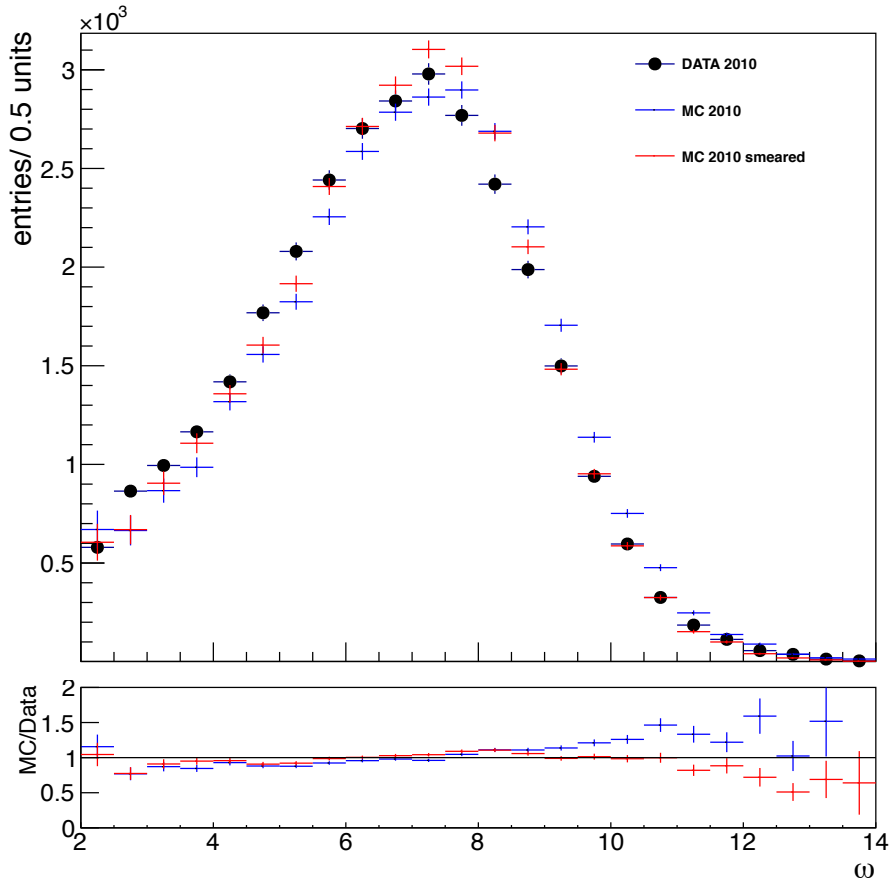

Figure 5.30: ω distribution estimated via background subtracted yields for DATA2010 (black filled circles),and MC2010 before (blue histogram) and after smearing (red histogram).

Chapter 6

Cross-checks

The properties of reconstructed and selected V^0-decays were analyzed in order to understand how suitable MC2010 is to reproduce DATA2010. Comparisons for several kinematic variables were made using background subtracted yields. The same procedure was applied for both cases.

6.1 Invariant mass

The procedures for yield extraction for DATA2010 and efficiency estimation for MC2010 rely on the invariant mass distributions. Figure 6.1(a) shows that for K^0_s-decays, signal peaks in MC2010 are shifted slightly towards higher invariant mass values; however, they still fall within the chosen signal window so that the extracted signal yield is only marginally affected (less than 0.1%). The yield extraction method used for this analysis (Subsection 4.3.1) was tested on MC2010 (Section 7.1) and was found to be reliable. For Λ and $\overline{\Lambda}$ (Figures 6.2(a) and 6.2(a)), the signal to background ratio is higher for DATA2010 as compared to MC2010, which indicates that in MC2010 the baryon production is underestimated. In this case, MC2010 distributions are normalized to match the background area in DATA2010, in order to show the clear differences in the signal peaks. However, since the background distribution has the same shape, and background subtraction was observed to be accurate in MC2010 (Figure 5.5), this underestimation does not affect the efficiency determination.

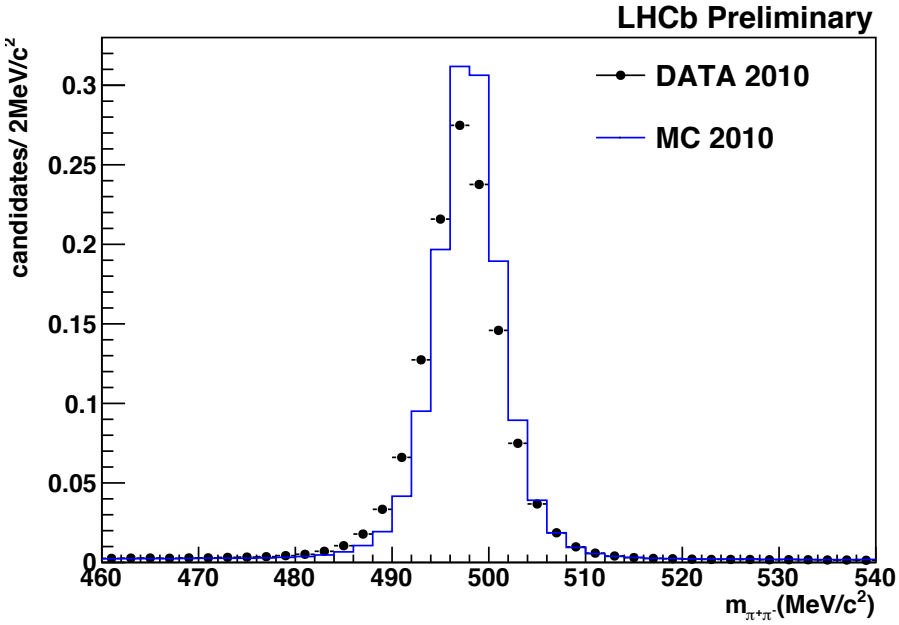

(a) Magnet Down

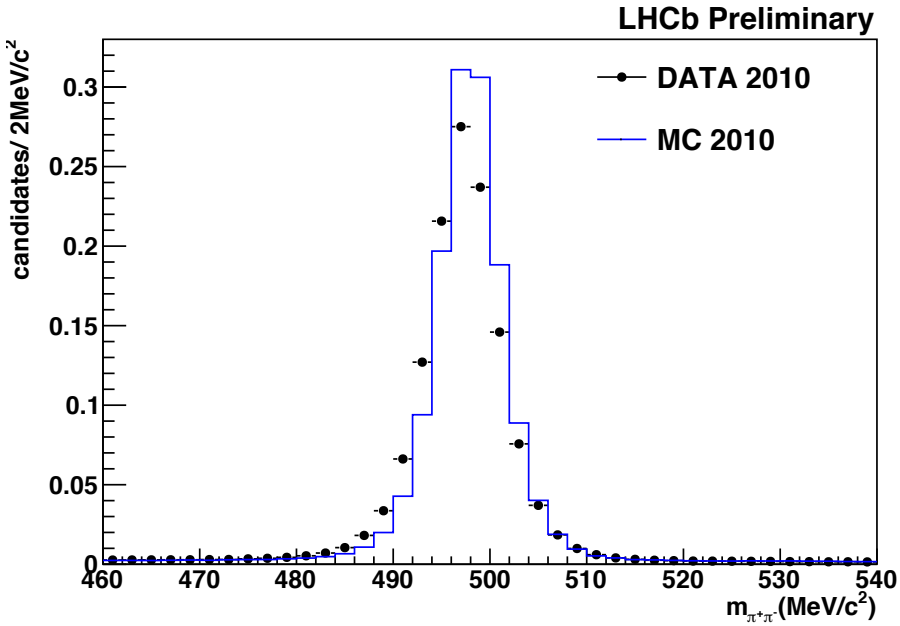

(b) Magnet Up

Figure 6.1: Invariant mass distribution of K_s^0-decays after selection from DATA2010 (black filled circles) and MC2010 (solid blue histogram), normalized to match signal yields. This normalization was chosen because the background contribution in K_s^0-decays is insignificant compared to Λ and $\overline{\Lambda}$-decays.

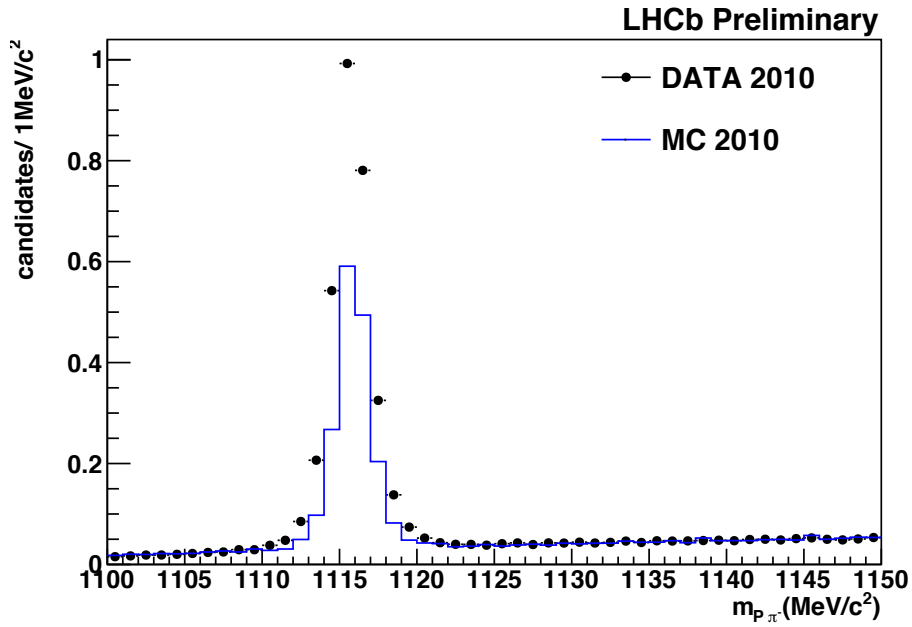

(a) Magnet Down

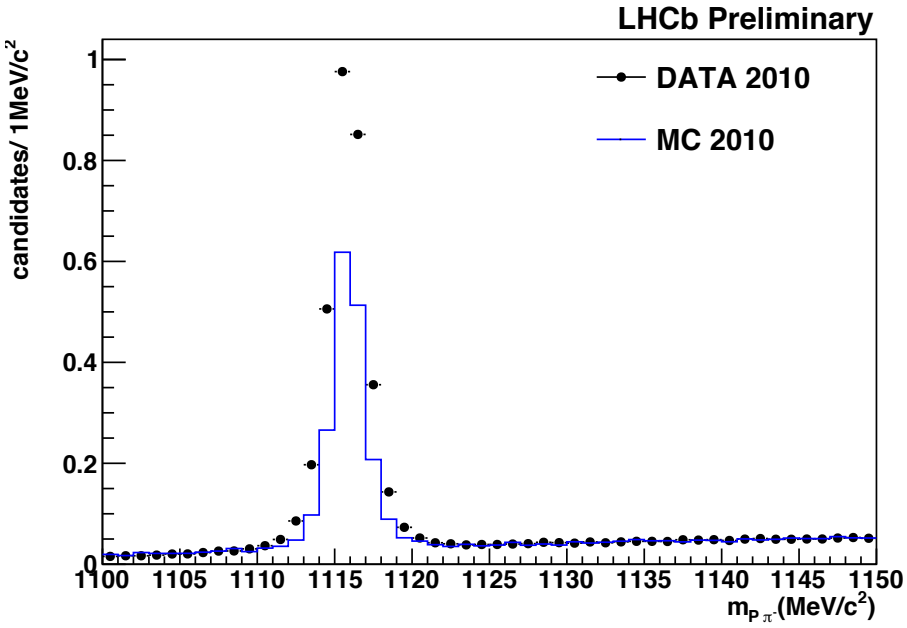

(b) Magnet Up

Figure 6.2: Invariant mass distribution of Λ-decays after selection from DATA2010 (black filled circles) and MC2010 (solid blue histogram), normalized to match the background area in both distributions.

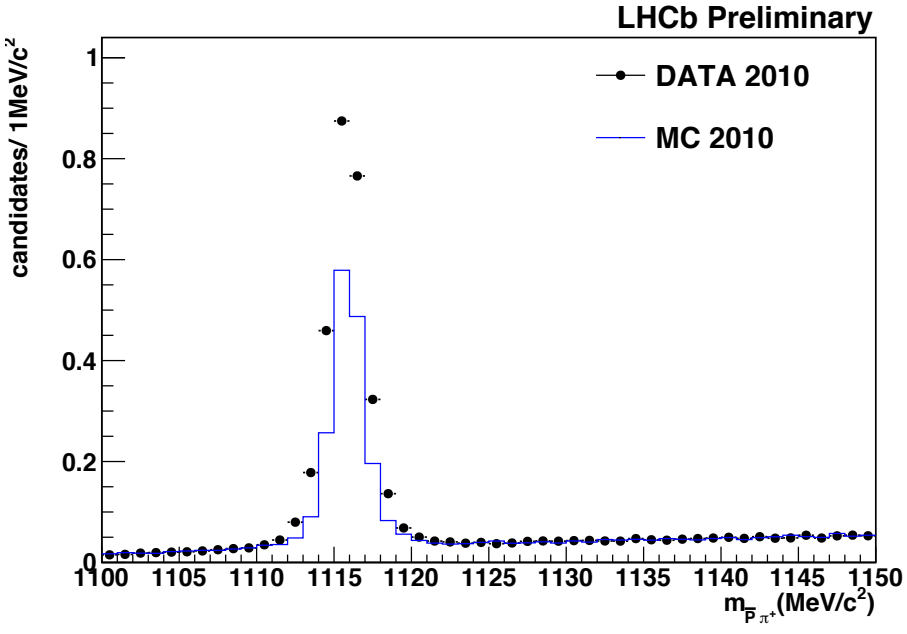

(a) Magnet Down

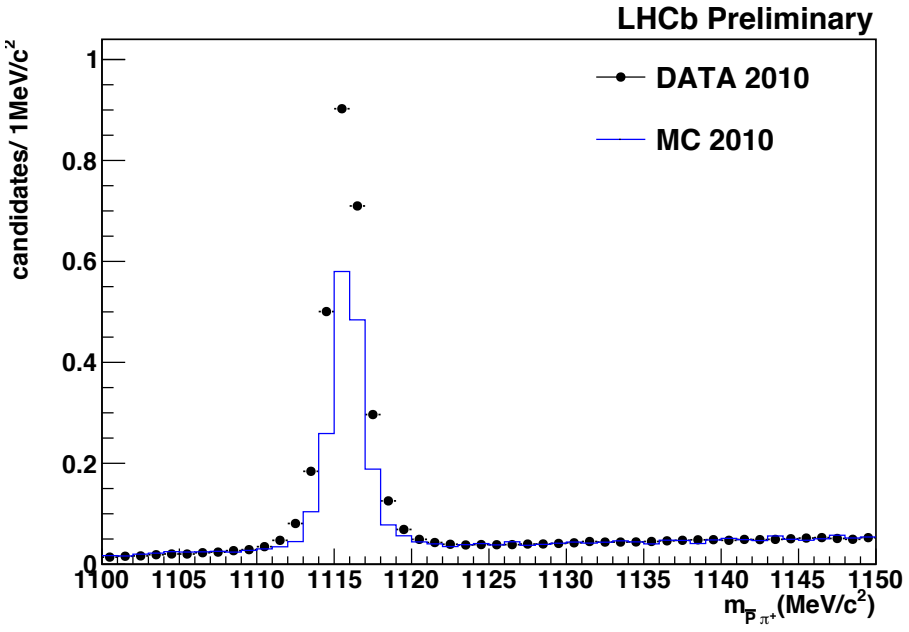

(b) Magnet Up

Figure 6.3: Invariant mass distribution of $\overline{\Lambda}$-decays after selection from DATA2010 (black filled circles) and MC2010 (solid blue histogram), normalized to match the background area in both distributions.

6.2 Rapidity

The rapidity (y) distributions (Figures 6.4 and 6.5) show a qualitative agreement between MC2010 and DATA2010. Discrepancies are on the order of 6%. Since the analysis was performed double differentially in bins of p_T and y, there is no weighting for this variable, nor for p_T.

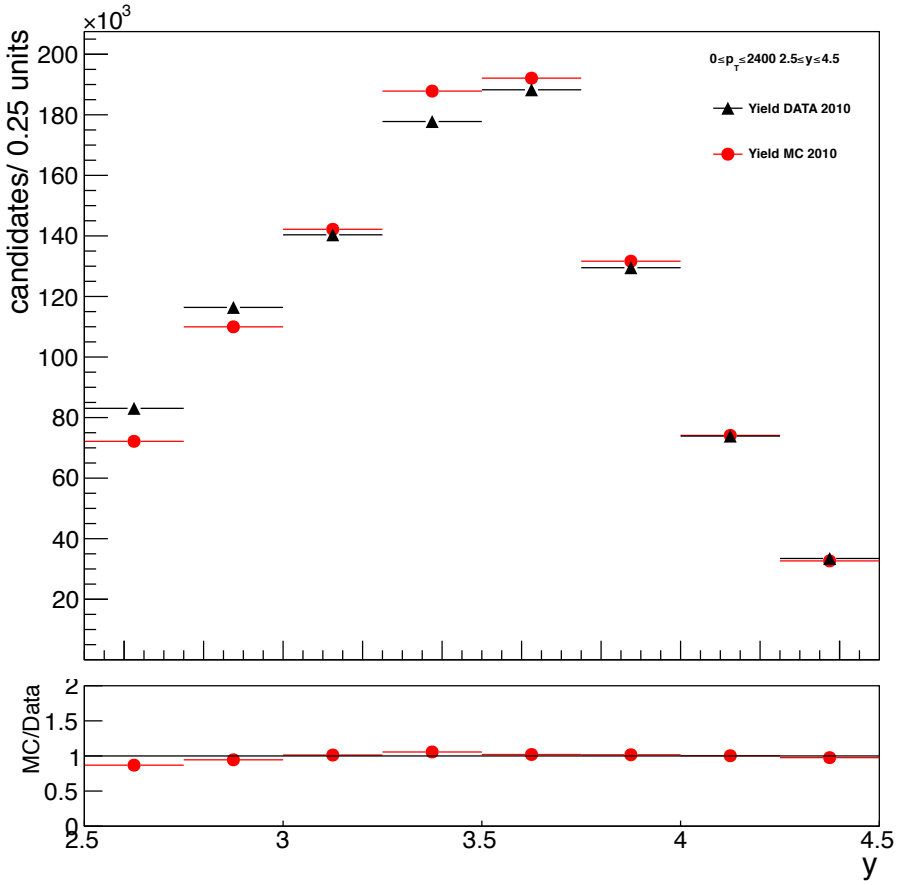

Figure 6.4: Observed y distribution of reconstructed and selected K^0_s-decays for DATA2010 (black filled circles) and MC2010 (red filled circles). MC2010 is normalized to match DATA2010 statistics.

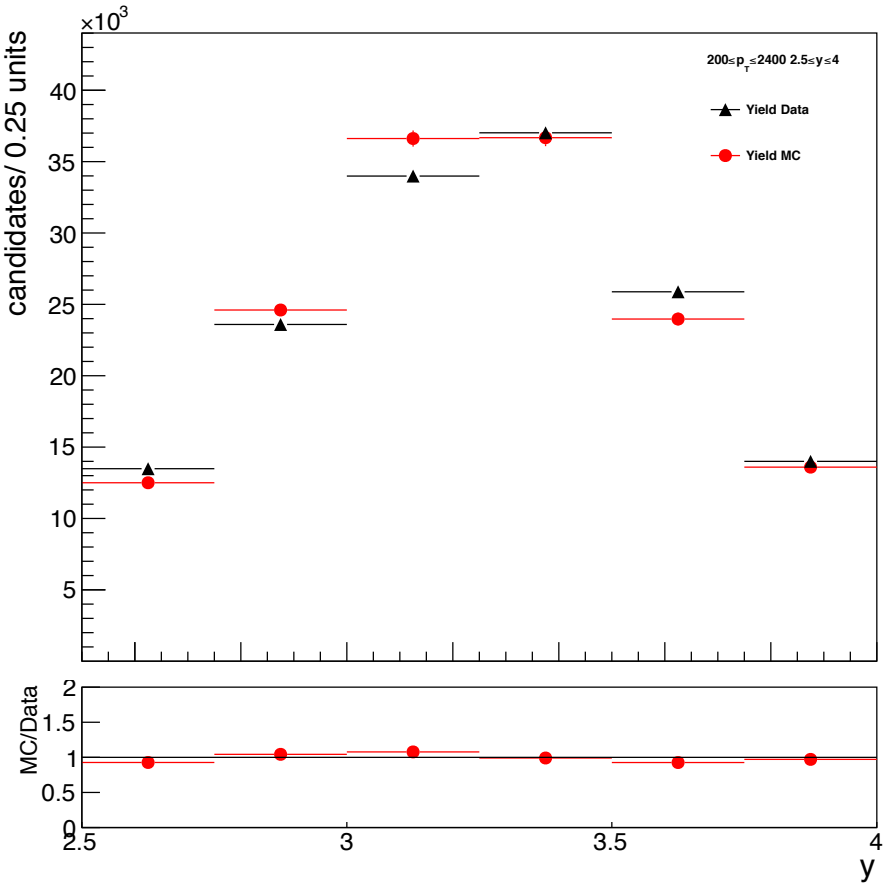

Figure 6.5: Observed y distribution of reconstructed and selected Λ and $\overline{\Lambda}$-decays for DATA2010 (black filled circles) and MC2010 (red filled circles). MC2010 is normalized to match DATA2010 statistics.

6.3 Flight length and cτ

Flight length and decay time distributions were analyzed in parallel. Flight length is important because the reconstruction and selection efficiency depend on where the particles decay and other correlated factors. On the other hand, the variable $c\tau$ takes into account the observed momentum, which differs between MC2010 and DATA2010 and thus provides additional information.

Flight length distributions for the reconstructed and selected candidates are shown in Figures 6.6 and 6.7 for K^0_s and Λ, $\overline{\Lambda}$-decays, respectively. The first noticeable feature is the presence of a double structure. Keeping in mind that only long tracks are used in the analysis, this structure can be explained by the positioning of modules in the VELO detector (Figure 3.8, Top). After the interaction region, there comes the primary zone, with a high density of modules which cover up to approximately 35 cm after the interaction region; this gives us the first component. After the primary zone follows an almost empty space, and then there comes the final part of the VELO, which has only 4 modules on each side; the second distribution comes from here. The second distribution is clearly smaller, since the density of modules is significantly less than in the primary zone, so V^0's decaying there have a smaller probability of being reconstructed. Figure 6.8 shows the reconstruction efficiency in flight length bins where the double structure due to the detector module setup is present.

Flight length distributions are also distorted due to event reconstruction and candidate selection. Long-lived V^0's generally decay out of VELO acceptance, and therefore the tracks of their daughter particles are not reconstructed as long tracks. As a consequence, flight lengths are only reconstructed up to values around 70 cm. In addition, short-lived V^0-decays are removed, since the selection variable ω tends to reject candidates that have small impact parameters on the daughter particles (d_1, d_2), and this is directly correlated with the flight length (Figure 5.22). Due to these short lived V^0's, there are more candidates in MC2010 as compared to DATA2010. It was seen that MC2010 has a high resolution such that its signal decays have small v_1 and v_2 values, resulting in larger ω values and acceptance by the selection (Subsection 5.6.3); on the contrary, for DATA2010, having larger values of v_1 and v_2 compared

to MC2010 results in smaller ω values which are not accepted by the selection. This effect is directly correlated with candidate selection based on the discriminant variable ω. Therefore, this discrepancy is already taken into account by the correction factor $\hat{k}$ (Section 5.4). In this analysis, an estimate for the decay time $c\tau$ is calculated using the known mass (m) together with the momentum (p_z) and flight length (l_z) components in the z axis as

$$c\tau = m\frac{l_z}{p_z}, \tag{6.1}$$

and its distributions (Figures 6.9 and 6.10) show that MC2010 reconstructs and selects more long-lived V^0-decays than DATA2010, and vice versa for short-lived V^0-decays. This is an effect of the resolution difference, since it is correlated with flight length. In addition, this discrepancy is already taken into account by the correction factor $\hat{k}$.

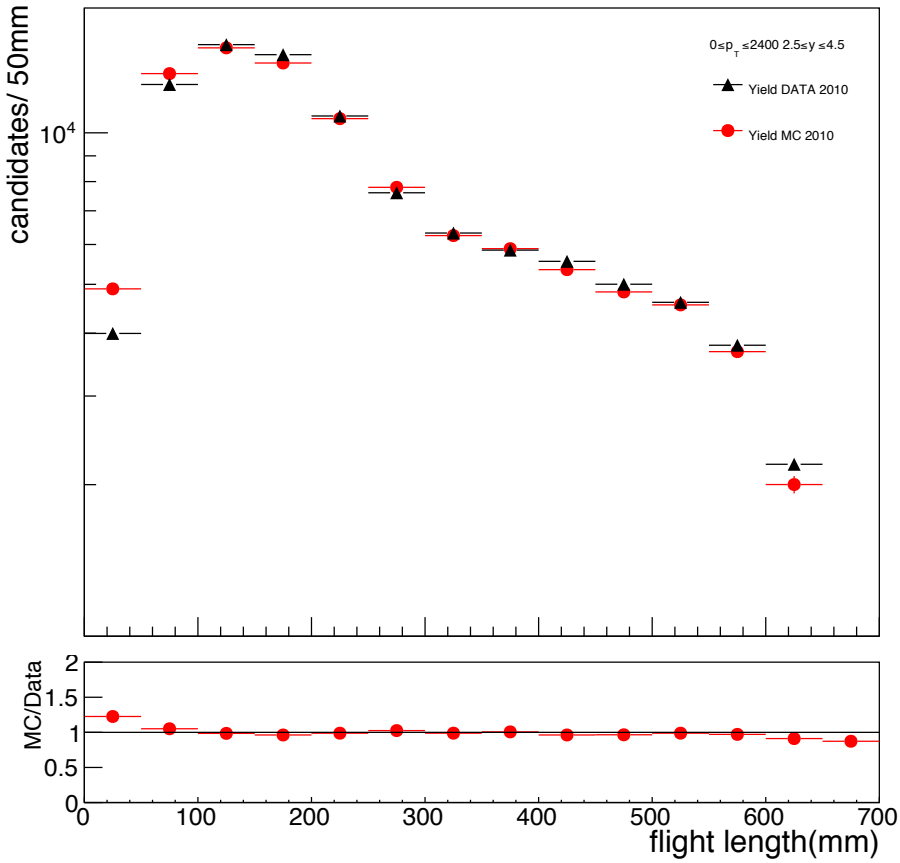

Figure 6.6: Observed flight length distribution of reconstructed and selected K^0_s-decays on DATA2010 (black filled circles) and MC2010 (red filled circles). MC2010 is normalized to match DATA2010 statistics.

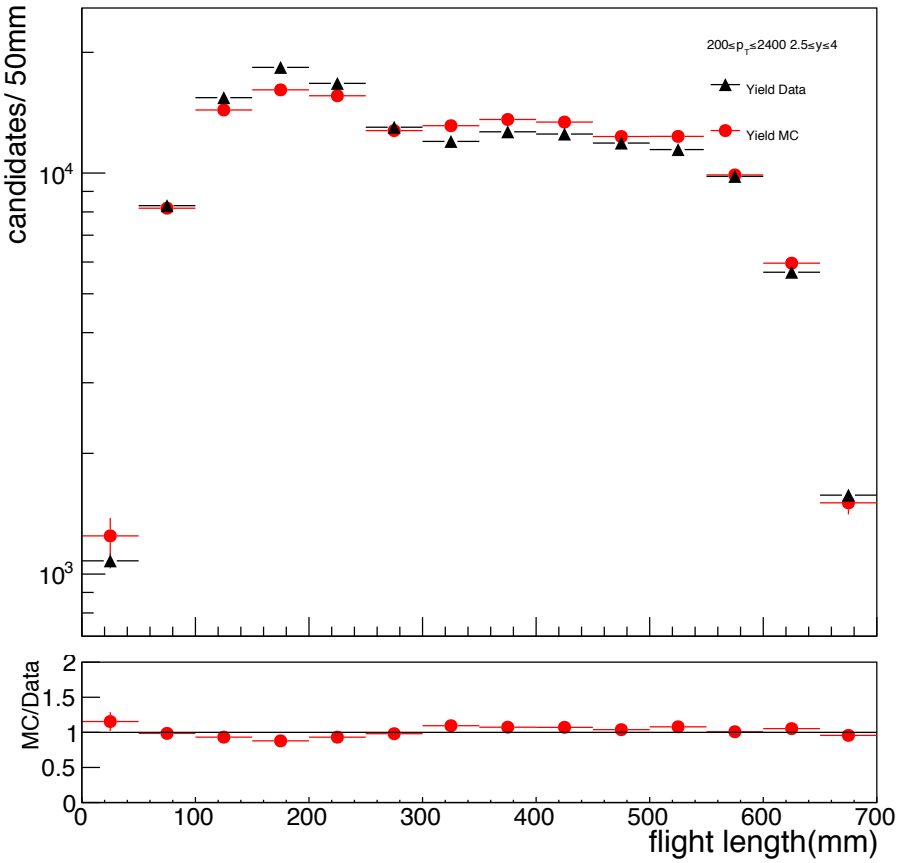

Figure 6.7: Observed flight length distribution of reconstructed and selected Λ and $\overline{\Lambda}$-decays on DATA2010 (black filled circles) and MC2010 (red filled circles). MC2010 is normalized to match DATA2010 statistics.

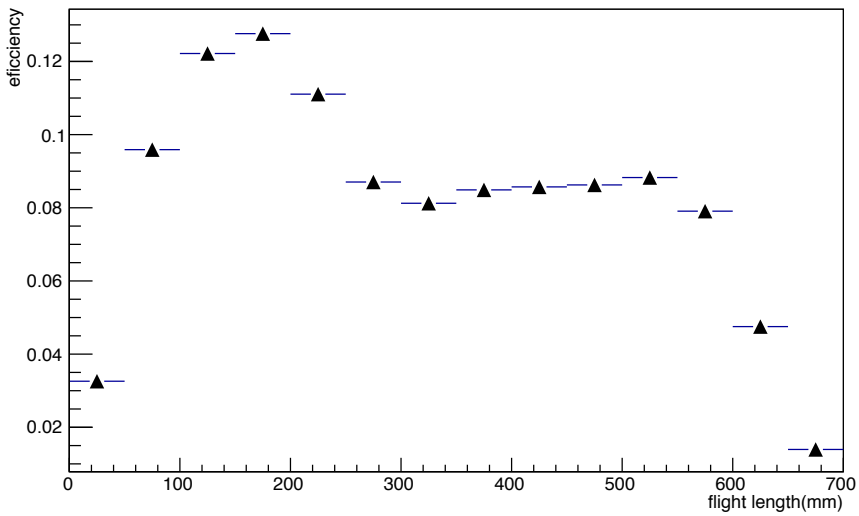

Figure 6.8: Observed efficiency in flight length bin distribution. The double structure due to the detector module setup is present.

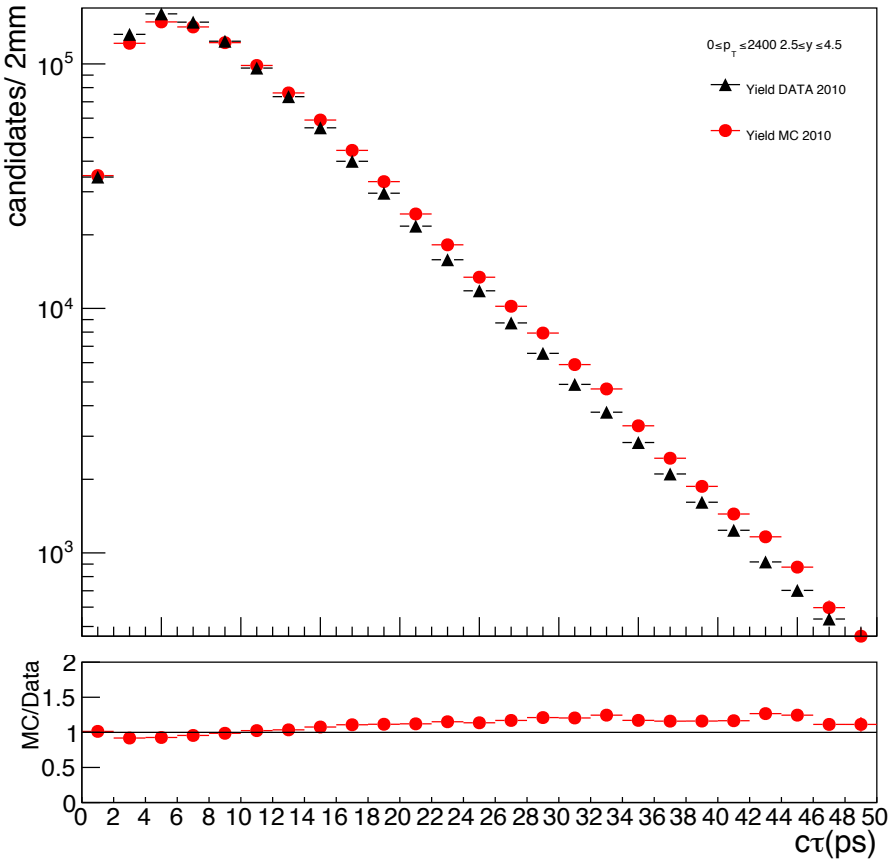

Figure 6.9: Observed $c\tau$ distribution of reconstructed and selected K^0_s-decays on DATA2010 (black filled circles) and MC2010 (red filled circles). MC2010 is normalized to match DATA2010 statistics.

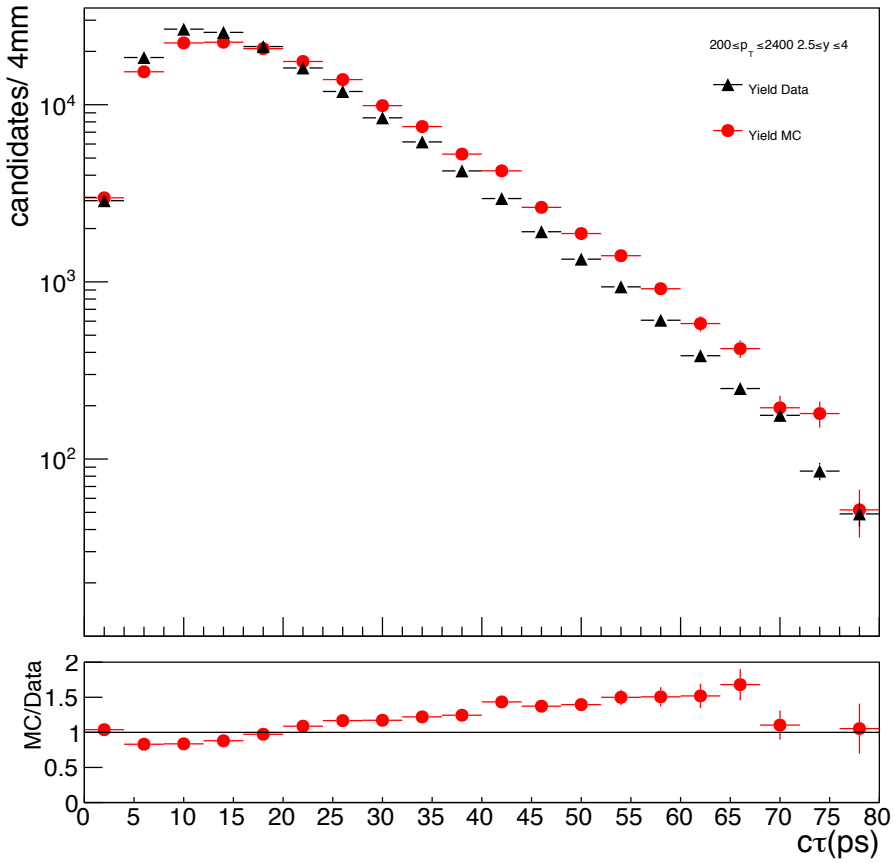

Figure 6.10: Observed $c\tau$ distribution of reconstructed and selected Λ and $\overline{\Lambda}$-decays on DATA2010 (black filled circles) and MC2010 (red filled circles). MC2010 is normalized to match DATA2010 statistics.

Chapter 7

Systematics

Relevant observed systematic uncertainties are classified in Table 7.1 as either global, for those which are taken homogeneously for every bin, or as local, for those where a phase space dependence was observed, making it necessary to estimate bin by bin. The total global uncertainties add up to 7.83% for K_s^0 and 8.26% for Λ, $\overline{\Lambda}$, respectively. In general, the precision in the measurement of systematic uncertainties is limited for the low occupancy bins, where large statistical uncertainties dominate.

Table 7.1: V^0 systematic uncertainties

Source	Local	Global
- Selection	2-10 %	
- Background subtraction	0.1-28 %	
- Efficiencies (magnet configuration)	0-14 %	
- Binning (generator dependence)	0-20 %	
- Luminosity		3.5 %
- Track efficiency		6 %
- Diffraction		2 %
- Selection efficiency ($\hat{k}$ correction)		3, 4%

7.1 Yield extraction

The yield extraction method described in Section 4.3.1 was tested on MC2010 to determine if it properly counts the number of reconstructed V^0-decays after selection. For this purpose, the double-binned p_T and y distributions obtained by background subtracted yields are compared with the true MC associated particles. As a first attempt, the K^0_s-decays, in Figure 7.1 and 7.2 show good agreement between yields and the true MC, meaning that the yield extraction method is reliable. Λ and $\overline{\Lambda}$ (Figures 7.3 and 7.4) show a small discrepancy in the central y region. Uncertainties due to background subtraction were estimated by measuring and comparing the reference cross-sections (which use background subtracted yields for efficiency estimation) against cross-sections estimated using MC true particles for efficiency estimation. There is a strong phase space dependence in this uncertainty, which is to be expected, since there are different background contributions associated with many phase space regions. Systematic uncertainties due to background subtraction are listed in Tables A.19, A.20, and A.21 for K^0_s, Λ, and $\overline{\Lambda}$-decays, respectively.

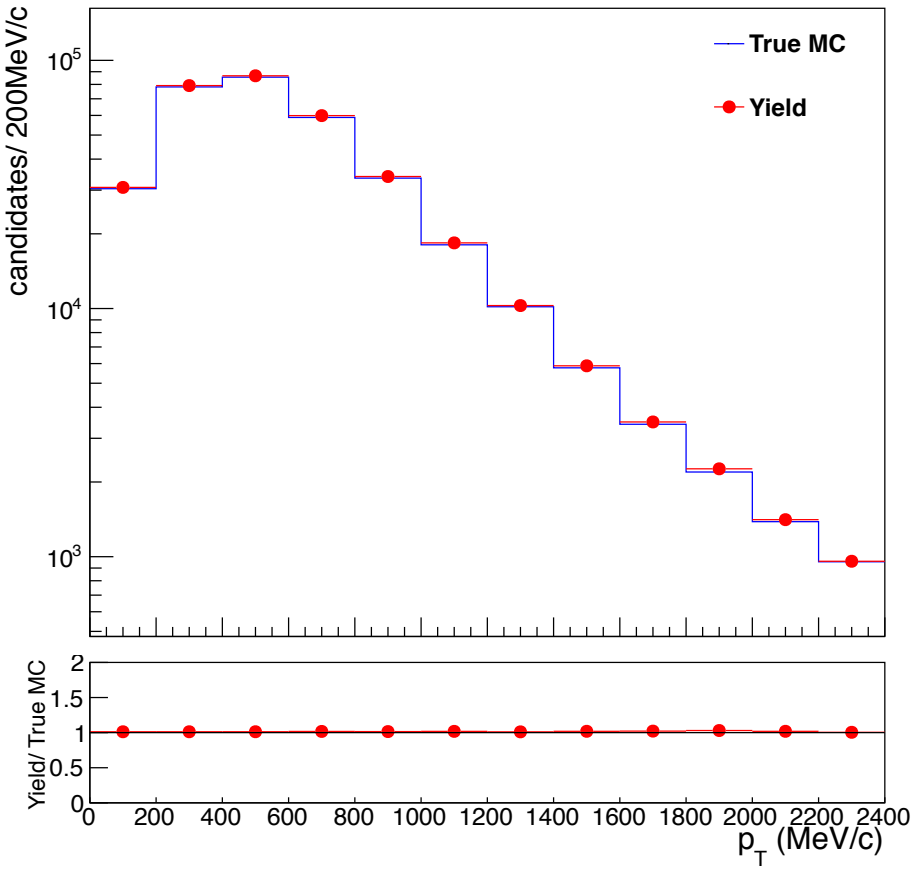

Figure 7.1: Reconstructed and selected K^0_s-decays in bins of p_T for MC2010, measured via background subtracted yields (red filled circles), and true MC (solid blue histogram).

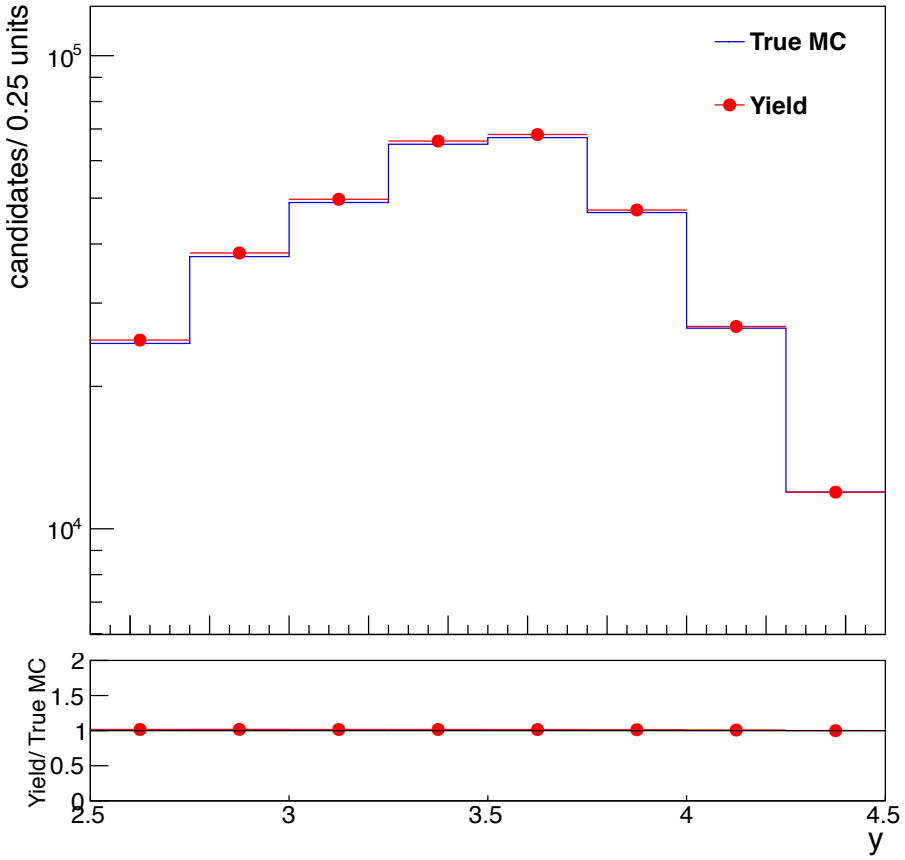

Figure 7.2: Reconstructed and selected K^0_s-decays in bins of y for MC2010, measured via background subtracted yields (red filled circles), and true MC (solid blue histogram).

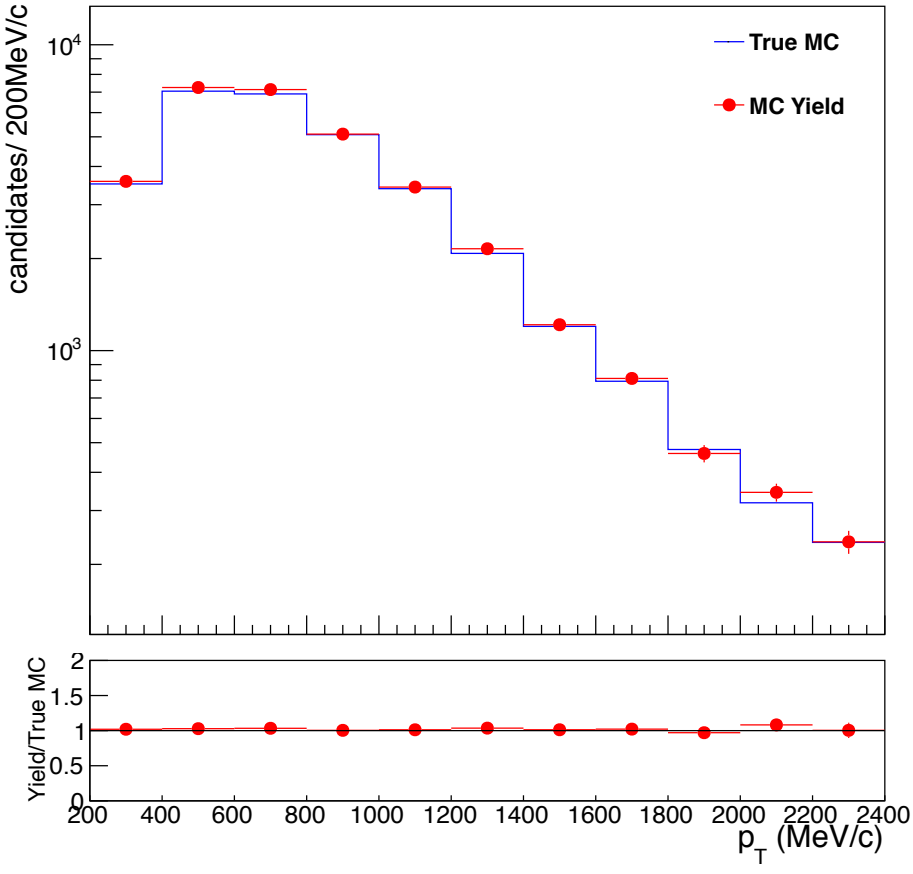

Figure 7.3: Reconstructed and selected K^0_s-decays in bins of p_T for MC2010, measured via background subtracted yields (red filled circles), and true MC (solid blue histogram).

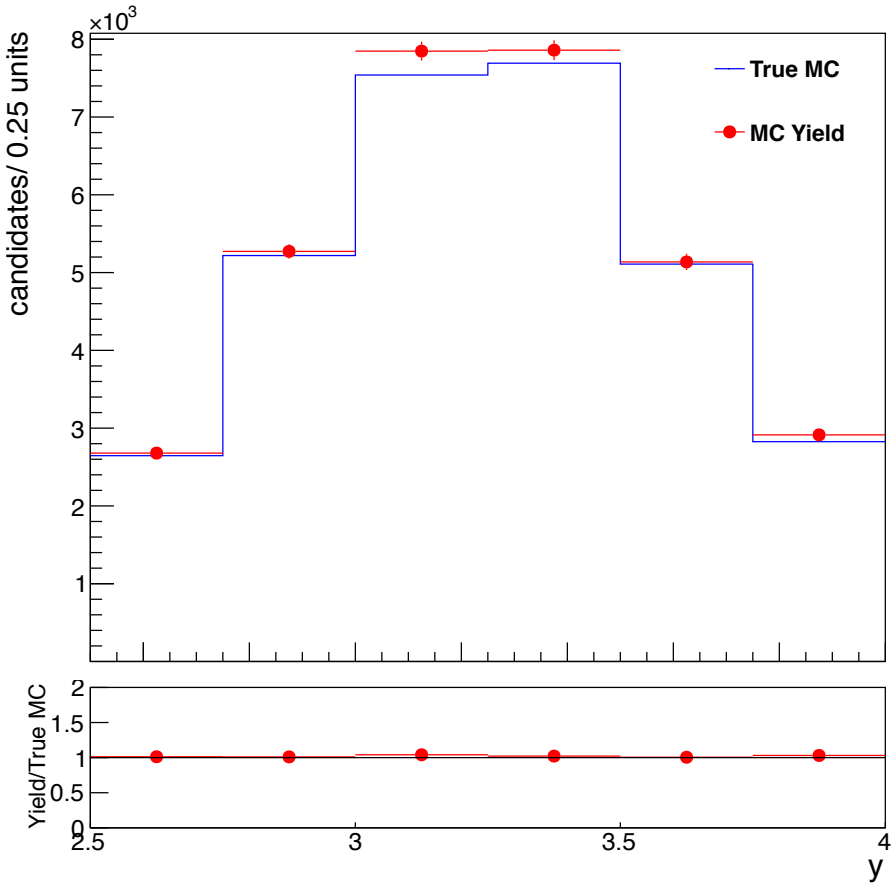

Figure 7.4: Reconstructed and selected K^0_s-decays in bins of y for MC2010, measured via background subtracted yields (red filled circles), and true MC (solid blue histogram).

7.2 Non-prompt and diffractive contributions

Another possible systematic uncertainty is the mismodelling of diffraction in the simulated data. MC studies were performed to estimate the contribution due to diffractive interactions and non-prompt V^0's, which are defined in the analysis as follows:
In diffractive processes no internal quantum numbers are exchanged between the colliding protons. A color singlet pomeron (IP) with vacuum quantum numbers mediates the interaction [37]. The diffractive contributions in this analysis are estimated in the simulated data for V^0's coming from single diffractive and double diffractive interactions (Figure 7.5). In single diffractive processes only one of the colliding protons dissociates via a pomeron ($p_1 + p_2 \rightarrow p_1' + \mathrm{X}$ and $p_1 + p_2 \rightarrow \mathrm{X} + p_2'$) [38]. If both of the protons dissociate, then the process is double diffractive ($p_1 + p_2 \rightarrow \mathrm{X}_1 + X_2$).

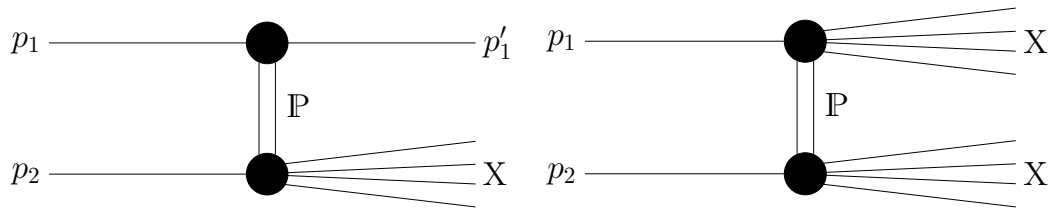

(a) Single diffractive (b) Double diffractive

Figure 7.5: Diffractive interaction diagrams.

Non-prompt V^0's include in their decay chain from the p-p interaction particles with a mean lifetime (τ) greater than 10^{-10}s. Most of the products from these particles are Λ and $\overline{\Lambda}$. Table 7.2 enumerates the particles (and all their related antiparticles) found in the PYTHIA list which meet such a requirement. Figure 7.6(a) and 7.6(b) show the contributions of diffractive events as well as non-prompts versus their transverse momentum for K_s^0 and Λ, $\overline{\Lambda}$-decays, respectively. It is clear that diffractive and non-prompt events are located in the low p_T region. Non-prompt contamination is not significant for two reasons: Firstly, the reconstruction and selection efficiencies ϵ^{sel} already take into account this factor, since they are calculated for non-prompt V^0-decays. Secondly, the selection applied implies strong pointing cuts to the primary interaction vertex, so it is robust against non-prompt contamination.

Table 7.2: Long-Lived Progenitors of Λ's

Particle	PDGID	τ(s)
Ξ^0	3322	2.90×10^{-10}
Ξ^-	3312	1.64×10^{-10}
Σ^-	3112	1.48×10^{-10}
Ω^-	3334	8.21×10^{-11}
Σ^+	3222	8.02×10^{-11}

The systematic uncertainty due to the modelling of diffractive contributions is found to be smaller than 2%. This approach is conservative since it is still model dependent, so no further effort is made to quantize bin by bin.

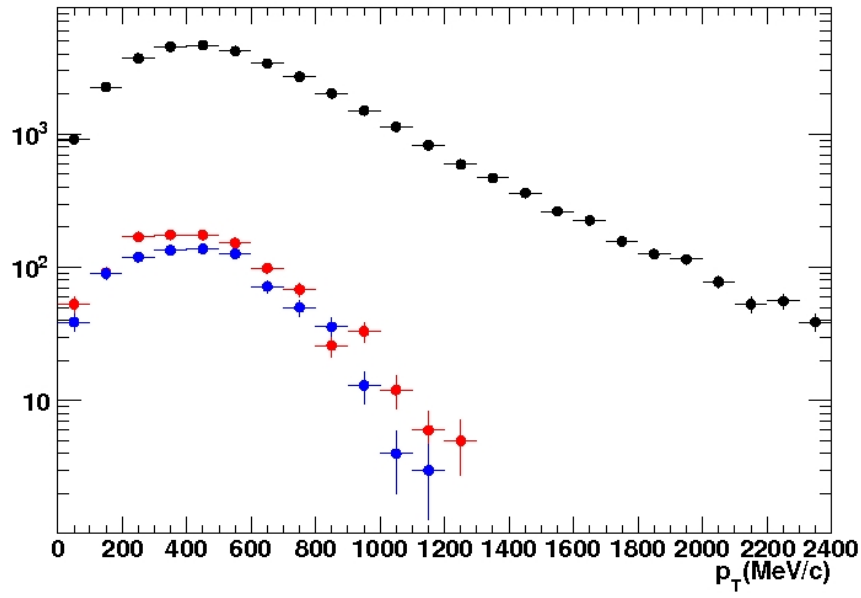

(a) K_s^0

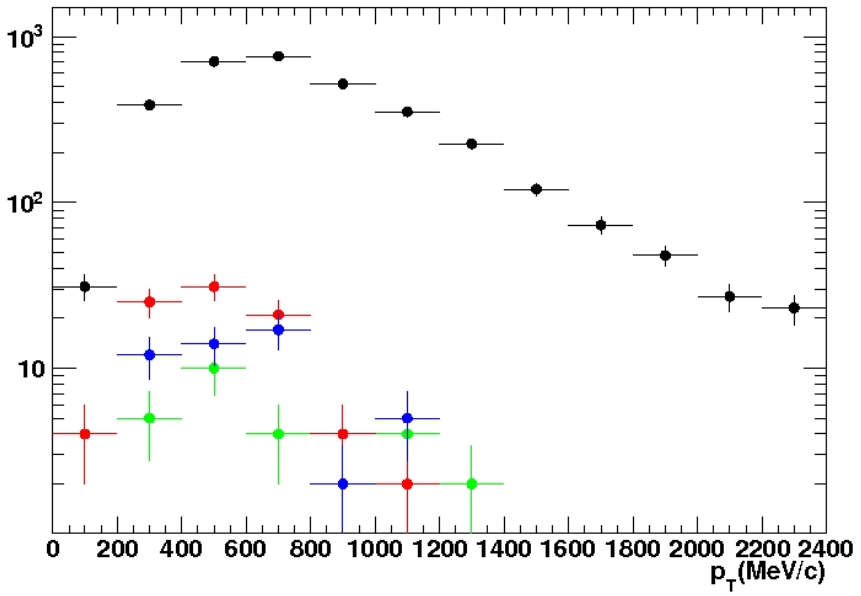

(b) Λ and $\overline{\Lambda}$

Figure 7.6: Transverse momentum p_T distribution of V^0's after selection (black filled circles) showing single diffractive (red filled circles), double diffractive (blue filled circles), and non-prompt contamination (green filled circles) for MC2010.

7.3 Binning and generator dependence

Since it was observed that various distributions for MC2010 do not match DATA2010 (Chapter 6), simulated detector efficiencies were checked carefully. Possible variations in reconstruction and selection efficiency within a certain bin of phase space are caused by the MC generator spectrum within the bin. These variations were studied by repeating the analysis, dividing each bin into four sub-bins of size Δy = 0.25 and Δp_T = 0.05 GeV/c for K^0_s-decays and Δy = 0.25 and Δp_T = 0.1 GeV/c for Λ and $\overline{\Lambda}$-decays, adding up the efficiency corrected yields, and comparing the results to those of the original binning. Good agreement was found between both binnings. Tables A.22, A.23, and A.24 show the observed differences in % for K^0_s, Λ, and $\overline{\Lambda}$-decays.

7.4 Magnet Down/Up asymmetries

Studies were performed to determine how the reconstruction efficiency of V^0-decays is affected by the detector geometry. For this task, the P_Y vs P_X distributions for the reconstructed V^0-decays were analyzed. For K^0_s-decays, P_Y vs P_X distributions show no apparent asymmetry between both magnet polarities (Figure 7.7(a) and 7.7(b)). However, for Λ and $\overline{\Lambda}$-decays there is a clear difference. When the magnet polarity is in the -y direction (Magnet Down), most of the Λ-decays are reconstructed on the left side of the detector, leaving the right side almost empty 7.8(a). For $\overline{\Lambda}$-decays we have the exact opposite case (Figure 7.8(b)). This is because for Λ-decays the pion is much softer than the proton (as seen in Figure B.1), and because it has a negative charge the magnetic field bends it strongly in the -x direction, taking it out of the detector's acceptance. For $\overline{\Lambda}$-decays the soft daughter is the positively charged pion. In this case the magnetic field bends the pion in the +x direction, so that pions coming from $\overline{\Lambda}$-decays with $p_X > 0$ fall out of the detector's acceptance. For the inverse magnet polarity (Magnet Up), we have the inverse situation, i.e., Λ-decays are mostly reconstructed on the right side and $\overline{\Lambda}$-decays on the left side (Figures 7.9(a) and 7.9(a)). For this polarity (B Field in the + y direction) the soft

negative pions from Λ-decays are bent in the +x direction, and the opposite holds for the soft positive pions from $\overline{\Lambda}$-decays. Final cross-sections are obtained using an unweighted average for both magnet polarities to cancel out any possible effects on the efficiency that may arise from the detector geometry. Combining the results for both magnet polarities, the distribution is fairly symmetric for all V^0-decays, as observed in Figures 7.11(a), 7.11(b), and 7.10.

Finally, the small difference in efficiency between the magnet polarities is taken into account as a systematic uncertainty for every p_T,y bin. Tables A.25, A.26, and A.27 show the measured uncertainties due to reconstruction efficiencies for opposite magnet polarities for K^0_s, Λ, and $\overline{\Lambda}$-decays, respectively.

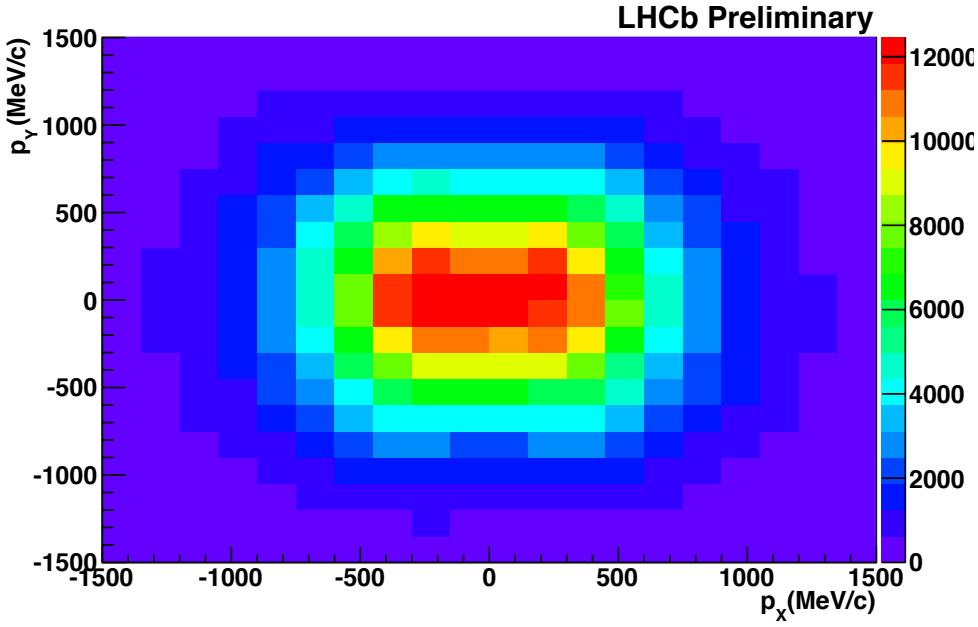

(a) Magnet Down

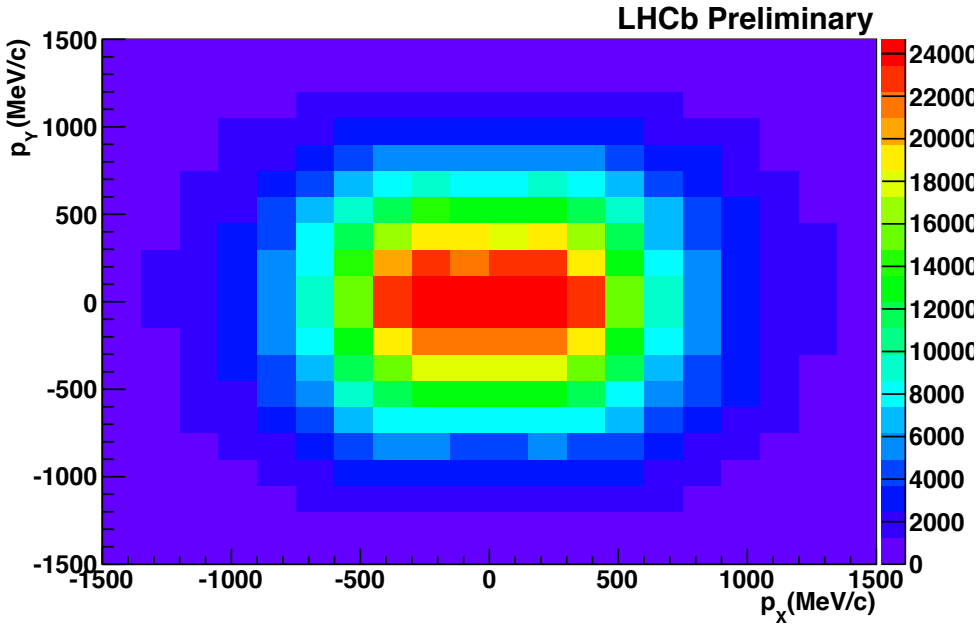

(b) Magnet Up

Figure 7.7: p_Y vs p_X distributions for reconstructed K^0_s candidates after selection from DATA2010.

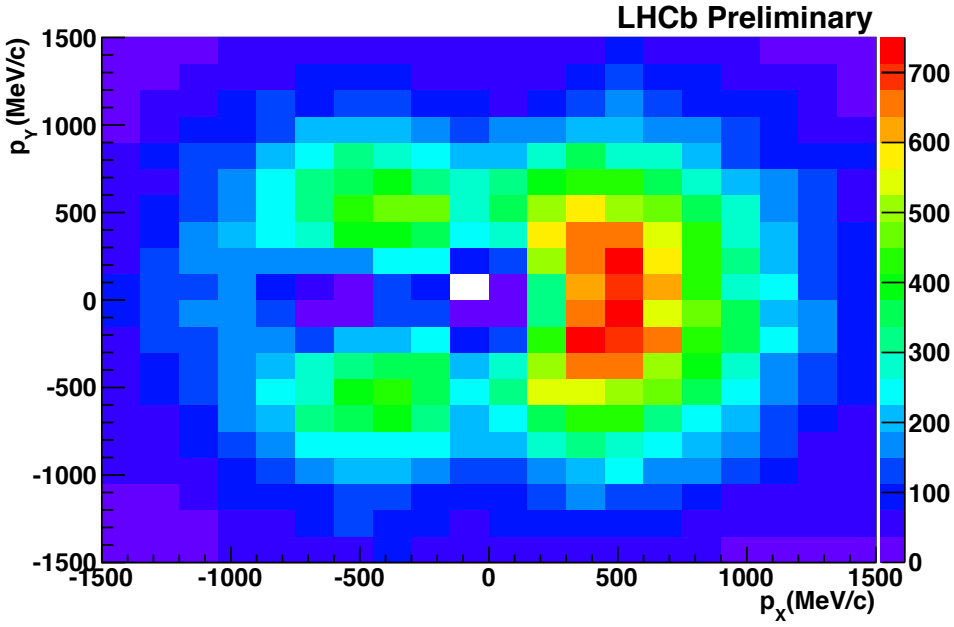

(a) Λ-decays

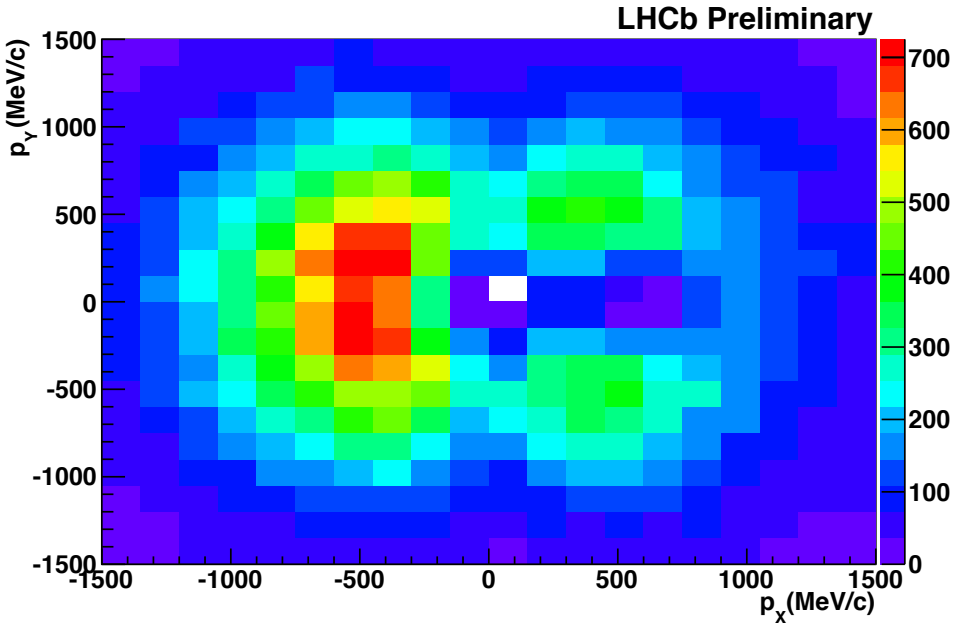

(b) $\overline{\Lambda}$-decays

Figure 7.8: p_Y vs p_X distributions for reconstructed Λ, $\overline{\Lambda}$-decays after selection from DATA2010, for the Magnet Down case.

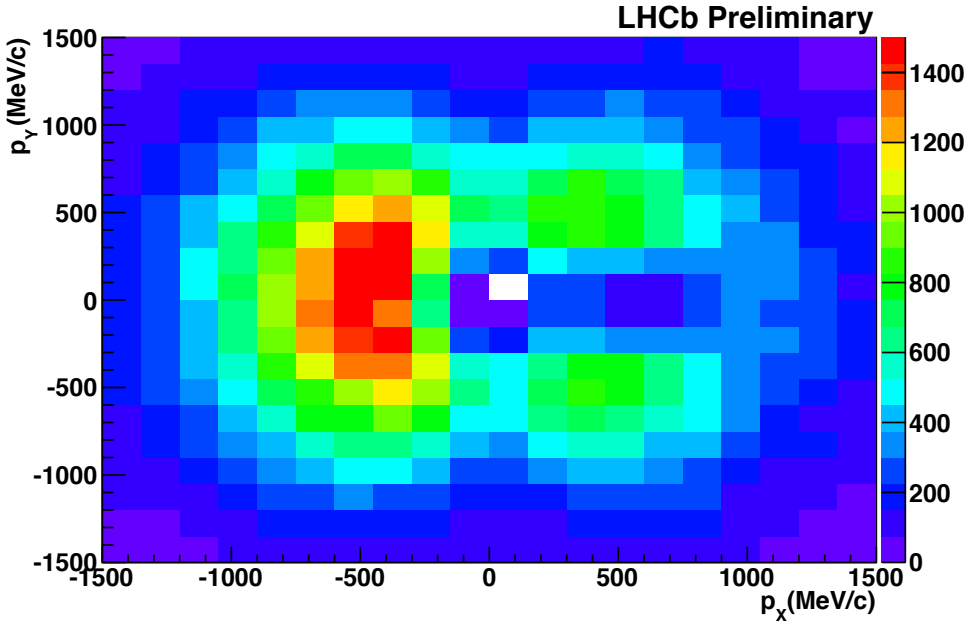

(a) Λ-decays

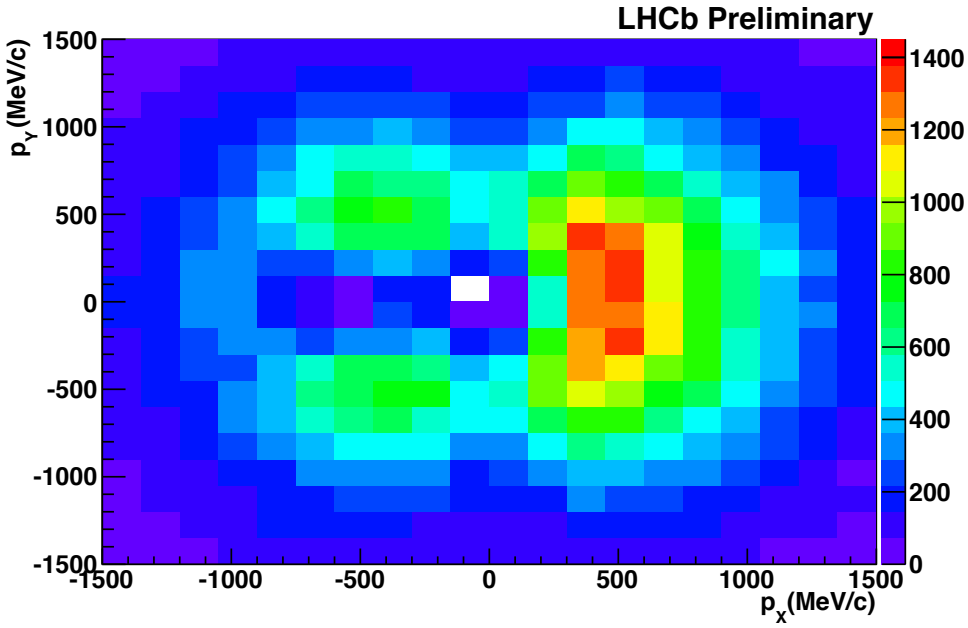

(b) $\overline{\Lambda}$-decays

Figure 7.9: p_Y vs p_X distributions for reconstructed Λ, $\overline{\Lambda}$-decays after selection from DATA2010, for the Magnet Up case.

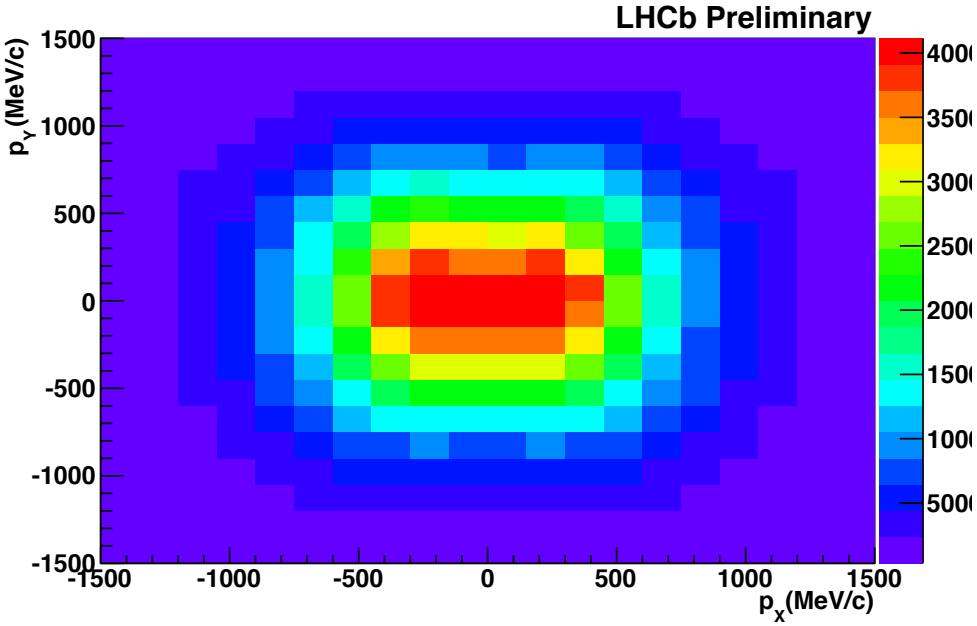

Figure 7.10: p_Y vs p_X distributions for reconstructed K^0_s-decays after selection from DATA2010, combining Magnet Down and Up results.

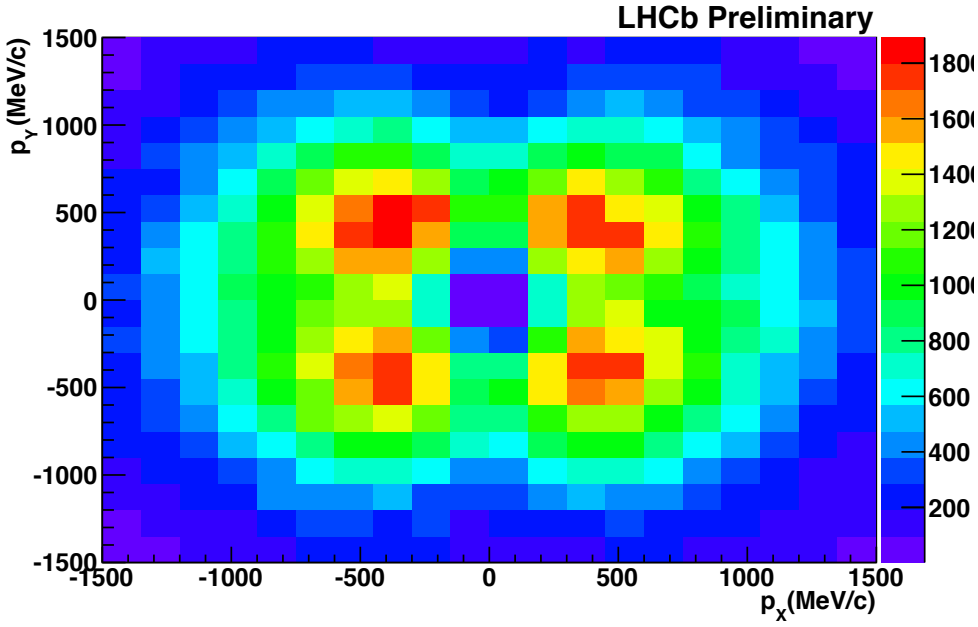

(a) Λ-decays

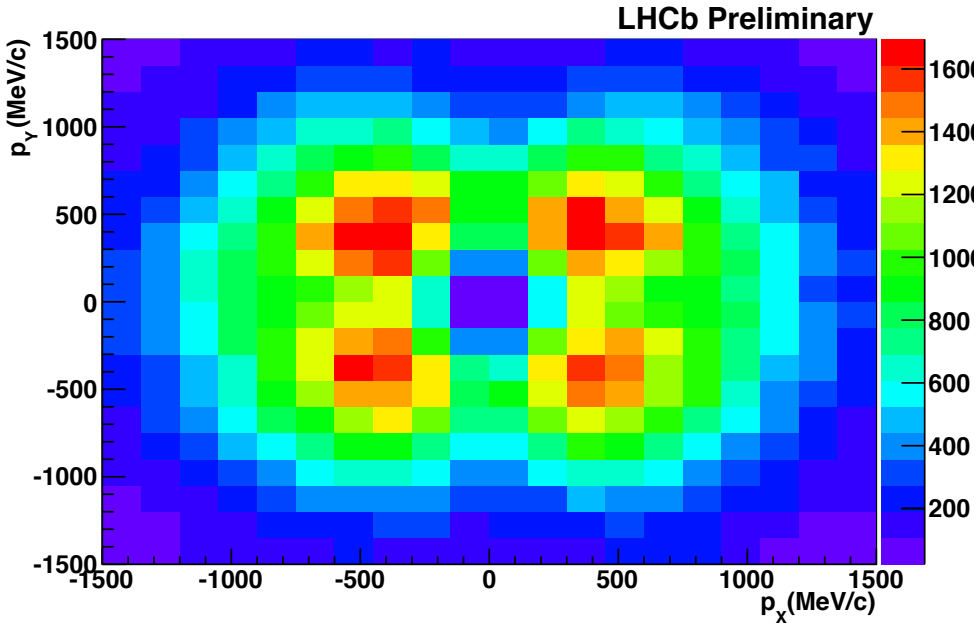

(b) $\overline{\Lambda}$-decays

Figure 7.11: p_Y vs p_X distributions for reconstructed Λ, $\overline{\Lambda}$-decays after selection from DATA2010, combining Magnet Down and Up results.

Chapter 8

Results

8.1 Measured yields

As a first step to estimate the cross-sections defined in Eq 4.2, the signal yields were measured for DATA2010 and MC2010. This was done separately for each magnet polarity. Figure 8.7 shows the measured K_s^0 yields in bins of p_T, showing consistency between Magnet Down and Magnet Up results for both DATA2010 and MC2010. In the case of K_s^0-decays, despite the yield underestimation in 2010 in the high p_T bins, we are still provided with enough statistics to measure the efficiencies with good accuracy. For Λ and $\overline{\Lambda}$, there is an observable, but not significant difference between magnet polarities (Figures 8.2, 8.3) in DATA2010. For MC2010, the discrepancy in the high p_T bins is large, but still covered by statistical uncertainties. These bins suffer from low statistics, since the p_T spectrum in MC2010 is softer and has a smaller sample size compared to DATA2010.

Numerical results are shown in Tables A.1, A.2, A.3, A.4, A.5, and A.6. For all V^0-decays, the numbers show no apparent inconsistency between the magnet polarities, and the event counts seem to be approximately double for Magnet Up with respect to Magnet Down. This is expected, since the sample used for Magnet Up had twice the luminosity of the one used for Magnet Down, and the efficiencies are approximately the same.

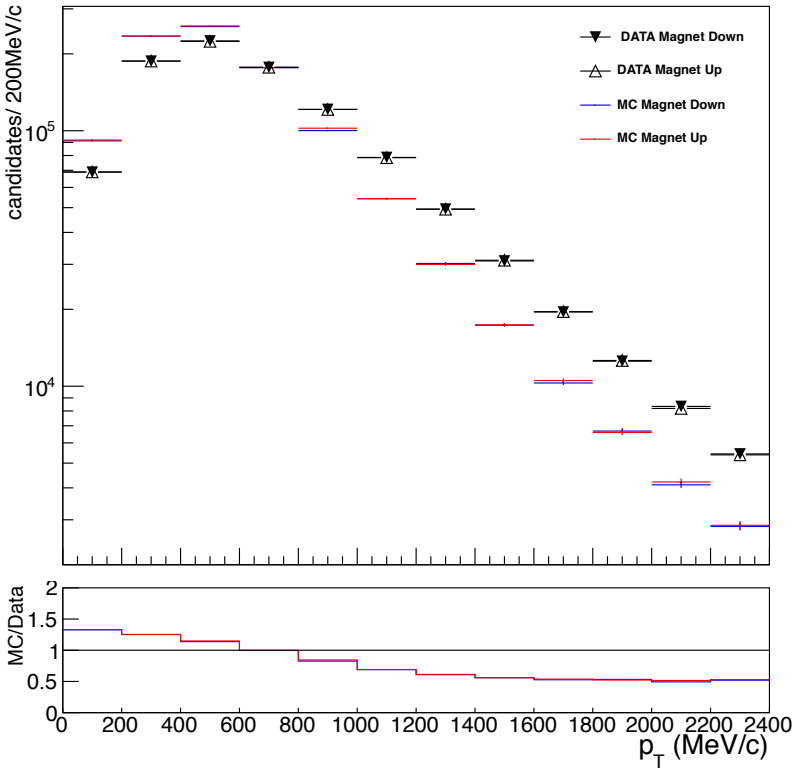

Figure 8.1: Measured K^0_s yields in bins of p_T (y integrated). Triangles are measurements done on DATA2010 for Magnet Down and Up polarities (black filled and black hollow triangles). In blue and red the same measurements for MC2010 are shown. The distributions are normalized to the same area as the data. Error bars are statistical uncertainties.

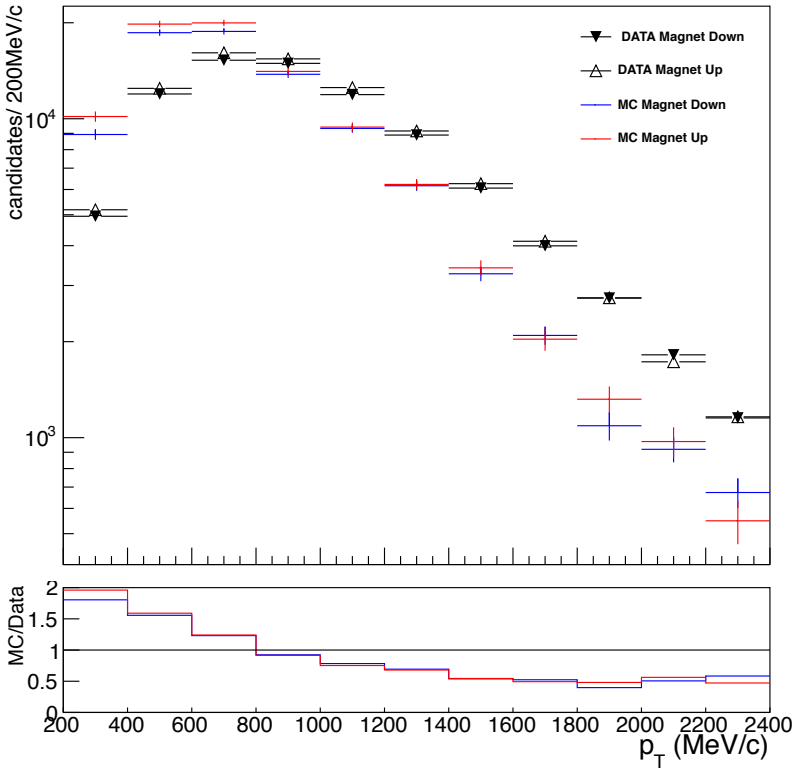

Figure 8.2: Measured Λ yields in bins of p_T (y integrated). Triangles are measurements done on DATA2010 for Magnet Down and Up polarities (black filled and black hollow triangles). In blue and red the same measurements for MC2010 are shown. The distributions are normalized to the same area as the data. Error bars are statistical uncertainties.

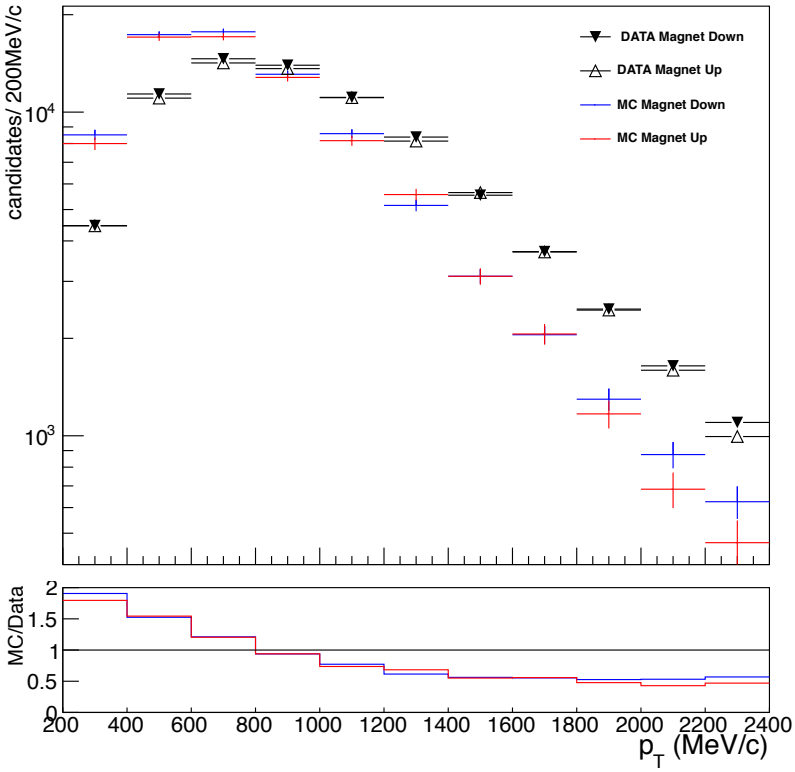

Figure 8.3: Measured $\overline{\Lambda}$yields in bins of p_T (y integrated). Triangles are measurements done on DATA2010 for Magnet Down and Up polarities (black filled and black hollow triangles). In blue and red the same measurements for MC2010 are shown. The distributions are normalized to the same area as the data. Error bars are statistical uncertainties.

8.2 Observed efficiencies

The efficiencies described in Subsection 4.3.2 were determined for MC2010 for the respective measured phase space regions for K_s^0-decays ($0 \leq p_T \leq 2.4$ GeV/c, $2.5 \leq$ y ≤ 4.5) and Λ, $\overline{\Lambda}$-decays ($0.2 \leq p_T \leq 2.4$ GeV/c, $2.5 \leq$ y ≤ 4.0). MC2010 was produced using PYTHIA 6.4 [39] as a generator to model high energy pp collisions, where the particles produced are propagated afterwards, modelling the interactions throughout the detector using GEANT 4 [40]. Inconsistencies between MC2010 and DATA2010 were measured and the correction factor $\hat{k}$ defined in Eq 5.6 was applied uniformly to all measured efficiencies for cross-section measurements.

Figures 8.4(a) and 8.4(b) show a 2-D map of K_s^0 corrected ($\hat{k}$) selection efficiencies in bins of p_T-y. The phase space region in which the detector offers the highest efficiency (8-10%) is $300 \leq p_T \leq 1200$MeV/c and $3 \leq$ y ≤ 4. The structure in y is due to the detector geometry since we require long tracks, and in this rapidity region tracks traverse the most active material. The decrease in efficiency at high p_T is due to the long lifetime of V^0 particles. High momentum V^0 particles travel long distances before decaying, so that they are not seen in the VELO detector. For Λ and $\overline{\Lambda}$ (Figure 8.5(a), 8.5(b), 8.6(a), and 8.6(b)) the highest efficiencies are observed (8-10%) in the bins with $600 \leq p_T \leq 1400$MeV/c and $3 \leq y \leq 4$. The low efficiencies for low p_T and at high and low y are due to the wide opening angle present in Λ and $\overline{\Lambda}$-decays.

Estimates of selection efficiencies are shown in Tables A.7, A.8, A.9, A.10 , A.11, and A.12 for K_s^0 , Λ, and $\overline{\Lambda}$ for both magnet polarities. The efficiencies are around $2 \leq \epsilon_{i,j}^{sel} \leq 11\%$ for K_s^0-decays and $2 \leq \epsilon_{i,j}^{sel} \leq 10\%$ for Λ and $\overline{\Lambda}$-decays.

No significant difference in efficiency was found between magnet polarities. Nevertheless, the unweighted average cross-section measurement is performed to cancel any systematic effects due to magnet polarity.

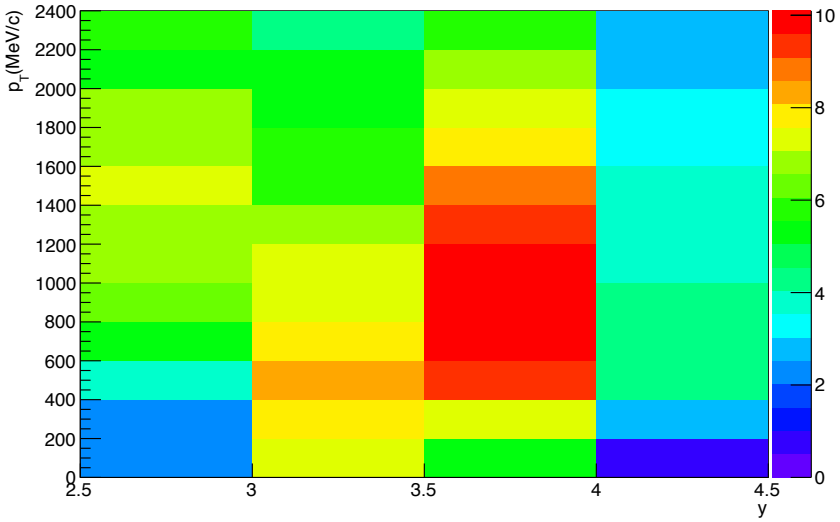

(a) Magnet Down

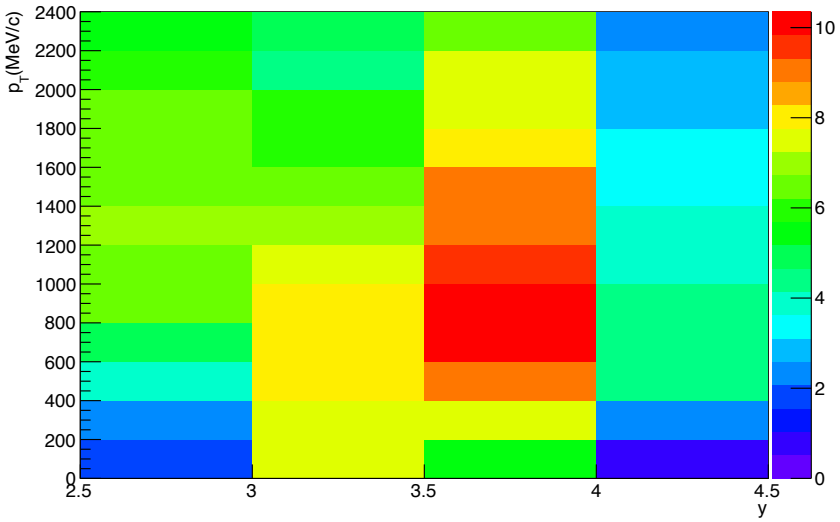

(b) Magnet Up

Figure 8.4: Reconstruction and selection efficiencies ϵ^{sel} for K^0_s-decays measured for MC2010, p_T vs y profile.

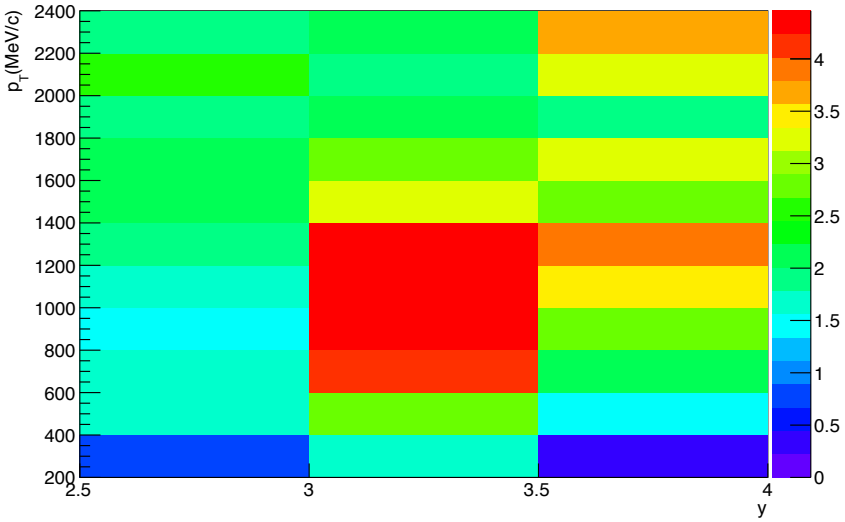

(a) Magnet Down

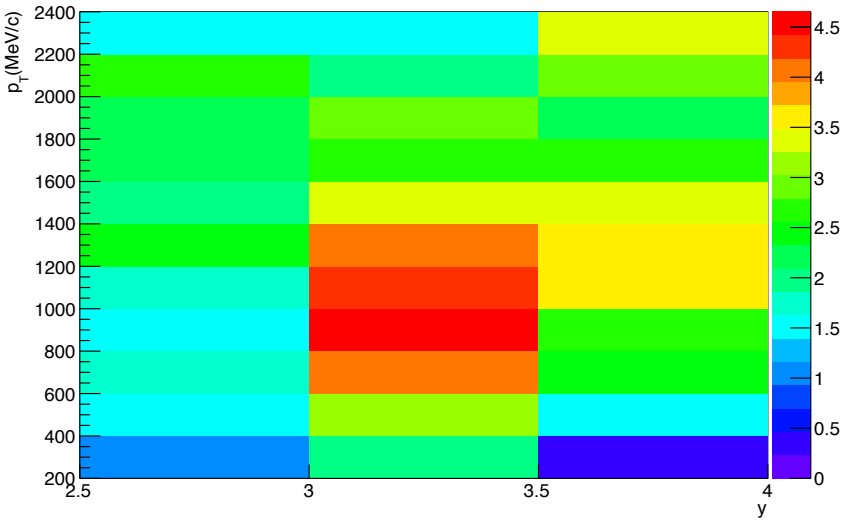

(b) Magnet Up

Figure 8.5: Reconstruction and selection efficiencies ϵ^{sel} for Λ-decays measured for MC2010, p_T vs y profile.

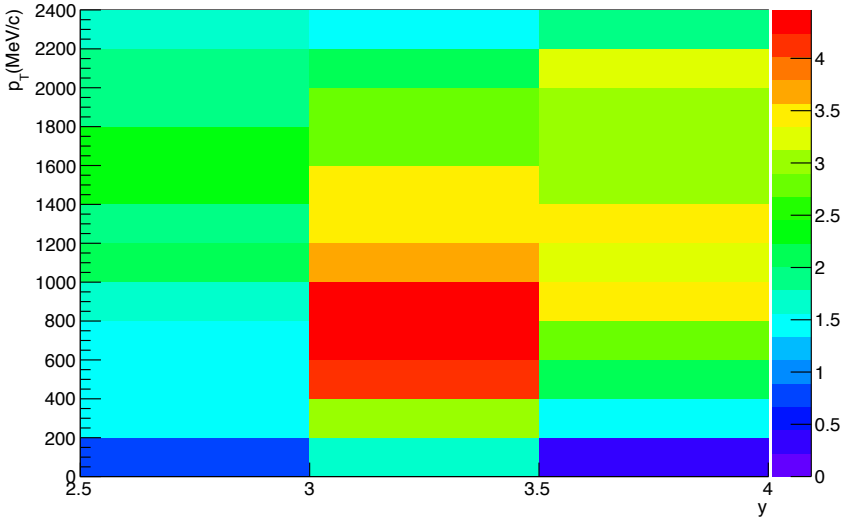

(a) Magnet Down

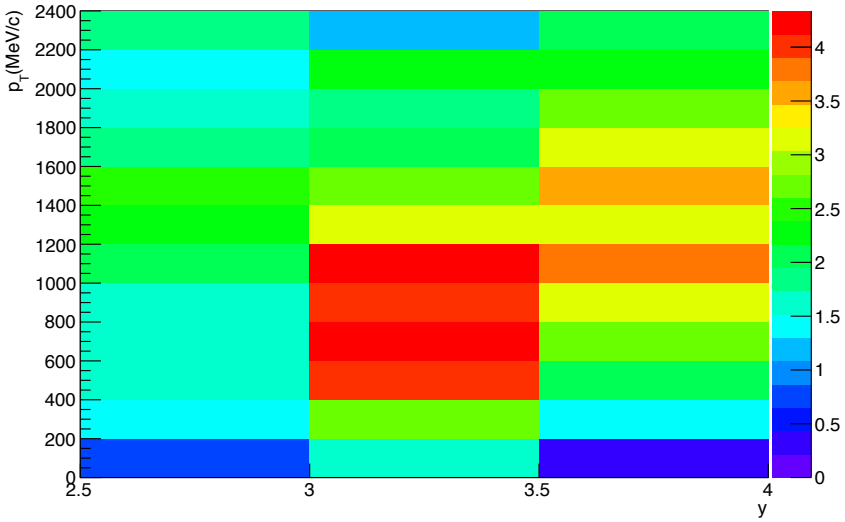

(b) Magnet Up

Figure 8.6: Reconstruction and selection efficiencies ϵ^{sel} for $\overline{\Lambda}$-decays measured for MC2010, p_T vs y profile.

8.3 Cross-sections

The measured cross-sections show good consistency for both polarities, as is illustrated in Figures 8.7, 8.12, and 8.9. From this it is understood that the differences seen between both magnet polarities are accounted for by the simulation.

The predictions performed by the MC generator, based on PYTHIA 6.4 [39] which includes only soft diffraction and p_T-spectra extrapolated from 1 TeV data, largely underestimate the measured cross-sections at high p_T. Predictions from PYTHIA 8 [20], which includes both soft and hard diffraction and early LHC data p_T calibration, show better agreement with DATA2010 for the high p_T tail. Nevertheless, both generators overestimate the measured Λ and $\overline{\Lambda}$ production at low p_T. Tables A.13, A.14, A.15, A.16, A.17, and A.18 show the measured cross-sections for each magnet polarity. The numbers show good consistency within error, which is only statistical at this point. The high p_T bins in the Λ and $\overline{\Lambda}$-decays already show uncertainties greater than 20%, due to the limited statistics in MC2010. This also reflects a limitation in measuring systematic uncertainties for these bins (Chapter 7).

To cancel out detector asymmetry effects (Subsection 7.4), the final cross-sections are calculated by combining the results for both magnet polarities via an unweighted average, using Eq. 4.3. Relative uncertainties are summarized in Table 7.1 (discussed in Chapter 7 in detail) and are added in quadrature within each category (local and global). The final results are listed in Tables A.28, A.29, and A.30.

The final cross-sections as a function of transverse momentum are plotted, comparing the results with other prompt V^0 measurements in high energy hadron collisions. Firstly, K^0_s results for this measurement (pp at 7 TeV, $2.5 < \mathrm{y} < 4.5$) were compared with previous measurements done by UA1 ($p\bar{p}$ at 630 GeV, $-2.5 < \eta < 2.5$ [18]), UA5 ($p\bar{p}$ at 540 GeV, $-3.5 < \eta < 3.5$ [19]), and LHCb (pp at 900 GeV, $2.5 < \mathrm{y} < 4.0$ [17]). The UA1 and UA5 measurements were published in the form of invariant differential cross-sections $\mathrm{E}\frac{d^3\sigma}{d^3p}$ as a function of p_T. They were converted into measurements of $\frac{d^2\sigma}{dp_T dy}$ by multiplication with $2\pi p_T$ in order to compare them with this measurement and the previous measurement from the LHCb at 900 GeV [17]. For both LHCb cases the p_T binning is the same, and systematic uncertainties are conservatively taken to

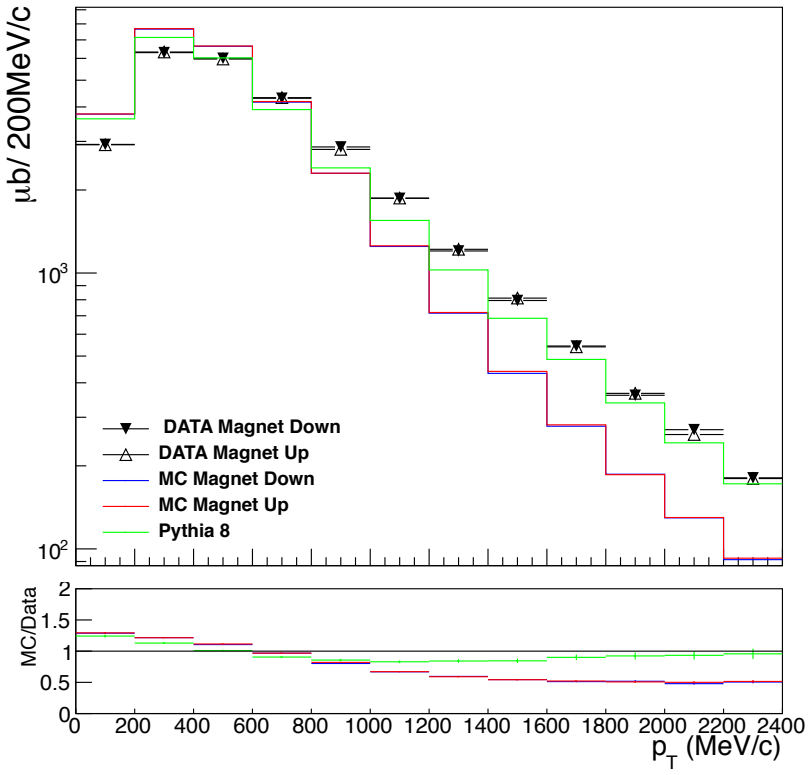

Figure 8.7: Observed K^0_s production cross-section (y integrated) in bins of p_T. Triangles are measurements done on DATA2010 for Magnet Down and Up polarities (black filled and black hollow triangles). The blue and red histograms represent the particles generated from MC2010, scaled to match the DATA2010 area. The green histograms represent the prediction by PYTHIA 8. Error bars are statistical uncertainties.

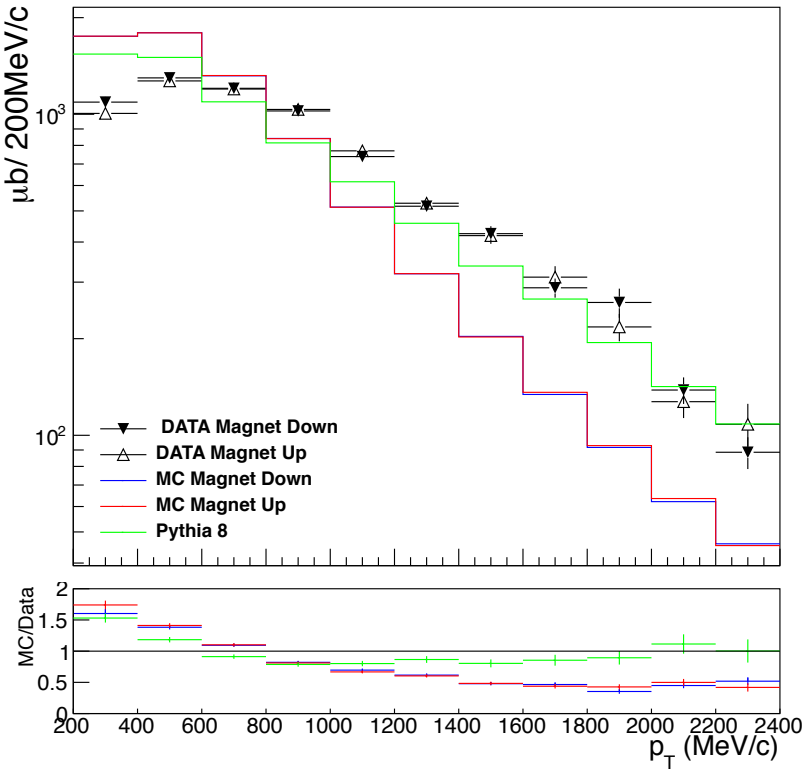

Figure 8.8: Observed Λ production cross-section (y integrated) in bins of p_T. Triangles are measurements done on DATA2010 for Magnet Down and Up polarities (black filled and black hollow triangles). The blue and red histograms represent the particles generated from MC2010, scaled to match the DATA2010 area. The green histograms represent the prediction by PYTHIA 8. Error bars are statistical uncertainties.

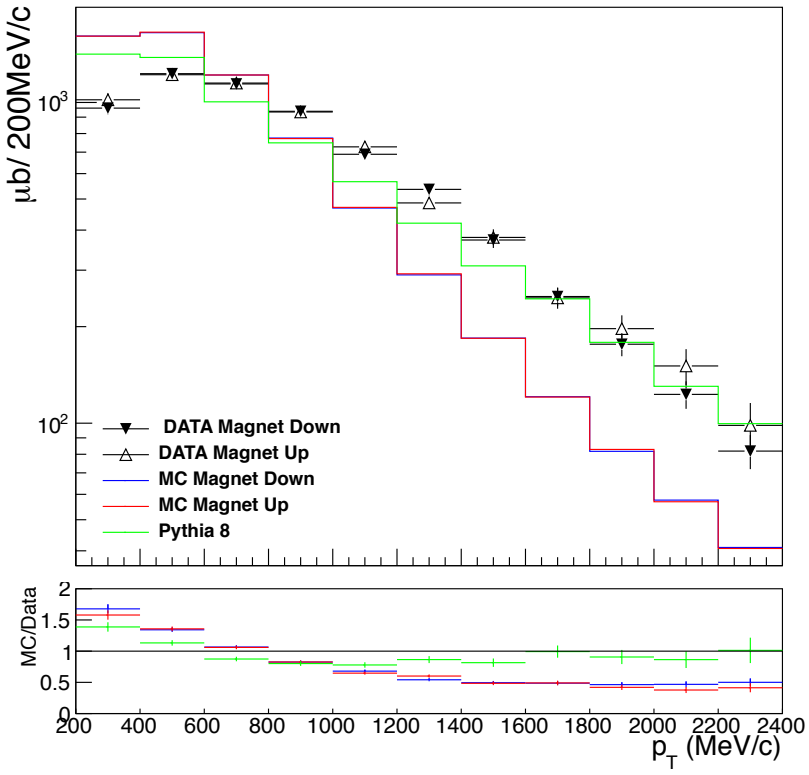

Figure 8.9: Observed $\overline{\Lambda}$ production cross-section (y integrated) bins of p_T. Triangles are measurements done on DATA2010 for Magnet Down and Up polarities (black filled and black hollow triangles). The blue and red histograms represent the particles generated from MC2010, scaled to match the DATA2010 area. The green histograms represent the prediction by PYTHIA 8. Error bars are statistical uncertainties.

be 100% correlated. Figure 8.10 shows that the observed strange meson production is around 2.5 times higher than previous low center-of-mass energy measurements. To verify this result, K_s^0 production p_T distributions were generated using PYTHIA 8 [20] for the rapidity range $2.5 \leq y \leq 4.5$, at 7 TeV and 0.9 TeV (Figure 8.11), where a similar increase in K_s^0-decay production is observed, consistent with measurement results. For Λ and $\overline{\Lambda}$, as Figure 8.12 shows, the production is compared with the results from UA1, also showing a significant increase in strange baryon production.

More comparisons were performed for V^0 production ratios with previous LHCb measurements at 7 TeV [17]; however, these are to be taken with a grain of salt, since the two measurements are sensitive to different systematic uncertainties. The results of this comparison are shown in Appendix C.

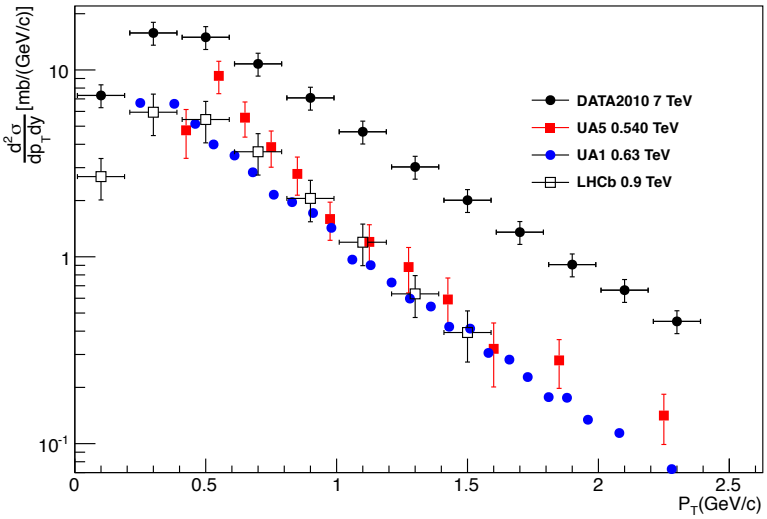

Figure 8.10: Measured prompt K_s^0 production cross-section as a function of p_T, measured on the LHCb DATA2010 (black filled circles), LHCb @0.9 TeV [17] (black hollow squares), UA1 [18] (blue filled circles), and UA5 [19] (red filled squares). Measurements were done at different cms energies on different hadron collision types and different pseudorapidity or rapidity ranges.

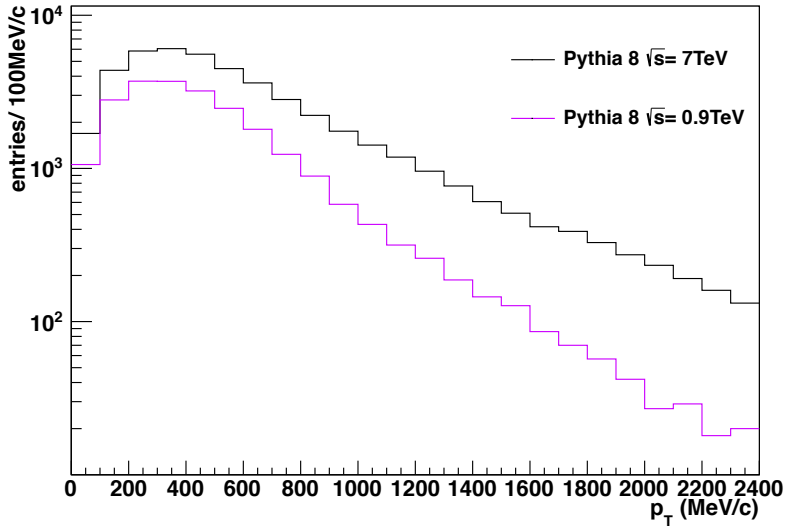

Figure 8.11: Prompt K_s^0 production prediction for the rapidity range $2.5 \leq y \leq 4.5$, for 7 TeV and 0.9 TeV pp collisions generated using PYTHIA 8 [20].

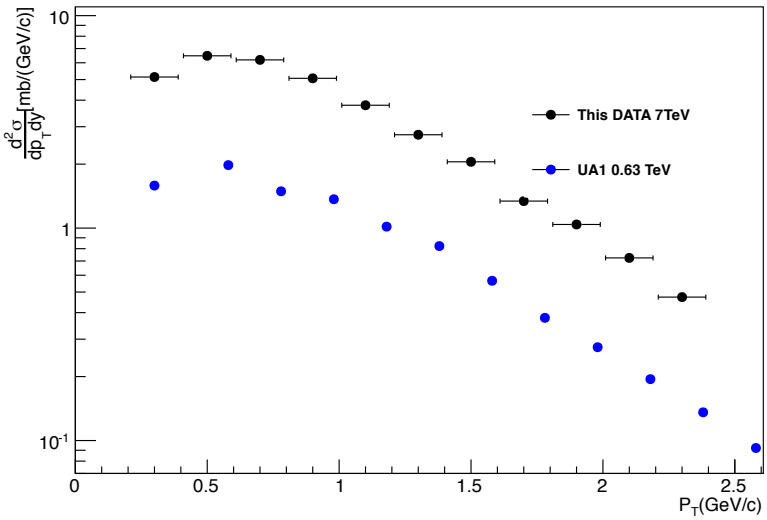

Figure 8.12: Measured prompt Λ and $\overline{\Lambda}$ production cross-section as a function of p_T, measured on the LHCb DATA2010 (black filled circles) and UA1 [18] (blue filled circles). Measurements were done at different center-of-mass energies on different hadron collision types and different pseudorapidity or rapidity ranges.

8.4 Conclusion

The production of V^0-decays from pp collisions at 7 TeV has been studied with the data collected by the LHCb detector in early 2010. A pure geometrical selection is used and applied equally to all V^0-decays. The analysis was done for two magnet polarities, and their results are combined for the final cross-section measurements. The total luminosity used for the analysis is 1.8 nb^{-1} (0.6 nb^{-1} for Magnet Down and 1.2 nb^{-1} for Magnet Up).

Uncertainties in the measurement were studied by calculating the variations due to background subtraction, differences in the reconstruction efficiency between Magnet Down and Magnet Up, and generator dependence (via binning). The most peculiar of these uncertainties are the Magnet Down-Magnet Up asymmetries, wherein it was found that Λ and $\overline{\Lambda}$-decays are reconstructed mostly on one specific side of the detector, depending on the magnet configuration. This has a small effect on the reconstruction efficiency. For this reason, the best strategy is to combine the results for both magnet polarities. From background subtraction studies it was seen that assuming a linear background accounts well for the background on Λ and $\overline{\Lambda}$-decays, and that such decays can then be analyzed without further cuts which might introduce a phase space bias.

The cross-sections were measured in bins of p_T and y in the kinematic range of $0 \leq p_T \leq 2.4$ GeV/c, $2.5 \leq$ y ≤ 4.5 for K_s^0 and $0.2 \leq p_T \leq 2.4$ GeV/c, $2.5 \leq$ y ≤ 4.0 for Λ and $\overline{\Lambda}$. Statistical errors for K_s^0-decays vary between 1 % and 5 % for low p_T, and between 7 % and 16 % for high p_T. For Λ and $\overline{\Lambda}$-decays, errors vary between 3 % and 6 % for low p_T, and between 14 % and 17 % for high p_T. Local systematic uncertainties are on the order of 6 %; however, there are large uncertainty values observed for certain bins. Firstly, to the fact that MC2010 has a very soft p_T spectra, the high p_T bins contain very few events. Secondly, at low p_T with very small or very large y, these bins provide small statistics due to detector acceptance for both DATA2010 and MC2010. The total global systematic uncertainty is 12%. In general, MC2010 has a higher resolution than DATA2010, resulting in a smaller selection efficiency for DATA2010; however, this effect was measured and taken into

account for the measurement.

Data results were compared to two generator predictions: LHCb MC (based on PYTHIA 6.4) and PYTHIA 8.1. It was found that LHCb MC does not reproduce the p_T spectra. It is too soft compared to data results. PYTHIA 8.1 predictions were more consistent with the observed spectra, proving that its configuration and calibration provides a reasonable description of meson production in pp collisions at the TeV scale. V^0 production cross-sections from this measurement showed a significant increase compared to previous low center-of-mass energy measurements. The increase was verified using PYTHIA 8.1 generator predictions.

These results can provide valuable information for generator tuning in experiments complementary to other strange mesons production measurements [41], baryon production ratios [42] [43], and previous K^0_s measurements at lower energies [17].

Appendix A

Tables

A.1 Yields

Table A.1: Number of observed K_s^0-decays on DATA 2010, Magnet Down, in bins of transverse momentum p_T and rapidity y.

p_T(MeV/c)/y	2.5 - 3.0	3.0 - 3.5	3.5 - 4.0	4.0 - 4.5
0-200	9961.5 ± 104.4	33685.5 ± 193.4	21787.5 ± 159.7	3423.5 ± 69.8
200-400	23651.5 ± 157.6	74936.5 ± 281.9	66812 ± 272.5	21904 ± 162.3
400-600	36557 ± 196.2	75865 ± 283.4	80130 ± 301.7	32117.5 ± 197.4
600-800	38738.5 ± 200.9	54701 ± 242.4	60805 ± 268.4	22815.5 ± 168.9
800-1000	31265.5 ± 180.5	35058 ± 198.3	40931 ± 225.6	13989 ± 134.5
1000-1200	22693.5 ± 154.4	21876.5 ± 160.1	25638.5 ± 181.1	8426.5 ± 106.5
1200-1400	15166.5 ± 128.2	13100.5 ± 126.9	15842.5 ± 144	5252 ± 85.4
1400-1600	10103 ± 106.9	8206.5 ± 101.1	9590 ± 112.9	3028.5 ± 65.4
1600-1800	6684 ± 88	5076 ± 81.4	5866 ± 88.1	1900 ± 51.7
1800-2000	4332 ± 72.2	3306 ± 65.6	3726 ± 71	1166.5 ± 39.4
2000-2200	3038.5 ± 60.7	2189 ± 53.5	2354.5 ± 57.1	753.5 ± 32
2200-2400	2023.5 ± 50.6	1368 ± 43	1602.5 ± 45.3	438 ± 25.8

Table A.2: Number of observed K_s^0-decays on DATA 2010, Magnet Down, in bins of transverse momentum p_T and rapidity y.

p_T(MeV/c)/y	2.5 - 3.0	3.0 - 3.5	3.5 - 4.0	4.0 - 4.5
0-200	19841.5 ± 147.7	67027 ± 273.1	44132.5 ± 226.7	7010.5 ± 98.8
200-400	46450.5 ± 221.5	149293 ± 398.1	135624 ± 387.8	43512.5 ± 228.4
400-600	74030.5 ± 278.2	152038 ± 401	157866 ± 423.7	63792.5 ± 279.5
600-800	77094.5 ± 283.7	110238 ± 344	121558 ± 379.9	45560 ± 239
800-1000	62798 ± 256.4	70451 ± 280.8	81242 ± 316.8	27795.5 ± 189.8
1000-1200	44913.5 ± 217.9	43283 ± 225.9	51759 ± 257	16893.5 ± 150.9
1200-1400	30654.5 ± 182.7	26694 ± 181	31159.5 ± 202.9	10088.5 ± 117.7
1400-1600	20378 ± 151.5	16342.5 ± 143.8	19206.5 ± 160.4	6319 ± 93.2
1600-1800	13290 ± 125	10370.5 ± 115.7	11821 ± 125.9	3684.5 ± 72
1800-2000	8954.5 ± 103.6	6565 ± 92.3	7374.5 ± 99.8	2324 ± 56.9
2000-2200	5895.5 ± 85.6	4277 ± 74.8	4720 ± 80.2	1476.5 ± 46.1
2200-2400	3974.5 ± 70.2	2833.5 ± 60.6	2999.5 ± 63.3	963.5 ± 35.2

Table A.3: Number of observed Λ-decays on DATA2010, Magnet Down, in bins of transverse momentum p_T and rapidity y.

p_T(MeV/c)/y	2.5 - 3.0	3.0 - 3.5	3.5 - 4.0
200-400	1486.5 ± 46.4	2929 ± 79.9	538 ± 39.9
400-600	3275.5 ± 65.2	5775.5 ± 103.5	2689.5 ± 75.4
600-800	3097.5 ± 64.5	7899 ± 112.5	3511 ± 79.8
800-1000	2730 ± 60.8	7519.5 ± 105.6	3648.5 ± 78
1000-1200	2373.5 ± 57.3	5291 ± 88.8	3419.5 ± 73
1200-1400	1990 ± 52.5	3442 ± 71.5	2745 ± 63.7
1400-1600	1521 ± 45.5	2160 ± 55.1	1884.5 ± 51.9
1600-1800	1126 ± 39.5	1365.5 ± 44.6	1198 ± 41.8
1800-2000	808.5 ± 33.3	847 ± 34.6	860.5 ± 34.8
2000-2200	621 ± 29	541 ± 28.7	529 ± 27.4
2200-2400	408.5 ± 24.2	362 ± 22.1	293 ± 22.4

Table A.4: Number of observed Λ-decays on DATA2010, Magnet Up, in bins of transverse momentum p_T and rapidity y.

p_T(MeV/c)/y	2.5 - 3.0	3.0 - 3.5	3.5 - 4.0
200-400	3098.5 ± 68.1	5987.5 ± 114.5	1280 ± 56.6
400-600	6845 ± 94.9	11852.5 ± 147.1	5696.5 ± 107.4
600-800	6787 ± 93.8	16214 ± 161.1	7448.5 ± 114.1
800-1000	5783 ± 87.3	15011 ± 150.6	7842.5 ± 111.3
1000-1200	5182.5 ± 83.2	10879 ± 126.5	7233 ± 104.3
1200-1400	4269 ± 75.4	7295 ± 102.8	5490 ± 90.4
1400-1600	3076 ± 66.1	4573 ± 81.6	3970.5 ± 75
1600-1800	2349 ± 57.7	2799 ± 63.5	2515 ± 59.5
1800-2000	1638 ± 48	1801.5 ± 51.2	1640 ± 48.3
2000-2200	1164 ± 40.1	1098 ± 39.8	971 ± 38.9
2200-2400	828 ± 33.4	730.5 ± 32.5	611 ± 30.9

Table A.5: Number of observed $\overline{\Lambda}$-decays on DATA2010, Magnet Down, in bins of transverse momentum p_T and rapidity y.

p_T(MeV/c)/y	2.5 - 3.0	3.0 - 3.5	3.5 - 4.0
200-400	1365.5 ± 46.7	2542.5 ± 78	558 ± 40.1
400-600	3124.5 ± 64.6	5511.5 ± 101.7	2580.5 ± 74.7
600-800	3168 ± 64.7	7235 ± 111.3	3442 ± 78.3
800-1000	2684.5 ± 60.5	6792 ± 103.9	3586 ± 77.1
1000-1200	2354.5 ± 57.2	4785 ± 86.9	3202.5 ± 71.6
1200-1400	1976.5 ± 51.6	3292 ± 70.1	2522.5 ± 61.8
1400-1600	1460.5 ± 44.9	2008 ± 55.2	1677.5 ± 50.7
1600-1800	1101 ± 39.8	1202.5 ± 43.3	1198.5 ± 41.6
1800-2000	728 ± 33.6	856.5 ± 34.5	710.5 ± 33
2000-2200	540.5 ± 27.8	505.5 ± 27.7	481.5 ± 25.2
2200-2400	394 ± 23.7	354 ± 22.8	297 ± 20.3

Table A.6: Number of observed $\overline{\Lambda}$-decays on DATA2010, Magnet Up, in bins of transverse momentum p_T and rapidity y.

p_T(MeV/c)/y	2.5 - 3.0	3.0 - 3.5	3.5 - 4.0
200-400	2637 ± 64.1	5141 ± 109.6	1120.5 ± 53.9
400-600	6197 ± 91.1	10484.5 ± 139.9	5003 ± 103.1
600-800	5950 ± 89.8	14465 ± 154.8	6524 ± 108.3
800-1000	5192 ± 83.1	13276 ± 144.1	6929.5 ± 106.3
1000-1200	4479.5 ± 77.6	9843.5 ± 122.1	6358 ± 99.4
1200-1400	3866.5 ± 71.8	6380 ± 98.8	4956.5 ± 87
1400-1600	2912 ± 64	4149.5 ± 77.5	3476.5 ± 71.5
1600-1800	2147 ± 55.4	2557.5 ± 61.5	2135 ± 57.4
1800-2000	1484.5 ± 45.9	1630.5 ± 48.9	1452 ± 47.7
2000-2200	1107.5 ± 40.3	1019.5 ± 38.4	873.5 ± 36.4
2200-2400	687.5 ± 31.6	606 ± 30.9	555.5 ± 29.5

A.2 Efficiencies

Table A.7: Estimated reconstruction and selection efficiencies (in %) for K_s^0-decays on MC 2010, Magnet Down, in bins of transverse momentum p_T and rapidity y.

p_T(MeV/c)/y	2.5 - 3.0	3.0 - 3.5	3.5 - 4.0	4.0 - 4.5
0-200	2 ± 0	7.3 ± 0.1	5.3 ± 0.1	0.9 ± 0
200-400	2.2 ± 0	7.6 ± 0	7.5 ± 0	2.6 ± 0
400-600	3.6 ± 0	8.1 ± 0	9.3 ± 0.1	4.1 ± 0
600-800	5.2 ± 0	8 ± 0.1	9.9 ± 0.1	4.3 ± 0.1
800-1000	6.2 ± 0.1	7.6 ± 0.1	10.1 ± 0.1	4.2 ± 0.1
1000-1200	6.7 ± 0.1	7.2 ± 0.1	9.9 ± 0.1	4 ± 0.1
1200-1400	6.9 ± 0.1	6.6 ± 0.1	9.4 ± 0.2	4 ± 0.1
1400-1600	7.1 ± 0.2	5.9 ± 0.2	8.8 ± 0.2	3.6 ± 0.2
1600-1800	6.6 ± 0.2	5.6 ± 0.2	7.9 ± 0.3	3.4 ± 0.2
1800-2000	6.6 ± 0.3	5.3 ± 0.3	7.3 ± 0.3	3.3 ± 0.2
2000-2200	5.5 ± 0.3	5.2 ± 0.3	6.6 ± 0.4	2.8 ± 0.3
2200-2400	6 ± 0.3	4.4 ± 0.3	6 ± 0.4	3 ± 0.3

Table A.8: Estimated reconstruction and selection efficiencies (in %) for K_s^0-decays on MC 2010, Magnet Up, in bins of transverse momentum p_T and rapidity y.

p_T(MeV/c)/y	2.5 - 3.0	3.0 - 3.5	3.5 - 4.0	4.0 - 4.5
0-200	2 ± 0	7.3 ± 0.1	5.4 ± 0.1	0.9 ± 0
200-400	2.2 ± 0	7.7 ± 0.1	7.5 ± 0.1	2.5 ± 0
400-600	3.7 ± 0	8.1 ± 0.1	9.3 ± 0.1	4.2 ± 0
600-800	5.1 ± 0.1	8 ± 0.1	9.9 ± 0.1	4.4 ± 0.1
800-1000	6.3 ± 0.1	7.8 ± 0.1	10.3 ± 0.1	4.2 ± 0.1
1000-1200	6.7 ± 0.1	7.3 ± 0.1	9.7 ± 0.2	4 ± 0.1
1200-1400	6.9 ± 0.1	6.8 ± 0.2	9.2 ± 0.2	3.6 ± 0.1
1400-1600	6.6 ± 0.2	6.4 ± 0.2	8.8 ± 0.3	3.2 ± 0.2
1600-1800	6.5 ± 0.2	6.1 ± 0.2	7.8 ± 0.3	3.2 ± 0.2
1800-2000	6.3 ± 0.3	5.7 ± 0.3	7.3 ± 0.4	2.9 ± 0.3
2000-2200	5.9 ± 0.3	4.2 ± 0.3	7.6 ± 0.4	2.8 ± 0.3
2200-2400	5.5 ± 0.4	5 ± 0.4	6.5 ± 0.5	2.2 ± 0.3

Table A.9: Estimated reconstruction and selection efficiencies (in %) for Λ-decays on MC 2010, Magnet Down, in bins of transverse momentum p_T and rapidity y.

p_T(MeV/c)/y	2.5 - 3.0	3.0 - 3.5	3.5 - 4.0
200-400	0.9 ± 0	1.7 ± 0.1	0.4 ± 0
400-600	1.6 ± 0.1	2.8 ± 0.1	1.5 ± 0.1
600-800	1.7 ± 0.1	4.1 ± 0.1	2.1 ± 0.1
800-1000	1.5 ± 0.1	4.4 ± 0.2	2.8 ± 0.1
1000-1200	1.8 ± 0.1	4.5 ± 0.2	3.4 ± 0.2
1200-1400	2 ± 0.2	4.3 ± 0.2	4 ± 0.3
1400-1600	2.1 ± 0.2	3.2 ± 0.3	2.8 ± 0.3
1600-1800	2.1 ± 0.2	2.8 ± 0.3	3.2 ± 0.4
1800-2000	2 ± 0.3	2.1 ± 0.4	1.9 ± 0.4
2000-2200	2.5 ± 0.4	1.9 ± 0.4	3.2 ± 0.5
2200-2400	1.9 ± 0.4	2.1 ± 0.5	3.7 ± 0.6

Table A.10: Estimated reconstruction and selection efficiencies (in %) for Λ-decays on MC 2010, Magnet Up, in bins of transverse momentum p_T and rapidity y.

p_T(MeV/c)/y	2.5 - 3.0	3.0 - 3.5	3.5 - 4.0
200-400	0.9 ± 0.1	1.9 ± 0.1	0.4 ± 0.1
400-600	1.6 ± 0.1	3 ± 0.1	1.6 ± 0.1
600-800	1.7 ± 0.1	4.1 ± 0.1	2.3 ± 0.1
800-1000	1.5 ± 0.1	4.7 ± 0.2	2.7 ± 0.2
1000-1200	1.8 ± 0.1	4.3 ± 0.2	3.6 ± 0.2
1200-1400	2.4 ± 0.2	4.1 ± 0.3	3.5 ± 0.3
1400-1600	2 ± 0.2	3.3 ± 0.3	3.5 ± 0.3
1600-1800	2.3 ± 0.3	2.6 ± 0.4	2.7 ± 0.4
1800-2000	2.1 ± 0.3	2.8 ± 0.4	2.2 ± 0.5
2000-2200	2.8 ± 0.4	1.9 ± 0.5	2.8 ± 0.6
2200-2400	1.4 ± 0.5	1.6 ± 0.5	3.3 ± 0.7

Table A.11: Estimated reconstruction and selection efficiencies (in %) for $\overline{\Lambda}$-decays on MC 2010, Magnet Down, in bins of transverse momentum p_T and rapidity y.

p_T(MeV/c)/y	2.5 - 3.0	3.0 - 3.5	3.5 - 4.0
200-400	0.9 ± 0.1	1.7 ± 0.1	0.3 ± 0
400-600	1.4 ± 0.1	2.9 ± 0.1	1.5 ± 0.1
600-800	1.5 ± 0.1	4.1 ± 0.1	2.1 ± 0.1
800-1000	1.5 ± 0.1	4.5 ± 0.2	2.8 ± 0.1
1000-1200	1.8 ± 0.1	4.4 ± 0.2	3.4 ± 0.2
1200-1400	2.1 ± 0.2	3.7 ± 0.2	3.3 ± 0.3
1400-1600	1.8 ± 0.2	3.4 ± 0.3	3.4 ± 0.3
1600-1800	2.3 ± 0.2	3.4 ± 0.3	3.1 ± 0.4
1800-2000	2.4 ± 0.3	2.8 ± 0.4	3 ± 0.4
2000-2200	2 ± 0.4	2.7 ± 0.4	3 ± 0.5
2200-2400	1.9 ± 0.5	2.2 ± 0.4	3.3 ± 0.7

Table A.12: Estimated reconstruction and selection efficiencies (in %) for $\overline{\Lambda}$-decays on MC 2010, Magnet Up, in bins of transverse momentum p_T and rapidity y.

p_T(MeV/c)/y	2.5 - 3.0	3.0 - 3.5	3.5 - 4.0
200-400	0.8 ± 0.1	1.6 ± 0.1	0.3 ± 0.1
400-600	1.5 ± 0.1	2.7 ± 0.1	1.5 ± 0.1
600-800	1.5 ± 0.1	4 ± 0.1	2.1 ± 0.1
800-1000	1.6 ± 0.1	4.3 ± 0.2	2.6 ± 0.2
1000-1200	1.6 ± 0.1	4.1 ± 0.2	3.1 ± 0.2
1200-1400	2 ± 0.2	4.1 ± 0.3	3.7 ± 0.3
1400-1600	2.2 ± 0.2	3.2 ± 0.3	3.2 ± 0.3
1600-1800	2.6 ± 0.3	2.8 ± 0.4	3.5 ± 0.4
1800-2000	1.9 ± 0.4	2.1 ± 0.4	3.1 ± 0.5
2000-2200	1.7 ± 0.3	1.9 ± 0.4	2.8 ± 0.6
2200-2400	1.3 ± 0.5	2.4 ± 0.6	2.3 ± 0.7

A.3 Cross-sections for both B-field polarities

Table A.13: Observed K^0_s production cross-section (in μb) in bins of transverse momentum p_T and rapidity y on DATA2010, Magnet Down. The quoted error is statistical.

p_T(MeV/c)/y	2.5 - 3.0	3.0 - 3.5	3.5 - 4.0	4.0 - 4.5
0-200	818.3 ± 16.1	777.8 ± 8.7	693.6 ± 9.9	626.2 ± 27.2
200-400	1819.7 ± 22.5	1645.3 ± 11.5	1488.6 ± 11.2	1422.3 ± 19.5
400-600	1706.7 ± 17.5	1566.5 ± 11.2	1436.5 ± 10.4	1319.5 ± 15.5
600-800	1239 ± 12.9	1138.4 ± 10.2	1025.7 ± 9.1	897.6 ± 13.1
800-1000	841 ± 10.6	776.5 ± 9.6	679.1 ± 8	557.8 ± 11.1
1000-1200	563.9 ± 9	509.4 ± 8.7	435.2 ± 7	351.2 ± 9.8
1200-1400	365.7 ± 7.6	332 ± 7.9	281.2 ± 6.1	221 ± 8.3
1400-1600	239.6 ± 6.3	231.2 ± 7.3	181.6 ± 5.2	142.7 ± 7.4
1600-1800	170.2 ± 5.7	150.6 ± 6	125.2 ± 4.8	95 ± 6.3
1800-2000	109.4 ± 4.5	105.4 ± 5.5	85.4 ± 4.1	58.7 ± 4.5
2000-2200	93.1 ± 5.1	70.8 ± 4.3	59.9 ± 3.6	45.8 ± 5
2200-2400	56.1 ± 3.5	52.1 ± 4	45 ± 3.6	24.6 ± 3.2

Table A.14: Observed K^0_s production cross-section (in μb) in bins of transverse momentum p_T and rapidity y on DATA2010, Magnet Up. The quoted error is statistical.

p_T(MeV/c)/y	2.5 - 3.0	3.0 - 3.5	3.5 - 4.0	4.0 - 4.5
0-200	822.7 ± 16.7	772.8 ± 8.7	691.3 ± 10	621.6 ± 26.9
200-400	1798.6 ± 22.6	1629.3 ± 11.6	1523.6 ± 11.7	1442.6 ± 20.5
400-600	1697.3 ± 17.5	1573.4 ± 11.6	1422.2 ± 10.6	1285 ± 15.3
600-800	1258.7 ± 13.7	1149.9 ± 10.6	1031.9 ± 9.5	876.9 ± 12.9
800-1000	834.7 ± 10.9	755.3 ± 9.6	658 ± 8	556.9 ± 11.4
1000-1200	563.2 ± 9.5	496.4 ± 8.9	446.9 ± 7.7	351.3 ± 10.1
1200-1400	371.6 ± 8.1	330.3 ± 8.1	283.7 ± 6.6	232.1 ± 9.4
1400-1600	257.1 ± 7.3	215.1 ± 6.9	182.2 ± 5.5	165.6 ± 9.3
1600-1800	172.6 ± 6.3	142.1 ± 5.8	127.2 ± 5.2	95.3 ± 6.8
1800-2000	118.3 ± 5.4	96.7 ± 5.1	84.5 ± 4.4	67.3 ± 6.3
2000-2200	83.8 ± 4.7	84.4 ± 6.1	52 ± 3	45 ± 5
2200-2400	61 ± 4.3	47.9 ± 3.8	38.5 ± 2.9	36.6 ± 5.7

Table A.15: Observed Λ production cross-section (in μb) in bins of transverse momentum p_T and rapidity y on DATA2010, Magnet Down. The quoted error is statistical.

p_T(MeV/c)/y	2.5 - 3.0	3.0 - 3.5	3.5 - 4.0
200-400	283.6 ± 18.3	294.1 ± 16.7	252.9 ± 39.1
400-600	344 ± 14	350 ± 13.6	307.3 ± 17.8
600-800	312.3 ± 14.3	326.5 ± 11.1	278.9 ± 14.7
800-1000	307.9 ± 18.6	289.2 ± 11.6	217.5 ± 11.6
1000-1200	223.3 ± 15.8	198.7 ± 9.7	168.7 ± 10.2
1200-1400	167.4 ± 13.6	135.2 ± 8.3	116.3 ± 8.1
1400-1600	121 ± 12.1	113.1 ± 9.7	111.5 ± 12.6
1600-1800	89.1 ± 10.7	80.7 ± 9.6	62.8 ± 7.4
1800-2000	68.3 ± 11.1	66.6 ± 12.3	75.2 ± 16.3
2000-2200	42.3 ± 6.7	47.4 ± 9.8	28 ± 4.4
2200-2400	36.2 ± 8.3	29.3 ± 7.1	13.1 ± 2.2

Table A.16: Observed Λ production cross-section (in μb) in bins of transverse momentum p_T and rapidity y on DATA2010, Magnet Up. The quoted error is statistical.

p_T(MeV/c)/y	2.5 - 3.0	3.0 - 3.5	3.5 - 4.0
200-400	277.8 ± 17.7	257.5 ± 13.3	278.8 ± 40.7
400-600	361.9 ± 15.7	327.3 ± 12.4	302.9 ± 17.7
600-800	329.6 ± 14.7	332.4 ± 12	266.2 ± 13.6
800-1000	327.5 ± 21.9	270.5 ± 11.2	242.2 ± 14.3
1000-1200	237.7 ± 17.6	213.4 ± 12	169.4 ± 10.4
1200-1400	149 ± 11.2	148.1 ± 9.8	130.7 ± 10.6
1400-1600	129 ± 15	115 ± 11.2	96.4 ± 9.6
1600-1800	86.8 ± 11.7	91.1 ± 14	78.1 ± 12.2
1800-2000	64.7 ± 10.6	53.9 ± 8.5	62.6 ± 13.4
2000-2200	35.1 ± 5.6	49.4 ± 13.7	29 ± 6.2
2200-2400	48.1 ± 17	39.1 ± 13.6	15.3 ± 3.4

Table A.17: Observed $\overline{\Lambda}$production cross-section (in μb) in bins of transverse momentum p_T and rapidity y on DATA2010, Magnet Down. The quoted error is statistical.

p_T(MeV/c)/y	2.5 - 3.0	3.0 - 3.5	3.5 - 4.0
200-400	259 ± 17.2	246.3 ± 14.1	268.7 ± 42.9
400-600	376.1 ± 17	313.3 ± 11.8	288.4 ± 17.3
600-800	346.2 ± 16.9	294.3 ± 10.2	271.3 ± 14.6
800-1000	298.5 ± 18.1	254.9 ± 10.3	215.8 ± 11.8
1000-1200	223.3 ± 15.8	181.1 ± 9.1	160 ± 10.3
1200-1400	156.3 ± 12.5	150.8 ± 10.7	128.3 ± 10.5
1400-1600	133.7 ± 15.6	98.2 ± 8.7	83.4 ± 8.4
1600-1800	79.7 ± 8.9	59.5 ± 6.3	65.1 ± 8.3
1800-2000	50.5 ± 7.5	51.5 ± 7.6	39.9 ± 5.6
2000-2200	45.2 ± 8.3	31.5 ± 5.3	26.7 ± 4.7
2200-2400	34.7 ± 9.5	26.7 ± 5.5	15.3 ± 3.3

Table A.18: Observed $\overline{\Lambda}$production cross-section (in μb) in bins of transverse momentum p_T and rapidity y on DATA2010, Magnet Up. The quoted error is statistical.

p_T(MeV/c)/y	2.5 - 3.0	3.0 - 3.5	3.5 - 4.0
200-400	271 ± 19.4	261.4 ± 16.3	279 ± 46.3
400-600	347.8 ± 15.7	319.7 ± 13.4	288.7 ± 18.3
600-800	326.4 ± 16.8	305.8 ± 11.6	265.3 ± 15.2
800-1000	273.7 ± 16	256.6 ± 11.4	219.8 ± 13.3
1000-1200	232.3 ± 18.6	202.5 ± 11.7	171.8 ± 12.1
1200-1400	165.3 ± 14.9	129.1 ± 8.5	111.4 ± 8.6
1400-1600	109.9 ± 11.2	108.4 ± 11.5	92.5 ± 10
1600-1800	70.4 ± 8.2	76.9 ± 11.4	51.4 ± 6.7
1800-2000	65.4 ± 13.1	66.5 ± 13.3	38.8 ± 6.3
2000-2200	55.1 ± 10.8	45.6 ± 10	26.2 ± 5.8
2200-2400	42.7 ± 16.8	21.6 ± 5.3	20.5 ± 6.2

A.4 Systematics

Table A.19: Estimated uncertainties (in %) due to background estimation for K^0_s-decays.

p_T/y	2.5 - 3.0	3.0 - 3.5	3.5 - 4.0	4.0 - 4.5
0-200	1.20	-0.07	-0.18	-3.73
200-400	1.33	0.56	-0.10	-1.84
400-600	0.98	0.73	-0.03	-1.46
600-800	1.65	1.32	0.51	-0.44
800-1000	1.09	0.96	0.67	-0.63
1000-1200	1.14	0.86	0.84	-0.55
1200-1400	0.63	0.89	1.42	0.00
1400-1600	1.25	0.24	2.98	-0.48
1600-1800	2.85	1.14	-0.46	0.24
1800-2000	2.53	0.26	0.27	3.59
2000-2200	-0.14	1.05	3.04	-1.17
2200-2400	-0.54	3.59	-1.80	-7.61

Table A.20: Estimated uncertainties (in %) due to background estimation for Λ-decays.

p_T/y	2.5 - 3.0	3.0 - 3.5	3.5 - 4.0
200-400	-0.18	3.87	0.84
400-600	2.74	2.60	4.50
600-800	6.14	5.67	5.07
800-1000	-3.17	0.91	0.13
1000-1200	-1.65	2.34	6.36
1200-1400	8.34	4.50	1.76
1400-1600	1.65	1.80	-0.35
1600-1800	-4.15	-11.74	-6.72
1800-2000	-3.95	-8.91	-14.27
2000-2200	13.19	-4.12	16.14
2200-2400	-20.15	-14.40	26.66

Table A.21: Estimated uncertainties (in %) due to background estimation for $\overline{\Lambda}$-decays.

p_T/y	2.5 - 3.0	3.0 - 3.5	3.5 - 4.0
200-400	-1.66	3.09	2.93
400-600	-0.13	4.19	0.23
600-800	1.82	-0.33	2.96
800-1000	2.45	1.92	-4.40
1000-1200	5.57	3.36	3.74
1200-1400	1.56	1.16	-1.14
1400-1600	9.77	-4.02	-2.65
1600-1800	-7.05	-3.89	13.51
1800-2000	-0.84	4.95	13.13
2000-2200	-28.24	10.08	4.40
2200-2400	3.60	-9.87	3.92

Table A.22: Estimated uncertainties (in %) due to binning (generator dependence) for K_s^0-decays.

p_T/y	2.5 - 3.0	3.0 - 3.5	3.5 - 4.0	4.0 - 4.5
0-200	-1.23	0.17	-0.62	1.67
200-400	-0.31	0.07	0.15	-0.78
400-600	0.29	0.17	-0.03	0.08
600-800	-0.04	0.23	-0.16	0.76
800-1000	0.22	0.23	-0.26	0.05
1000-1200	0.06	0.04	-0.02	-0.58
1200-1400	0.16	0.31	-0.05	-0.48
1400-1600	0.23	0.18	0.01	2.26
1600-1800	0.72	0.79	0.00	0.58
1800-2000	0.46	2.79	0.28	3.75
2000-2200	0.96	0.53	1.06	-0.59
2200-2400	1.26	3.76	1.08	19.17

Table A.23: Estimated uncertainties (in %) due to binning (generator dependence) for Λ-decays.

p_T/y	2.5 - 3.0	3.0 - 3.5	3.5 - 4.0
200 - 400	1.19	0.11	-1.44
400 - 600	4.24	-0.06	4.07
600 - 800	-2.77	-0.15	0.81
800 - 1000	-0.71	0.16	-0.25
1000 - 1200	-0.42	0.27	-0.00
1200 - 1400	-0.03	-0.93	1.87
1400 - 1600	3.41	0.94	1.68
1600 - 1800	3.31	0.35	-0.09
1800 - 2000	5.35	4.3	7.55
2000 - 2200	3.04	14.9	5.62
2200 - 2400	18.7	10.6	9.03

Table A.24: Estimated uncertainties (in %) due to binning (generator dependence) for $\overline{\Lambda}$-decays.

p_T/y	2.5 - 3.0	3.0 - 3.5	3.5 - 4.0
200 - 400	-1.49	2.83	-15.5
400 - 600	-0.98	-0.63	2.98
600 - 800	-1.95	0.06	0.07
800 - 1000	-0.98	-0.19	-0.91
1000 - 1200	0.23	1.43	-0.56
1200 - 1400	0.56	1.13	1.01
1400 - 1600	0.61	-0.54	-0.02
1600 - 1800	2.4	1.39	9.87
1800 - 2000	1.44	-0.67	3.78
2000 - 2200	36.6	23.4	-0.07
2200 - 2400	7.53	5.34	11

Table A.25: Estimated uncertainties (in %) due to difference in reconstruction efficiencies for opposite magnet polarities for K_s^0-decays.

p_T/y	2.5 - 3.0	3.0 - 3.5	3.5 - 4.0	4.0 - 4.5
0-200	-1.23	0.17	-0.62	1.67
200-400	-0.31	0.07	0.15	-0.78
400-600	0.29	0.17	-0.03	0.08
600-800	-0.04	0.23	-0.16	0.76
800-1000	0.22	0.23	-0.26	0.05
1000-1200	0.06	0.04	-0.02	-0.58
1200-1400	0.16	0.31	-0.05	-0.48
1400-1600	0.23	0.18	0.01	2.26
1600-1800	0.72	0.79	0.00	0.58
1800-2000	0.46	2.79	0.28	3.75
2000-2200	0.96	0.53	1.06	-0.59
2200-2400	1.26	3.76	1.08	19.17

Table A.26: Estimated uncertainties (in %) due to difference in reconstruction efficiencies for opposite magnet polarities for Λ-decays.

p_T/y	2.5 - 3.0	3.0 - 3.5	3.5 - 4.0
200 - 400	-3.39	10	1.59
400 - 600	-0.92	4.28	10.1
600 - 800	-6.44	-1.8	-4.07
800 - 1000	-2.67	1.23	-2.6
1000 - 1200	-13.6	-7.43	0.00
1200 - 1400	10.4	-7.73	-4.58
1400 - 1600	-6.74	-4.67	7.43
1600 - 1800	9.32	5.86	-0.77
1800 - 2000	-9.9	11.4	8.44
2000 - 2200	37.7	8.4	14.3
2200 - 2400	-17	-24.2	-11.6

Table A.27: Estimated uncertainties (in %) due to difference in reconstruction efficiencies for opposite magnet polarities for $\overline{\Lambda}$-decays.

p_T/y	2.5 - 3.0	3.0 - 3.5	3.5 - 4.0
200 - 400	2.0	-5.8	-9.6
400 - 600	3.5	4.9	-0.7
600 - 800	7.5	1.8	-1.0
800 - 1000	0.4	2.5	-2.4
1000 - 1200	1.11	-6.7	-10.1
1200 - 1400	2.6	3.5	-3.2
1400 - 1600	3.6	-2.5	-2.2
1600 - 1800	5.8	-4.2	32.4
1800 - 2000	-0.6	-6.9	10.9
2000 - 2200	-35.7	-38.1	-7.7
2200 - 2400	11	58.1	-28.7

A.5 Cross-sections

Table A.28: Measured K^0_s production cross-section (in μb) in bins of transverse momentum p_T and rapidity y as defined on Eq. 4.3. The first quoted error is statistical and the second is the local systematic error. The total global systematic uncertainty is 12%.

p_T/y	2.5 - 3.0	3.0 - 3.5	3.5 - 4.0	4.0 - 4.5
0-200	821 ± 12 ± 67	775 ± 6 ± 61	692 ± 7 ± 56	624 ± 19 ± 58
200-400	1809 ± 16 ± 145	1637 ± 8 ± 130	1506 ± 8 ± 121	1432 ± 14 ± 116
400-600	1702 ± 12 ± 135	1570 ± 8 ± 124	1429 ± 7 ± 115	1302 ± 11 ± 109
600-800	1249 ± 9 ± 103	1144 ± 7 ± 91	1029 ± 7 ± 81	887 ± 9 ± 76
800-1000	838 ± 8 ± 66	766 ± 7 ± 65	669 ± 6 ± 57	557 ± 8 ± 44
1000-1200	563 ± 7 ± 45	503 ± 6 ± 45	441 ± 5 ± 36	351 ± 7 ± 28
1200-1400	369 ± 6 ± 30	331 ± 6 ± 26	282 ± 5 ± 24	227 ± 6 ± 18
1400-1600	248 ± 5 ± 28	223 ± 5 ± 23	182 ± 4 ± 15	154 ± 6 ± 26
1600-1800	171 ± 4 ± 15	146 ± 4 ± 18	126 ± 4 ± 10	95 ± 5 ± 9
1800-2000	114 ± 4 ± 12	101 ± 4 ± 14	85 ± 3 ± 7	63 ± 4 ± 7
2000-2200	88 ± 3 ± 11	78 ± 4 ± 9	56 ± 2 ± 6	45 ± 4 ± 7
2200-2400	59 ± 3 ± 6	50 ± 3 ± 9	42 ± 2 ± 5	31 ± 3 ± 9

Table A.29: Measured Λ production cross-section (in μb) in bins of transverse momentum p_T and rapidity y as defined on Eq. 4.3. The first quoted error is statistical and the second is the local systematic error. The total global systematic uncertainty is 12%.

p_T/y	2.5 - 3.0	3.0 - 3.5	3.5 - 4.0
200-400	281 ± 13 ± 25	276 ± 11 ± 37	266 ± 28 ± 23
400-600	353 ± 11 ± 34	339 ± 9 ± 33	305 ± 13 ± 44
600-800	321 ± 10 ± 40	329 ± 8 ± 34	273 ± 10 ± 29
800-1000	318 ± 14 ± 30	280 ± 8 ± 24	230 ± 9 ± 20
1000-1200	231 ± 12 ± 37	206 ± 8 ± 23	169 ± 7 ± 18
1200-1400	158 ± 9 ± 25	142 ± 6 ± 17	123 ± 7 ± 12
1400-1600	125 ± 10 ± 14	114 ± 7 ± 11	104 ± 8 ± 12
1600-1800	88 ± 8 ± 12	86 ± 8 ± 13	70 ± 7 ± 8
1800-2000	67 ± 8 ± 10	60 ± 7 ± 10	69 ± 11 ± 14
2000-2200	39 ± 4 ± 16	48 ± 8 ± 9	28 ± 4 ± 7
2200-2400	42 ± 9 ± 14	34 ± 8 ± 11	14 ± 2 ± 4

Table A.30: Estimated $\overline{\Lambda}$ production cross-section (in μb) in bins of transverse momentum p_T and rapidity y as defined on Eq. 4.3. The first quoted error is statistical and the second is the local systematic error. The total global systematic uncertainty is 12%.

p_T/y	2.5 - 3.0	3.0 - 3.5	3.5 - 4.0
200-400	265 ± 13 ± 23	254 ± 11 ± 28	274 ± 32 ± 55
400-600	362 ± 12 ± 33	317 ± 9 ± 33	289 ± 13 ± 25
600-800	336 ± 12 ± 39	300 ± 8 ± 25	268 ± 11 ± 24
800-1000	286 ± 12 ± 25	256 ± 8 ± 23	218 ± 9 ± 21
1000-1200	228 ± 12 ± 23	192 ± 7 ± 22	166 ± 8 ± 22
1200-1400	161 ± 10 ± 14	140 ± 7 ± 13	120 ± 7 ± 11
1400-1600	122 ± 10 ± 16	103 ± 7 ± 10	88 ± 7 ± 8
1600-1800	75 ± 6 ± 9	68 ± 7 ± 7	58 ± 5 ± 22
1800-2000	58 ± 8 ± 5	59 ± 8 ± 7	39 ± 4 ± 8
2000-2200	50 ± 7 ± 30	39 ± 6 ± 18	26± 4 ± 3
2200-2400	39 ± 10 ± 6	24 ± 4 ± 14	18 ± 4 ± 6

Appendix B

RICH selection

An alternative method for measuring Λ and $\overline{\Lambda}$ yields uses RICH information to reduce the background. V^0-decays can be sufficiently well-identified using only tracking information, and clean mass peaks with very little or practically no background can be obtained. Nevertheless, as a cross-check, RICH particle ID was used to verify the identity of the V^0-daughters, especially for Λ-decays whose combinatorial background is mostly due to pion tracks from K^0_s-decays given a proton mass. As seen in Figure B.1, the momentum of the positive and and negative daughters of the Λ candidates in the signal region (Table 4.2) fall into the active separation range of the RICH subdetectors for proton-pion separation (Figure 4.7). We can also see clearly that the pion is the soft daughter from the decay, which plays a role in Subsection 7.4. The discriminant variable used is DLL(p-π), which stands for 'Delta-Log-Likelihood for proton hypothesis vs pion hypothesis' of the p candidate (defined in Subsection 4.2.3). First, from real data, we can observe in Figure B.2 that the p candidates from Λ-decays in the signal region, peak well right after DLL(p-π) = 0. The p candidates coming from the sidebands fall mostly to the left of the red line. It can also be seen that weighting the sidebands assuming a linear background is a good model, since for DllP (p-π)$<$ 0 it exactly covers the tail left by the p candidates from the signal region.

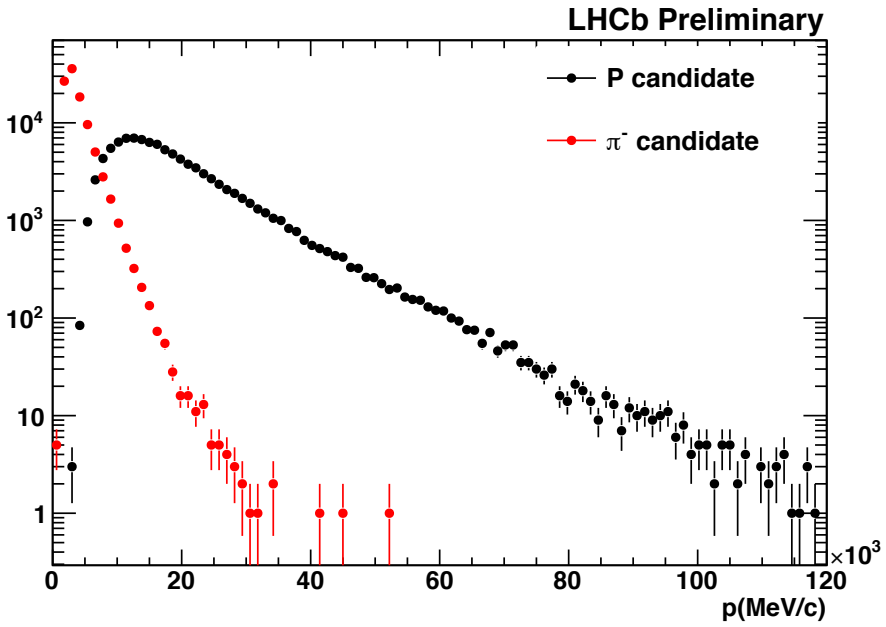

Figure B.1: p candidate (black filled circles) and π candidate (red filled circles) momentum p for Λ-decays, after selection, in the signal region.

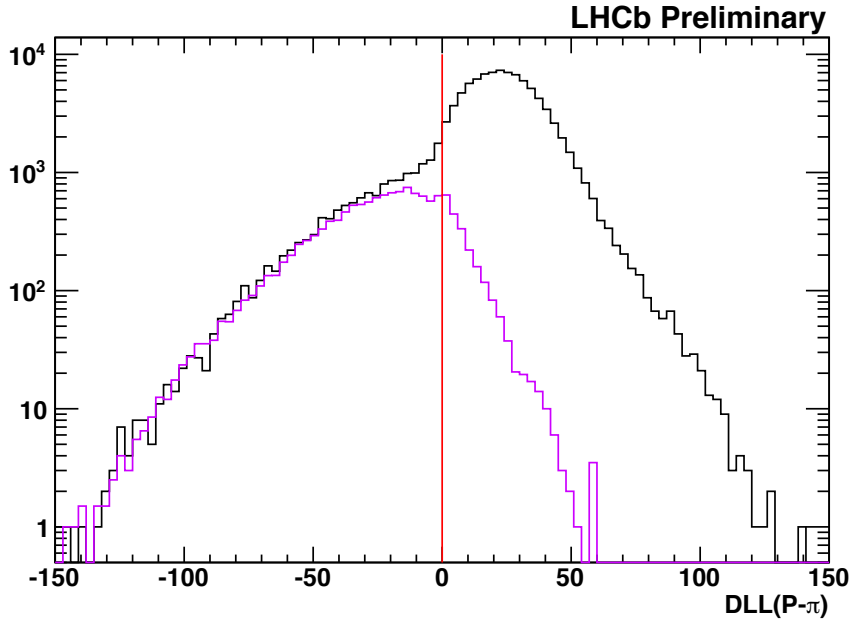

Figure B.2: DLL(p-π) distribution for p candidate momentum for Λ-decays in the signal region (solid black histogram) and sidebands (solid violet histogram).

Finally, Figure B.3 shows a comparison of the DLL(p-π) distributions for p candidates of Λ-decays in the signal region for DATA2010, background subtracted DATA2010, MC2010, and MC truth associated particles. A good match is visible between the four distributions for DLL(p-π) > 0. From this, one can trust that for DLL(p-π) > 0, most of the signal Λ-decays come from true Λ's (and similarly for $\overline{\Lambda}$). Also, one can conclude that there is a fair match between DATA2010 and MC2010. Finally, one can see that the background subtraction method is appropriate, since background subtraction reduces the counts mostly on the DLL(p-π) < 0, which is mostly combinatorial background contamination, and on the right side where the true Λ's appear, both profiles match very well, and there is no significant signal reduction.

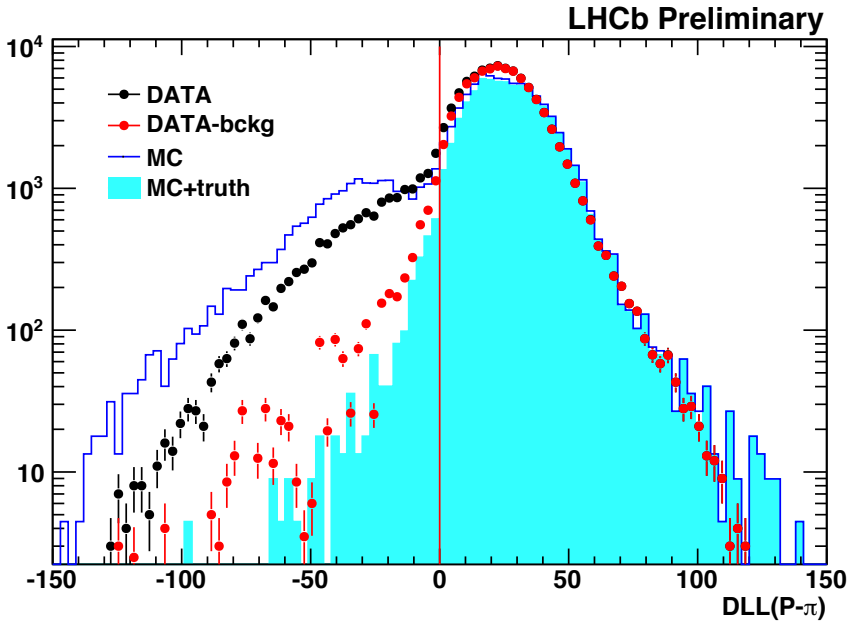

Figure B.3: DLL(p-π) distribution for p candidates from Λ-decays in the signal region for DATA2010 (black filled circles), sideband subtracted DATA2010 (red filled circles), MC2010 (solid blue histogram), and MC truth associated (cyan filled histogram).

The effect of the DLL(p-π) cut on invariant mass distributions can be seen in Figures B.4(a) and B.4(b). The background is reduced almost completely, leaving

the signal untouched for both DATA2010 and MC2010. The effect on the efficiency corrected yields is shown in Tables B.1 and B.2, which demonstrate that there is no significant reduction in yields from using the extra RICH cut while the background is highly suppressed.

Table B.1: Estimated uncertainties (in %) due to RICH particle identification for Λ-decays.

p_T/y	2.5 - 3.0	3.0 - 3.5	3.5 - 4.0
200 - 400	4.36	-5.66	-7.97
400 - 600	5.62	-9.3	-7.63
600 - 800	3.55	-5.24	-7.22
800 - 1000	2.33	-2.5	-6.82
1000 - 1200	1.52	-1.64	-3.22
1200 - 1400	-0.598	-2.01	-3.06
1400 - 1600	-1.2	-1.81	-2.67
1600 - 1800	-1.18	-2.07	-2
1800 - 2000	-2.1	-2.12	-3.41
2000 - 2200	-2.39	-0.965	-2.26
2200 - 2400	-0.984	-3.12	2.18

Table B.2: Estimated uncertainties (in %) due to RICH particle identification for $\overline{\Lambda}$-decays.

p_T/y	2.5 - 3.0	3.0 - 3.5	3.5 - 4.0
200 - 400	8.88	-6.97	-8.6
400 - 600	7.97	-8.37	-7.97
600 - 800	5.22	-6.16	-8.65
800 - 1000	2.42	-3.48	-5.44
1000 - 1200	0.783	-3.39	-3.62
1200 - 1400	-0.903	-2.04	-4.19
1400 - 1600	-1.86	-1.38	-2.84
1600 - 1800	-1.45	-3.29	-3.34
1800 - 2000	-1.47	-2.65	-4.67
2000 - 2200	-1.53	-2.34	-5.72
2200 - 2400	-1.43	-2.53	-1.19

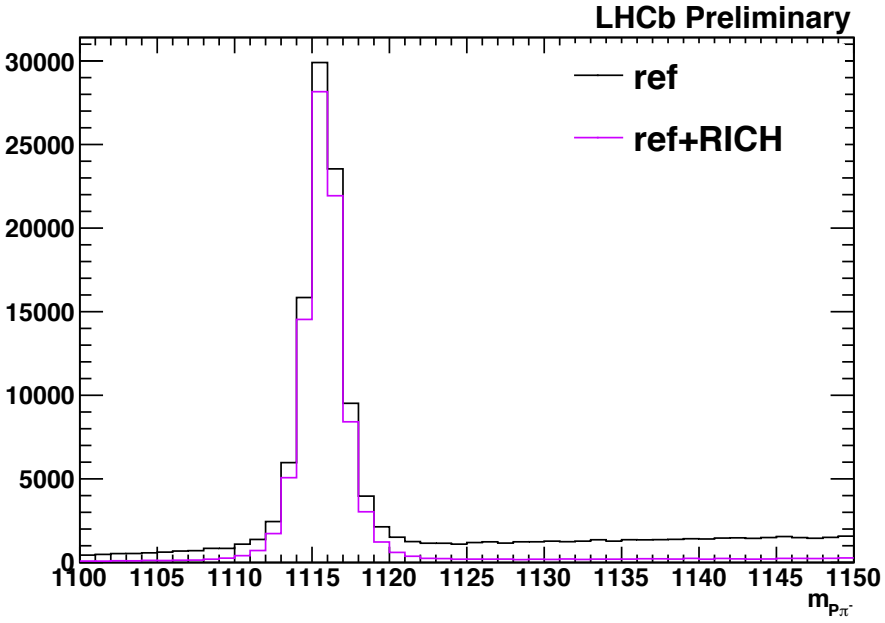

(a) DATA2010

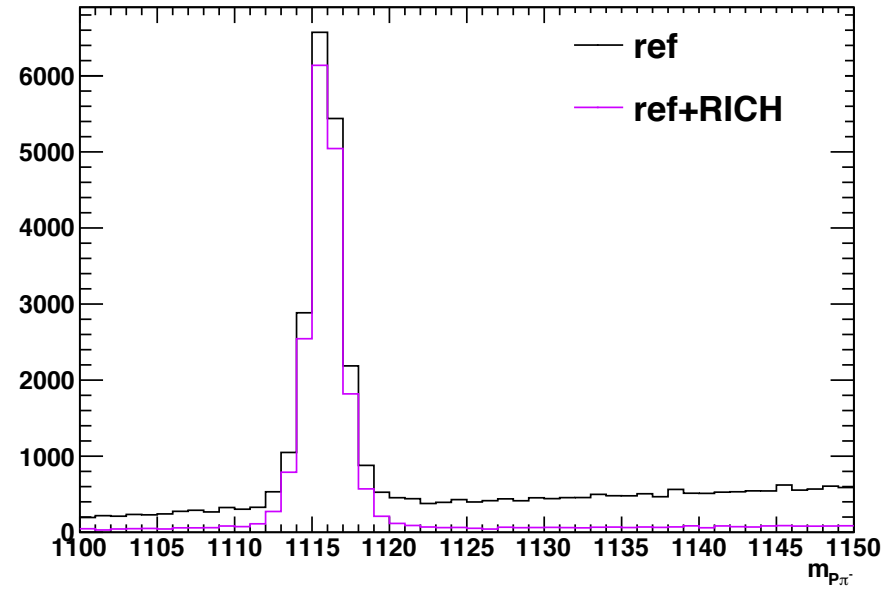

(b) MC2010

Figure B.4: Invariant mass distribution for Λ-decays after selection without RICH cuts (solid black histogram) and after DLL(p-π) > 0 (solid violet histogram).

Appendix C

V^0 production ratios

V^0 production ratios from this measurement were compared with previous results obtained in the experiment at 7 TeV [17], which will be referred to as LHCb 2011. The cross-section ratio of $\overline{\Lambda}$ over Λ production is displayed in Figure C.1 as a function of rapidity, and shows good agreement between DATA2010 and LHCb 2011. The generator level predictions are not consistent with observations, but they are quite close.

Secondly, for $\overline{\Lambda}/K_s^0$ ratios (Figure C.2), DATA2010 and LHCb 2011 are consistent within error bars. The agreement is good considering that the measurements were done using quite different selections. LHCb 2011 has a veto around the K_s^0 mass for the $\pi\pi$ hypothesis for Λ and $\overline{\Lambda}$selection; it was shown in Section 5.5 that this cut removes part of the signal. In addition, efficiency estimations in the case of LHCb 2011 were corrected using weighted distributions, so in general the measurements are sensitive to different systematic uncertainties. One should also keep in mind that this ratio is p_T dependent, that $\overline{\Lambda}$ and K_s^0 have a different p_T spectra, and that the two measurements are not in exactly the same transverse momentum range. Generator predictions in this case largely underestimate the observation.

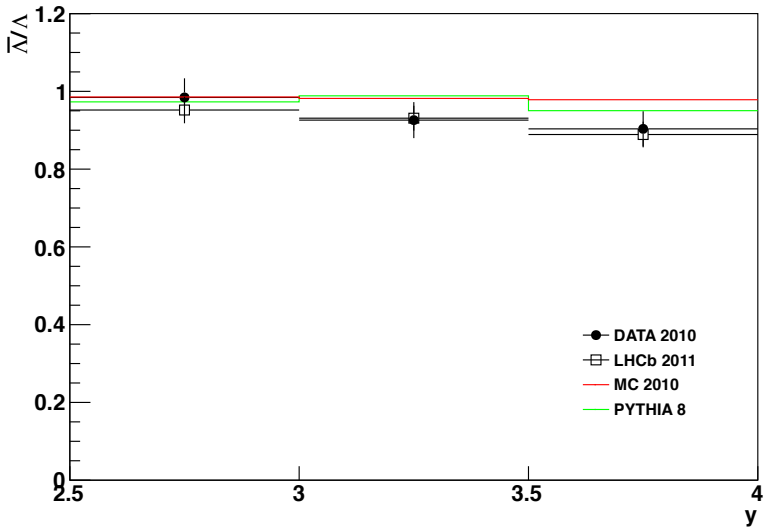

Figure C.1: Measured $\overline{\Lambda}/\Lambda$ production ratios in bins of y for DATA2010 (black filled circles), LHCb 2011 measurement [17] (black hollow circles), and generator predictions by MC2010 (solid red histogram) and PYTHIA 8 (solid green histogram). Error bars represent systematic uncertainties.

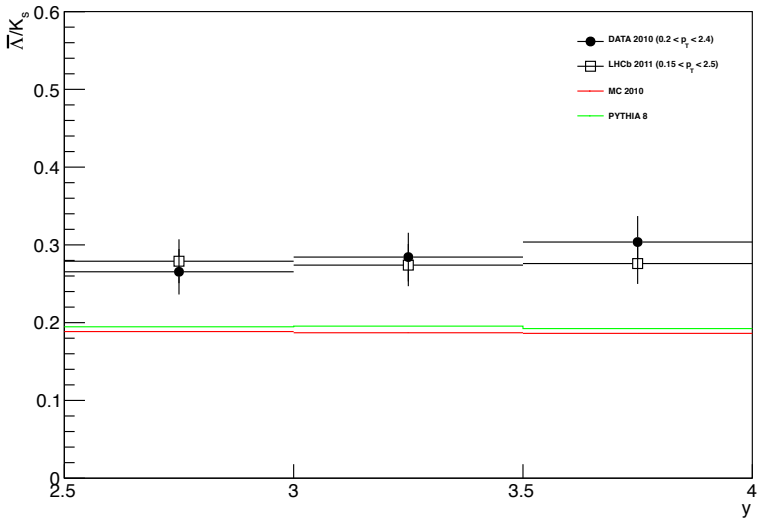

Figure C.2: Measured $\overline{\Lambda}/K_s^0$ production ratios in bins of y for DATA2010 (black filled circles), LHCb 2011 measurement [17](black hollow circles), and generator predictions by MC2010 (solid red histogram) and PYTHIA 8 (solid green histogram). Error bars represent systematic uncertainties.

References

[1] J. Beringer *et al.* (Particle Data Group), *Particle Data Group - 2012 Reviews, Tables, Plots*, PR D86, 010001 (2012), http://pdg.lbl.gov.

[2] P. Skands, *Les-Houches Plots*, http://home.fnal.gov/škands/leshouches-plots/.

[3] Fermilab Visual Media Service, http://www-visualmedia.fnal.gov/.

[4] R.K. Ellis, *Collider Physics: Five Lectures*, 2006, http://theory.fnal.gov/people/ellis/Talks/TASI06/.

[5] B.R. Webber, *A QCD model for jet fragmentation including soft gluon interference*, Nucl. Phys. B 238, 1984.

[6] P.Z. Skands, *QCD for Collider Physics Lectures from the 2010 European School of High Energy Physics (ESHEP 2010), Raseborg, Finland*, arXiv:1104.2863v2 [hep-ph], 2012.

[7] LHCb Collaboration, *LHCb public webpage*, http://lhcb-public.web.cern.ch/lhcb-public/en/detector/Detector-en.html.

[8] CERN, *The accelerator complex*, http://home.web.cern.ch/about/accelerators.

[9] ATLAS Collaboration, http://www.atlas.ch/photos/atlas_photos/selected-photos/lhc/9906025_01_dipmag_diagram.jpg.

[10] H.J. Hilke and T. Nakada (LHCb Collaboration), *The LHCb Experiment*, Technical Proposal, CERN, GENEVA, 1998.

[11] A Augusto Alves Jr et al. (LHCb Collaboration), *The LHCb Detector*, JINST 3, 2008.

[12] O. Steinkamp, *Lhcb silicon tracker home page (Dec. 2009)*, http://lhcb.physik.uzh.ch/SiliconTracker/.

[13] The LHCb Calorimeter, *LHCb public webpage*, https://lhcb-public.web.cern.ch/lhcb-public/en/Detector/Calorimeters2-en.html.

[14] Florin Maciuc for The LHCb Collaboration, *Tracking and Alignment in LHCb*, Physics at LHC, 2010.

[15] LHCb VELO Collaboration, *LHCb VELO Collaboration workspace*, Internal Communication.

[16] A. Powell, *Particle Identification at LHCb*, ICHEP, CERN-LHCb-PROC-2011-008, 2010.

[17] R. Aaij et al. (LHCb collaboration), *Prompt K^0_s production in pp collisions at $\sqrt{s}$ = 0.9 TeV*, Phys. Lett. B 693, 2010.

[18] G. Bocquet et al. (UA1 collaboration), *Inclusive production of strange particles in pp collisions at s= 630 GeV with UA1*, Phys. Lett. B 366, 1996.

[19] G.J. Alner et al. (UA5 collaboration), *Kaon production in pp reactions at a centre-of-mass energy of 540 GeV*, Nucl. Phys. B 258, 1985.

[20] T. Sjostrand, S. Mrenna and P. Skands, *A Brief Introduction to PYTHIA 8.1*, Comput. Phys. Comm. 178 (2008) 852, http://home.thep.lu.se/~torbjorn/Pythia.html.

[21] L. Hoddeson, L. Brown, M. Riordan and M. Dresden, *The Rise of the Standard Model*, Cambridge, 1997.

[22] ATLAS Collaboration, *Observation of a new particle in the search for the Standard Model Higgs boson with the ATLAS detector at the LHC*, Nucl. Phys. B 716:1-29, 2012.

[23] CMS Collaboration, *Observation of a new boson at a mass of 125 GeV with the CMS experiment at the LHC*, Nucl. Phys. B 716:30, 2012.

[24] K. Nakamura *et al.* (Particle Data Group), *Review of particle physics*, J. Phys. G 37, 075021, 2010.

[25] S. M. McGee, *A search for* $D^0 - \overline{D}^0$ *mixing in the semileptonic decay of* $D^0 \to K^* e\nu$, Ph.D. Thesis, Wayne State University, 2002.

[26] D. C. Cheng, *Elementary Particle Physics: An Introduction*, Addison-Wesley, 1979.

[27] C. Amsler *et al.*, *The CKM Quark-Mixing-Matrix*, Phys. Lett. B 667, 2008.

[28] R.K. Ellis, *QCD and Collider Physics*, Cambridge, 1996.

[29] Joint Institute for Nuclear Research (JINR) DUBNA, *The quantum number color, colored quarks and QCD*, http://www.inr.troitsk.ru/quantum.html.

[30] A. Petersen et al., *Multihadronic events at* E_{CM} *= 29GeV and predictions of QCD models from* E_{cm} *= 29 GeV to* E_{cm} *= 93 GeV*, SLAC-PUB-4290, 1987.

[31] T. Sjostrand, *The lund monte carlo for jet fragmentation and* e^+e^- *physics - jetset version 6.2*, Comput.Phys.Commun. 39, 1986.

[32] ATLAS Collaboration, *Improved luminosity determination in pp collisions at* $\sqrt{(s)}$ *= 7 TeV using the ATLAS detector at the LHC*, arXiv:1302.4393 [hep-ex], 2013.

[33] S. Amato et al, *LHCb calorimeters technical design report*, CERN-LHCC-2000-036, 2000.

[34] M. Ferro-Luzzi, *Overview of lhc luminosity calibration measurements*, ICHEP, 2010.

[35] M. Britsch, *Cubic sideband subtration and the handling of a special kind of structure in the background*, LHCb-INT-2011-010, 2011.

[36] R. Aaij et al. (LHCb Collaboration), *Cubic sideband subtraction and the handling of a special kind of structure in the background*, Phys. Lett. B694, 2010.

[37] A. Bermudez Martinez, *Studies on the definition of inelastic Non-Single Diffractive events*, Ph.D. Thesis, DESY-InSTEC Cuba, 2014.

[38] S. Navin, *Diffraction in PYTHIA*, arXiv preprint arXiv:1005.3894, 2010.

[39] T. Sjostrand, S. Mrenna and P. Skands, *PYTHIA 6.4 physics and manual*, JHEP05 (2006) 026, http://home.thep.lu.se/~torbjorn/Pythia.html.

[40] S. Agostinelli et al., *GEANT4 a simulation toolkit*, Nucl. Instrum. Methods A 506 (2003) 250.

[41] LHCb Collaboration, *Measurement of the inclusive ϕ cross-section in pp collisions at $\sqrt{s}$ = 7 TeV with the LHCb experiment*, LHCb-CONF-2010-014, 2010.

[42] Biagio,Francesco,Walter, *Measurement of Prompt $\overline{\Lambda}/\Lambda$ and $\overline{\Lambda}/K^0_s$ production ratios in inelastic pp collisions at $\sqrt{s}$=0.9 and 7 TeV*, LHCb-ANA-2010-006, 2010.

[43] LHCb Collaboration, *Measurement of prompt hadron production ratios in pp collisions at $\sqrt{s}$=0.9 and 7 TeV*, Eur. Phys. J. C, 72:2168,2012.